BOND ANALYSIS OF METAL–ELEMENT INTERACTIONS IN MOLECULES AND SOLIDS APPLYING EMBEDDING AND DENSITY FUNCTIONAL TECHNIQUES

Dissertation

Zur Erlangung des naturwissenschaftlichen Doktorgrades der Julius-Maximilians-Universität Würzburg

Vorgelegt von

Kathrin Claudia Götz

aus Würzburg, Deutschland

Würzburg, **2009**

Eingereicht am: _____

An der Fakultät für Chemie und Pharmazie

1.Gutachter: _____

2.Gutachter: _____

der Dissertation

1.Prüfer: _____

2.Prüfer: _____

3.Prüfer: _____

des Öffentlichen Promotionskolloquiums

Tag des Öffentlichen Promotionskolloquiums: _____

Doktorurkunde ausgehändigt am: _____

Nicht müde werden
sondern dem Wunder
leise
wie einem Vogel
die Hand hinhalten.

Hilde Domin

(deutsche Lyrikerin, 1909-2006)

Contents

Abbreviations

BCP	Bond Critical Point
CC	Charge Concentration
CD	Charge Depletion
CN	Coordination Number
Cp	η^5-C_5H_5
Cp'	η^5-C_5H_4Me
DFT	Density Functional Theory
ECP	Effective Core Potentials
ED	Electron Density
ELF	Electron Localization Function
ELI	Electron Localizability Indicator
GGA	Generalized Gradient Approximation
HF	Hartree Fock
HOMO	Highest Occupied Molecular Orbital
IQA	Interacting Quantum Atom
KS	Kohn Sham
LDA	Local Density Approximation
LUMO	Lowest Unoccupied Molecular Orbital
Me	Methyl
NBO	Natural Bond Orbitals
NLMO	Natural Localized Molecular Orbitals
NPA	Natural Population Analysis
PBC	Periodic Boundary Conditions
PCM	Polarizable Continuum Model
PEECM	Periodic Electrostatic Embedded Cluster Model
QTAIM	Quantum Theory of Atoms In Molecules
TMCDA	N,N,N',N'-Tetramethylcyclohexane-1,2-diamine
VSCC	Valence Shell Charge Concentration

PART I

Introduction and Theoretical Background

Chapter 1

Introduction

Every science has its basic concepts and principles, the cornerstones on which everything else is constructed. At the heart of chemistry, there is a selection of fuzzy concepts that have already served as guidelines before the rise of quantum mechanics enabled their proper understanding. One of the most fundamental, if not *the* fundamental topic in chemistry is the deep comprehension and precise description of the chemical bond.[1] Although the principle of "elective affinities" can be traced back into the 17th century,[2] it took the landmark paper[3] of *G.N. Lewis* in 1916 to give the chemical bond the shape it still takes today: the joining electron pair. By the advertising work of *I. Langmuir*,[4, 5] Lewis' ideas became public and were encountered by *L. Pauling*, who developed his Nobel-prize honoured theory[6] about the "nature of the chemical bond". Due to *Pauling* the electron-pair bond obtained its quantum-mechanical backbone by the seminal discoveries (1928) of *Heitler* and *London* on the forces which hold H_2 together.[7, 8] When Lewis summarized his work at the Faraday Discussion Meeting in 1923[9] the

dichotomous universe of the chemical bond was already built between the electrostatic/ionic picture and the non-polar/covalent one by different degrees of polarization of the shared electron-pair. However, the fascination in chemistry is mainly due to the great variety of bonds that can be formed in between these two extreme situations, with each bond possessing its own specific character.

Since Lewis' electronic structure revolution, many exceptional and intriguing bonding situations have been discovered, among them agostic, multi-centered, metallic, dispersive, aromatic, anti-aromatic and multiple bonding up to quintuple bonds *etc*. (see e.g. ref [10]). The interaction between metal atoms and light main-group elements, especially carbon, has been of general interest ever since and determines the chemical behavior of a complete section of chemistry: organometallics. Not only because of the broad applicability of organometallic compounds in e.g. catalysis or bio-inorganic chemistry, but also due to their complicated electronic structure and intriguing bonding situations, the metal–non-metal bond has been of broad interest for all kinds of chemists.[11] Within this thesis two sub-classes of organometallics are investigated: i) transition-metal complexes, with a focus on carbene and borylene species (Part II), and ii) lithium-organic compounds, especially methyl derivatives (Part III).

Concurrently with the discovery of novel bonding situations, a plethora of methods have been developed to classify, describe and understand the chemical bond (c.f. special issue of J. Comput. Chem.: "90 years of chemical bonding").[12] The valence bond (VB) and molecular orbital (MO) theories have risen as two independent concepts to describe a broad range of bonding situations, both promoted by rivaling groups of supporters. However, the many useful schemes, which are available for the analysis of the chemical bond, may emphasize different aspects of bonding and hence yield varying chemical interpretations.[13] One category focuses on the electronic restructuring accompanying the bond formation process, namely the natural bond orbitals,[14-17] the atoms in molecules approach[18] or the electron localization function,[19-21] along with many variants of population schemes.[22, 23] A second group is based on the decomposition of the bond energy into chemically significant contributions, for instance the Kitaura-Morokuma approach[24] or the extended transition state scheme.[25-27] Alternatively, tools from the third group provide the classification of chemical bonds in terms of bond orders or bond multiplicity indices. Examples are the methods developed by Pauling,[6] Wiberg,[28] Jug,[29] Mayer[30] and Cioslowksi.[31]

In the following first part of this thesis, the basic formalism, applicability and shortcomings of the herein applied theoretical and quantumchemical tools are presented. Density functional theory is introduced, since it is the underlying technique used to obtain the molecular charge density that can be evaluated by bond analysis tools.

Chapter 2

Foundations of Density Functional Theory

The elementary principle behind Density Functional Theory (DFT) is the use of the charge density as the quantity from which every system property can be obtained. Although this idea has been developed in the 1920s (Thomas-Fermi model, 1927;[1, 2] continued by Slater, 1951[3]), it took another thirty years before Hohenberg and Kohn (1964)[4] provided the foundation to build DFT on solid grounds. Two basic theorems proofed the direct interdependence of the charge density and the wavefunction, which had been until then the exclusive object upon which quantum mechanics was based. However, it required the ideas of Kohn and Sham (1965)[5] to create the procedure that enabled DFT its prevalence in quantum chemistry. Today, DFT has demonstrated its high efficiency and accuracy despite the ambiguity of its details (e.g. the choice of appropriate functionals).

On the following pages, the basics of quantum mechanics are introduced, starting with the Schrödinger equation and a brief outline of the Hartree-Fock (HF) procedure, from which Kohn and Sham borrowed their idea of DFT orbitals. Based on the

Hohenberg-Kohn theorems, the Kohn-Sham approach will be introduced. We will proceed with a summary of functionals and their peculiarities and link them to electron holes, which will be also important for understanding the analysis tools ELF (Electron Localization Function) and ELI (Electron Localizability Indicator). Since the outline of this chapter is a brief summary of the methods that have been applied within this thesis, the extensive discussion of the particulars of quantum mechanics is omitted and can be found elsewhere.[6-13]

2.1 Fundamentals: the Schrödinger Equation and the Hartree-Fock Approximation

One of the fundamental pillars on which quantum mechanics was constructed in the 1920s are the wavefunction to express a quantum state and the Schrödinger equation as tool to describe the whole system or – in view of quantum *chemical* problems – to extract information from this state function. However, there exist different approximations for the Schrödinger equation depending on the system that shall be described.[6] For a stationary, non-relativistic system in state i with M nuclei at position $\mathbf{R}_M$ and n electrons at $\mathbf{r}_n$, the time-independent, non-relativistic Schrödinger equation can be obtained as

$$\widehat{H}\Psi_i(\mathbf{r}_1, \mathbf{r}_2 \ldots \mathbf{r}_n, \mathbf{R}_1, \mathbf{R}_2 \ldots \mathbf{R}_M) = \mathrm{E}_i\Psi_i(\mathbf{r}_1, \mathbf{r}_2 \ldots \mathbf{r}_n, \mathbf{R}_1, \mathbf{R}_2 \ldots \mathbf{R}_M). \qquad (2.1)$$

One easily recognizes that this is an eigenvalue equation of the Hamilton operator $\widehat{H}$. The state functions Ψ_i correspond to the eigenfunctions (also called eigenstates), and the energy of each state i is given as eigenvalue E_i. The eigenfunctions Ψ_i can be sorted with respect to their energies and match ground and excited states. *Via* the variational principle a tool is given, with which the best ground state wavefunction can be defined as the one with the lowest energy. The second-order differential operator $\widehat{H}$ can be expressed as

$$\widehat{H} = -\frac{1}{2}\sum_{i=1}^{n}\nabla_i^2 - \frac{1}{2}\sum_{A=1}^{M}\frac{1}{m_A}\nabla_M^2 - \sum_{i=1}^{n}\sum_{A=1}^{M}\frac{\mathrm{Z}_A}{\mathbf{r}_{iA}} + \sum_{i=1}^{n}\sum_{j>i}^{n}\frac{1}{\mathbf{r}_{ij}} + \sum_{A=1}^{M}\sum_{B>A}^{M}\frac{\mathrm{Z}_A\mathrm{Z}_B}{\mathbf{R}_{AB}}, \qquad (2.2)$$

including the masses of the interacting nuclei m_A as well as their charges Z_A. Within the Born-Oppenheimer approximation, the movement of the much heavier nuclei is separated from the electronic motion, and one derives the electronic Hamiltonian

$$\widehat{H}_{el.} = -\frac{1}{2}\sum_{i=1}^{n}\nabla_i^2 - \sum_{i=1}^{n}\sum_{A=1}^{M}\frac{Z_A}{\mathbf{r}_{iA}} + \sum_{i=1}^{n}\sum_{j>i}^{n}\frac{1}{\mathbf{r}_{ij}} \,. \tag{2.3}$$

The solutions obtained from the electronic Hamiltonian can be interpreted in terms of electronic wavefunctions depending on a static field of fixed nuclei.[i]

Based on the fermionic nature of the electron, this wavefunction has to be antisymmetric with respect to interchange of spatial or spin coordinates of any two electrons. This requirement is often called the Pauli Exclusion Principle, which is an independent postulate of quantum mechanics. A simple way to fulfill this condition is the Slater-determinant ϕ_{SD}, which is the anti-symmetrized product of *n* one-electron wavefunctions or spin-orbitals χ_i

$$\phi_{SD} = \frac{1}{\sqrt{n!}}\begin{vmatrix} \chi_1(\mathbf{x}_1) & \chi_2(\mathbf{x}_1) & \cdots & \chi_n(\mathbf{x}_1) \\ \vdots & \vdots & & \vdots \\ \chi_1(\mathbf{x}_n) & \chi_2(\mathbf{x}_n) & \cdots & \chi_n(\mathbf{x}_n) \end{vmatrix}. \tag{2.4}$$

Rows are labeled by electrons and columns by spin-orbitals. The spin-orbitals consist of a spatial part dependant on **r** and a spin function **s**, which can be either α or β (up- or down spin). The coordinate **x** summarizes both components **r** and **s**. Already at this stage, exchange effects are introduced, which arise from the requirement that $|\phi_{SD}|^2$ be invariant to the exchange of any two electrons. Consequently, the Slater-determinant incorporates the *Fermi correlation*, which means that the motion of two same-spin electrons is not independent. One can also express these exchange effects in terms of Fermi holes, which exist around every electron and eliminate the coexistence of two electrons with equal spins at the same point. For DFT approaches the Fermi (or exchange) hole has great importance and we will come back to this concept in the proceedings. Since the movement of electrons with opposite spin remains uncorrelated (Coulomb correlation), one refers to a single-determinant wavefunction as uncorrelated.

The Hartree-Fock Approximation

However, the Schrödinger equation can only be solved for the very simple cases like H_2^+ due to the many-electron problem. Consequently, it is one of the major goals in quantum chemistry to derive approximate solutions of the Schrödinger equation. The simplest

[i] This gave rise to the concept of potential energy surfaces. Within this approach the total molecular energy is depicted as hypersurface depending on the coordinates of the interacting nuclei.

useful approach to this problem and a real headstone in quantum chemistry is the Hartree-Fock theory (HF). It assumes that the exact many-body wavefunction within the Born-Oppenheimer picture can be approximated by the Slater-determinant, neglecting relativistic and electrostatic correlation effects. Hence, the HF (uncorrelated) ground state energy is simply given as

$$E_{HF} = \langle \phi_{SD} | \hat{H} | \phi_{SD} \rangle = \sum_{i=1}^{n} (i|\hat{h}|i) + \sum_{i}^{n} \sum_{j}^{n} (ii|jj) - (ij|ji), \tag{2.5}$$

with $\hat{h}$ being the one-electron Hamiltonian. It contains the average kinetic and nuclear attraction energy of the electron *i*, and can be expressed as

$$(i|\hat{h}|i) = \int \chi_i^*(\mathbf{x}_1) \left\{ -\frac{1}{2}\nabla^2 - \sum_{A}^{M} \frac{Z_A}{\mathbf{r}_{iA}} \right\} \chi_i(\mathbf{x}_1) d\mathbf{x}_1. \tag{2.6}$$

The terms $[ii|jj]$ and $[ij|ji]$ are the Coulomb J_{ij} and exchange K_{ij} integrals, respectively. They describe the electron-electron interactions and have the following form

$$[ii|jj] = [ij|ij] = \int \int |\chi_i(\mathbf{x}_1)|^2 \frac{1}{\mathbf{r}_{12}} |\chi_j(\mathbf{x}_2)|^2 d\mathbf{x}_1 d\mathbf{x}_2 = J_{ij}\,, \tag{2.7}$$

$$[ij|ji] = \int \int \chi_i(\mathbf{x}_1)\chi_j^*(\mathbf{x}_1) \frac{1}{\mathbf{r}_{12}} \chi_j(\mathbf{x}_2)\chi_i^*(\mathbf{x}_2)\, d\mathbf{x}_1 d\mathbf{x}_2 = K_{ij}\ . \tag{2.8}$$

The Coulomb part is the classical electrostatic contribution describing the repulsion an electron experiences from all other electrons due to its charge. The exchange part, however, results from a true quantum phenomenon – the indistinguishability of electrons – and incorporates the non-classical contributions (also the Fermi hole).

As mentioned before, the variational principle can be used to obtain the best ground state wavefunction by simply minimizing the energy. The variational freedom in this expression is the choice of the spin orbitals in the Slater determinant

$$E_{HF} = \min_{\phi_{SD} \to n} E[\phi_{SD}]\,. \tag{2.9}$$

However, these spin-orbitals have to remain orthonormal throughout the minimization procedure. This constraint enters as Langrangian multiplier[6] ε_i in the energy expression and one obtains the one-electron HF equations

$$\hat{f}\chi_i(\mathbf{1}) = \varepsilon_i \chi_i(\mathbf{1}) \tag{2.10.1}$$

$$= \left[\hat{h}(\mathbf{1}) + \sum_{j \neq i} J_j(\mathbf{1}) - \sum_{j \neq i} K_j(\mathbf{1})\right] \chi_i(\mathbf{1}) = \varepsilon_i \chi_i(\mathbf{1}). \qquad (2.10.2)$$

Hence, the Fock operator $\hat{f}(\mathbf{1})$ of an electron **1** is the sum of the core-Hamiltonian operator $\hat{h}(\mathbf{1})$ and an effective one-electron potential operator called the Hartree-Fock potential $v^{HF}(\mathbf{1})$. The HF potential consists of the Coulomb and exchange interactions with all other electrons **2** … n in orbitals $j \neq i$. Consequently, the unsolvable many-electron problem is broken down to two-electron interactions which are taken into account in an average way (v^{HF}). In other words, each electron is subjected to the time-averaged field created by all other particles. Hence, one obtains pseudo-eigenvalue equations which are related to each other due to the form of the Fock operator. Thus the HF equations are non-linear equations, which have to be solved *via* a self-consistent iterative procedure. From this energy minimization, the spin-orbitals χ_i are derived as eigenfunctions and the energies ε_i as the corresponding orbital energies. Hence, the canonical orbitals χ_i can actually be interpreted in terms of chemical or physical properties.

Of the many simplifications imposed in the HF approximation, the total neglect of electrostatic correlation is probably the most severe one for quantum chemistry. Even for simple cases like the dissociation of H_2 this leads to dramatically incorrect results. A number of approaches remedying this shortcoming have been made and collected under the term *post*-HF methods, and include Configuration Interaction, Coupled Cluster, Møller-Plesset and others. As a completely alternative approach, DFT can be used, since it contains approximations for both contributions: exchange and correlation interactions.

2.2 From Hohenberg-Kohn Theorems to the Kohn-Sham Approach

2.2.1 The Hohenberg-Kohn Theorems

On principle, DFT relies on the ground state electron density as the basic variable from which all system properties can be derived. However, it took the theorems of Hohenberg and Kohn to place this concept on physical footings.[4] These theorems laid the groundwork for reducing the many-body problem of n electrons with $3n$ spatial

coordinates to only three spatial coordinates on which the electron density depends. To prove the uniqueness of the ground state electron density, they derived the first Hohenberg-Kohn theorem.

If the ground state electronic energy is expressed in terms of potentials depending on the electron density, one obtains

$$E[\rho] = T[\rho] + V_{ee}[\rho] + V_{ext}[\rho], \tag{2.11}$$

with T being the kinetic energy, V_{ee} the electron-electron interaction energy and V_{ext} corresponding to the external potential. This energy expression can be divided in a universally valid part, containing the kinetic and electron-electron interaction energy, and a system-dependant one, equal to the external potential, which incorporates the electron-nucleus attraction. The first theorem proves that every external potential is a unique functional of the charge density, i.e. every system can be described by a single external potential corresponding to one electron density distribution. However, the functional forms of T and V_{ee}, summarized as Hohenberg-Kohn functional F_{HK}, are unknown, and especially the proper handling of T has been turned out to be very difficult. Otherwise, the exact solution of the Schrödinger equation would be possible for all chemical systems, since the Hohenberg-Kohn functional contains the universally valid parts.

2.2.2 The Kohn-Sham Approach

In 1965, Kohn and Sham suggested the use of a non-interacting reference system of equal density to solve the dilemma of the unknown Hohenberg-Kohn functional and make DFT of use for quantum chemistry. Within the Kohn-Sham (KS) approach the intractable many-body problem of interacting electrons in an external potential is simplified to a manageable problem of non-interacting particles moving in an effective potential.[5] Consequently, as much as possible can be computed exactly *via* the non-interacting reference and only a small portion has to be approximated. If the Slater Determinant, which is the exact wavefunction for a non-interacting system, is then built up from KS orbitals instead of HF orbitals, one obtains an antisymmetric wavefunction of non-interacting particles. In complete analogy to the HF scheme, one can derive the KS orbitals via the one-electron equation

$$\hat{f}^{KS}\varphi_i = \varepsilon_i\varphi_i, \tag{2.12}$$

with the one-electron KS operator $\hat{f}^{KS}$ being defined as follows

$$\hat{f}^{KS} = -\frac{1}{2}\nabla^2 + V_s(\mathbf{r}) = -\frac{1}{2}\nabla^2 + \left[\int \frac{\rho(\mathbf{r}_2)}{\mathbf{r}_{12}} d\mathbf{r}_2 + V_{XC} - \sum_A^M \frac{\mathbf{Z}_A}{\mathbf{r}_{A1}}\right], \tag{2.13}$$

and the exchange-correlation potential as

$$V_{XC} = \frac{\delta E_{XC}}{\delta \rho}. \tag{2.14}$$

The effective potential $V_s(\mathbf{r})$ has to be chosen so that the density resulting from the squared KS orbitals equals the real ground state density. Consequently, it connects the KS orbitals to the real system of interacting electrons. At this point it should be mentioned that, in contradiction to the HF approximation, $V_s(\mathbf{r})$ yields the exact one-electron density $\rho(\mathbf{r})$. The approximation enters the KS approach at the derivation of functional forms for $V_s(\mathbf{r})$. Additionally, one can ask if the KS orbitals have any physical meaning.[12] Indeed the highest occupied orbital (HOMO) energy is related to the exact first ionization energy of the system.[ii] The lowest unoccupied molecular orbital (LUMO) and all other virtual orbitals are solutions in exactly the same potential as the occupied orbitals and do not suffer from the energy up-shift like HF orbitals. This difference arises from the fact that HF virtual orbitals are within the field of all *n* electrons while KS virtual orbitals are derived from a potential of *n*-1 electrons. Thus the KS HOMO-LUMO gap gives a good approximation of excitation energies as has been observed empirically for quite some time. As a striking and important characteristic of $V_s(\mathbf{r})$ and its components, it should be mentioned that it exhibits a remarkable structure, such as peaks at intershell regions in atoms, bond midpoints, a step behavior if one moves from one atomic shell to the next etc. These characteristics are directly related to electron correlation and are "folded" into the one-electron potential $V_s(\mathbf{r})$.[12] To obtain suitable approximations to the effective potential is the most important quest of ongoing DFT research and will be a topic of the following chapter.

[ii] This is directly connected to the fact that the first ionization energy governs the asymptotic behavior of the density. Consequently, if the asymptotic behavior is described poorly by a chosen functional, the orbital energies suffer from an artificial up shift.[8]

2.3 Functionals and Electron Holes – about LDA, GGA and Hybrids

To gain insight into the construction of DFT functionals, one needs to understand the underlying patterns in the electron density as there are to emphasize exchange and Coulomb correlation. If the total energy of a system is calculated as

$$E[\rho] = T_S[\rho] + E_{Ne}[\rho] + J[\rho] + E_{XC}[\rho] \tag{2.15}$$

with T_S being the kinetic energy of the non-interacting system, $E_{Ne}$the electron-nucleus interaction and J the classical Coulomb interaction, E_{XC} summarizes all the non-classical parts as there are the kinetic energy contribution due to the interacting system, exchange and correlation energies. *Via* the adiabatic connection, it can be shown that the difference in the kinetic energies of the non-interacting and the interacting system is somehow folded into the exchange-correlation behavior.[14] Since exchange as well as correlation effects are not only dependant on the position of one electron but also on the spatial coordinates of the "interacting" electron, the electron density is not a sufficient quantity to describe these interactions properly, but one actually needs the pair density. In the following subchapter the pair density shall be introduced in terms of the density matrix as well as an introduction into the concept of electron holes shall be given.

2.3.1 Density Matrices and Electron Holes

On the next page a series of density matrices of different order are introduced. They can be derived from the wavefunction, which is from the KS orbitals. These density matrices are antisymmetric with respect to exchange of their indices and are related to each other. Consequently, lower order density matrices can be obtained from higher order ones by the formula[9]

$$\begin{aligned}\gamma_{p-1}(\mathbf{r}_1', \mathbf{r}_2' \ldots \boldsymbol{r_{p-1}}' | \mathbf{r}_1, \mathbf{r}_2 \ldots \boldsymbol{r_{p-1}}) \\ = \frac{p}{n+1-p} \int \gamma_p(\mathbf{r}_1', \mathbf{r}_2' \ldots \boldsymbol{r_{p-1}}', \mathbf{r}_p | \mathbf{r}_1, \mathbf{r}_2 \ldots \boldsymbol{r_{p-1}}, \mathbf{r}_p) d\mathbf{r}_p.\end{aligned} \tag{2.16}$$

Of special importance are the diagonal elements (**r**'=**r**), which are symmetric in all their coordinates and have the following physical interpretation. The electron density

Overview of density matrices (meaning of diagonal elements, r'=r)

- **electron density $\boldsymbol{\rho}(\mathbf{r})$ (first order)**

$$\gamma(\mathbf{r}_1'|\mathbf{r}_1) = n\int \psi^*(\mathbf{1}', \mathbf{2}, \mathbf{3} \ldots n)\psi(\mathbf{1}, \mathbf{2}, \mathbf{3} \ldots n)(d\mathbf{r}_1')$$

$$\int \gamma(\mathbf{r}_1)d\mathbf{r}_1 = n$$

- **pair density $\boldsymbol{\rho}_2(\mathbf{r}, \mathbf{r})$ (second oder)**

$$\gamma(\mathbf{r}_1', \mathbf{r}_2'|\mathbf{r}_1, \mathbf{r}_2) = \binom{n}{2}\int\int \psi^*(\mathbf{1}', \mathbf{2}', \mathbf{3} \ldots n)\psi(\mathbf{1}, \mathbf{2}, \mathbf{3} \ldots n)(d\mathbf{r}_1' d\mathbf{r}_2')$$

$$\int\int \gamma(\mathbf{r}_1, \mathbf{r}_2)d\mathbf{r}_1 d\mathbf{r}_2 = \frac{n(n-1)}{2}$$

- **p-order density $\boldsymbol{\rho}_p(\mathbf{r}, \ldots \mathbf{r})$**

$$\gamma\left(\mathbf{r}_1', \mathbf{r}_2' \ldots \boldsymbol{r}_p'\middle|\mathbf{r}_1, \mathbf{r}_2 \ldots \boldsymbol{r}_p\right) = \binom{n}{p}\int \ldots \int \psi^*(\mathbf{1}'', \mathbf{2}', \mathbf{p}' \ldots n)\psi(\mathbf{1}, \mathbf{2}, \mathbf{3} \ldots n)(d\mathbf{r}_1' d\mathbf{r}_2' \ldots d\boldsymbol{r}_p')$$

$$\int \ldots \int \gamma(\mathbf{r}_1, \mathbf{r}_2, \mathbf{p})d\mathbf{r}_1 d\mathbf{r}_2 d\mathbf{p} = \frac{n(n-1)}{p}$$

with *n* being the total number of electrons.

$\gamma(\mathbf{r}_1|\mathbf{r}_1) = \rho(\mathbf{r}_1)$ gives the probability of finding an electron with the spin s_1 at position $\mathbf{r}_1$ when all other electrons have arbitrary positions and spins. Hence, from the pair density $\gamma(\mathbf{r}_1, \mathbf{r}_2|\mathbf{r}_1, \mathbf{r}_2) = \rho_2(\mathbf{r}_1, \mathbf{r}_2)$ the probability is obtained to find one electron with spin s_1 at position $\mathbf{r}_1$, a second one with s_2 at $\mathbf{r}_2$ and all other electrons having arbitrary positions and spins. Since all matrices are antisymmetric in each set of their indices, they will vanish if two or more indices of a set are identical, i.e. the probability to find two same-spin electrons at one position $\mathbf{r}_1$ is zero, which leads us back to the concept of the Fermi hole.

An opportune way to describe the energy due to electron-electron interaction is *via* the pair density

$$E_{ee} = \frac{1}{2}\int\int \frac{\rho_2(\mathbf{r}_1, \mathbf{r}_2)}{\mathbf{r}_{12}} d\mathbf{r}_1 d\mathbf{r}_2. \tag{2.17}$$

This expression can be split into a classical (uncorrelated) Coulomb part and a non-classical exchange-correlation contribution

$$E_{ee} = \underbrace{\frac{1}{2}\int\int \frac{\rho(\mathbf{r}_1)\rho(\mathbf{r}_2)}{\mathbf{r}_{12}} d\mathbf{r}_1\, d\mathbf{r}_2}_{classical} + \underbrace{\frac{1}{2}\int\int \frac{\rho(\mathbf{r}_1)h_{XC}(\mathbf{r}_1, \mathbf{r}_2)}{\mathbf{r}_{12}} d\mathbf{r}_1\, d\mathbf{r}_2}_{non-classical}. \tag{2.18}$$

The first contribution contains the classical electrostatic interaction of two charge distributions. However, due to the form of the integral, it also contains the non-physical interaction of each particle with itself. This self-interaction error (s. also Chapter 1.4) is corrected by the second part which represents the interaction of an electron with the exchange-correlation hole $h_{XC}(\mathbf{r}_1, \mathbf{r}_2)$. This exchange-correlation hole can be split into the Fermi and a Coulomb hole, however, only the total hole has a physical meaning

$$h_{XC}(\mathbf{r}_1, \mathbf{r}_2) = \underbrace{h_X^{s_1=s_2}(\mathbf{r}_1, \mathbf{r}_2)}_{Fermi\ hole} + \underbrace{h_C^{s_1\neq s_2}(\mathbf{r}_1, \mathbf{r}_2)}_{Coulomb\ hole}. \tag{2.19}$$

The exchange hole has a normalization of –1 which removes the unphysical self-interaction of the Coulomb potential *J*. As mentioned before, the Fermi hole results from the Pauli Exclusion Principle or, mathematically expressed, from the antisymmetry of the density matrices. It therefore reflects the probability of finding a second electron near the reference electron at $\mathbf{r}_1$. Fundamentally, the exchange hole has to fulfill three exact constraints summarized in the following:

(1) on-top value $h_X(\mathbf{r}_2 \rightarrow \mathbf{r}_1, \mathbf{r}_1) = -\rho(\mathbf{r}_1)$

(2) normalization $\int h_X(\mathbf{r}_1, \mathbf{r}_2) d\mathbf{r}_2 = -1; \forall \mathbf{r}_1$

(3) non-positivity $h_X(\mathbf{r}_1, \mathbf{r}_2) \leq 0$

Depending on the density distribution of the reference electron, the Fermi hole can have individual forms – also be completely delocalized. Hence, the shape of the Fermi hole gives major insight into the underlying patterns of electron pairing. Analyzing tools like the ELF take advantage of this and were constructed from an approximation of the Fermi hole shape, which will be discussed later on.

In most cases, the Coulomb hole has much less importance for the shape of the total hole than the Fermi hole (exceptions are e.g. stretched bonds) and integrates to zero. One can think of it as a possibility to remove density from the position of the reference electron and accumulate it elsewhere.[7] Hence, it will be negative and largest at the position of the reference electron. However, the probability of finding two electrons of different spins at the same position is not zero in contradiction to the same spin case.

At this point the topic of correlation in general warrants comment. From the principles, correlation is defined as the difference between the HF exact-exchange energy and the real ground state energy. However, it can be split into a short-range contribution, which is dynamic, and a long-range part, a non-dynamic one. Dynamic correlation is due to the fact that electrons avoid each other due to their charge. Hence, if dynamic correlation is neglected like in the HF scheme the electrons come too close to each other and the Coulomb repulsion term is thus overestimated. Non-dynamic correlation results from the principle drawback of a one-determinantal method and gains special importance when dissociation procedures are described correctly. Within DFT the dynamic short-range contribution is explicitly represented by the correlation functional, while the non-dynamic part is included in the exchange functional.[15] How these functionals are constructed in detail will be topic of the following chapter.

2.3.2 Modern Functionals

Generally spoken, the development of density functionals concentrates on finding suitable approximations to the exchange-correlation part of the total energy expression, since all other contributions can be calculated exactly. The starting point for this quest

lies in the proper description of the homogeneous electron gas which gave rise to the *local density approximation* (LDA). Since the exchange energy of the uniform electron gas is described exactly by

$$\varepsilon_X = -\frac{3}{4}\left(\frac{3\,\rho(\mathbf{r})}{\pi}\right)^{1/3} \tag{2.20}$$

the exchange energy for a non-homogeneous system can be simply approximated as

$$E_X^{LDA} = \int \rho(\mathbf{r})\varepsilon_X[\rho]d\mathbf{r} = -\frac{3}{4}\left(\frac{3}{\pi}\right)^{1/3}\int \rho(\mathbf{r})^{4/3}d\mathbf{r}. \tag{2.21}$$

The correlation part is obtained from highly accurate Monte Carlo (most common parametrization by Vosko, Wilk and Nusair, VWN correlation functional)[16] simulations and included *via*

$$\varepsilon_{XC} = \varepsilon_X + \varepsilon_C, \tag{2.22}$$

and

$$E_{XC}^{LDA} = \int \rho(\mathbf{r})\varepsilon_{XC}[\rho]d\mathbf{r}\,. \tag{2.23}$$

The whole approach is termed “local”, since the exchange correlation potential depends solely on the local value of $\rho(\mathbf{r})$. As a consequence, the LDA hole is always attached to the reference electron. One can also extend the LDA to the unrestricted case, i.e. to systems with an odd number of electrons. The spin-sensitive approach is then called *local spin density approximation* (LSDA).

The L(S)DA approach works surprisingly well although the inhomogeneity of chemical systems is totally neglected. To correct this drawback, the *generalized gradient approximation* (GGA) was developed. In its beginnings (*gradient-expansion approximation*, GEA) it included the density gradient in terms of a Taylor expansion correction term to E_X^{LDA}. However, a real space cut-off had to be introduced to fulfill the aforementioned exchange hole constraints (2) and (3) to make the GEA approach physically meaningful. Additionally, instead of the actual density gradient $\nabla\rho(\mathbf{r})$ the reduced analog $s(\mathbf{r})$ is now used as an inhomogeneity parameter in GGA approaches and one obtains

$$E_X^{GGA} = E_X = -\frac{3}{4}\left(\frac{3}{\pi}\right)^{1/3} \sum \rho(\mathbf{r})^{4/3}\, F_X^{GGA}[s(\mathbf{r})] d\mathbf{r}, \tag{2.24}$$

with

$$s(\mathbf{r}) = \frac{|\nabla\rho(\mathbf{r})|}{\rho(\mathbf{r})^{4/3}}. \tag{2.25}$$

For the function *F* two main classes have been realized. The first was developed by Becke and includes an empirical parameter, which has been determined *via* least-squares fit (B88[17], PW91[18]). The second group uses for *F* a rational function of the reduced density gradient (P86[19], PBE[20]). These exchange functionals can be combined with different correlation functionals such as P86[21] (which contains one empirical parameter fitted to neon) or the very common LYP[22, 23] (also fitted to neon). Generally, GGA functionals have opened a new area in DFT due to the far better description of thermochemical data and have been further improved to *meta*- or even *hyper*-GGA functionals by including additional inhomogeneity parameters such as the second derivative of the density or the kinetic energy density to be more flexible.

Hybrid functionals are born from the idea of including the exact exchange behavior known from the HF scheme into the DFT approach. The exact-exchange itself is self-interaction free and shows the correct asymptotic behavior. Although the results of this approach were quite promising for atoms, it failed completely for molecules, since non-dynamical correlation is again neglected. Modern global hybrids are thus a well-balanced compromise between self-interaction elimination of the exact exchange contribution and the inclusion of non-dynamic correlation *via* the DFT exchange contribution

$$E_{XC}^{hybrid} = a\, E_X^{exact} + (1-a)E_X^{DFT} + E_C^{DFT}. \tag{2.26}$$

Probably the most famous example is Becke's B3 exchange functional, which is part of the successfull B3LYP.[24]

However, it is possible to fit the admixture of exact and DFT exchange more precisely to the nature of the system, i.e. to modulate the mixing variable *a*. The resulting *local hybrids* allow more flexible tuning of the exchange admixture by a local mixing function $g(\mathbf{r})$[25-27]

$$E_X^{LH} = \int g(\mathbf{r})\, \varepsilon_X^{exact}(\mathbf{r}) d\mathbf{r} + \int [1 - g(\mathbf{r})] \varepsilon_X^{DFT}(\mathbf{r}) d\mathbf{r}. \quad (2.27)$$

Additionally, it should be mentioned, that the implementation of exact exchange as a local and multiplicative functional dependent on the KS orbitals succeeded in the form of the so-called *optimized effective potentials* (OEPs). This has special meaning since DFT methods do not succeed in obtaining the Rydberg series of excited states correctly, although excitation energies are in principle better described within the DFT approach then the HF approximation, as mentioned before. The problem with the Rydberg series can be traced back to the incorrect asymptotic behavior of the exchange energy within conventional functionals. Hence, the OEP has been developed to correct this shortcoming for obtaining better spectroscopic data, nevertheless, the inclusion of correlation effects within OEPs is complicated in many cases.[28]

2.4 Shortcomings within the DFT Approach

As introduced in the previous paragraph, conventional exchange-correlation potentials are not attractive enough and exhibit incorrect asymptotic behavior, resulting in orbitals and eigenvalue spectra which do not contain a Rydberg series. Additionally, this leads to eigenvalues lying energetically too high and to HOMO-LUMO gaps that are often too small, albeit better than the HF ones. Furthermore, the description of charge-transfer excitations *via* DFT methods is still not possible, even within the approach of time-dependant DFT (TDDFT[29, 30]). Besides the wrong asymptotic behavior, many functionals violate further exact constraints like the uniform gas limit or the Lieb-Oxford boundary.[31] The consequences are doubtful and result in ambiguous descriptions of borderline cases, such as stretched bonds, near-degeneracy of states etc.

Coming back to the system quantum chemistry started with – the H_2 molecule – whose dissociation procedures are still a problematic task to be handled by conventional functionals in the restricted KS formalism.[32] This is due to the high amount of non-dynamic correlation or, to put it differently, to the wrong shape of the exchange-correlation hole. It has been stated that the key point in understanding the exchange-correlation behavior in multi-centered systems is the knowledge of the extent of delocalization of the exact exchange hole, which has, however, not been achieved yet and will be a demanding task for the future.[33] From a different point of view, one can also

consider this as a problem of fractional spins and charges. If an H_2 molecule is split and the two protons are separated to infinity, one would need fractional spins to obtain a solution that accounts for the correct symmetry. The necessary symmetry breaking can be solved by a multi-determinant method (see e.g. multi-reference configuration interaction), which is, however, not possible within the single-determinantal KS formalism. As an interim solution to this problem one can use *broken symmetry approaches*,[34] which are also applied for the description of antiferromagnetic systems.

However, underestimated energies might always be related to one of the most troublesome features that plague DFT – the self-interaction error. The self-interaction error is caused by an incomplete cancellation of the Coulomb self-interaction through the exchange hole (see also Chapter 1.3.1) and leads to too much delocalization, too low energies and too low energetic barriers in chemical reactions. Although self-interaction-free functionals have been constructed (B05[35], MCY[36]), they only account for the one-electron self-interaction and many-electron self-interaction can still only be handled by the exact exchange hole.[37]

Although this overview is still incomplete, only one further issue shall be mentioned at this point – the shortcomings within the individual functionals. The choice of the appropriate functional is one of the great quests within DFT and an evaluation of results obtained by various DFT methods is in most cases only possible *via* comparison to *post*-HF or experimental methods. While the second Hohenberg-Kohn theorem states that the exact energy is a lower limit for approximations, this does not hold for comparisons of energies obtained *via* different functionals since they incorporate unequal approximations to the Hamiltonian. Consequently, the energy cannot be used as a quantity to evaluate different solutions obtained with different functionals. However, it shall be mentioned, that the variational principle holds within a series of solutions derived within the same DFT approach (s. Chapter 1.2.1). Due to the diversity of approximations and drawbacks included in the variety of functionals, the system properties derived by applying them might qualitatively differ, without a criterion other than experiment or high-accuracy calculations to distinguish the correct solution.

Chapter 3

Introduction to Density-Based Topological Tools

With assistance of the previously introduced quantum chemical methods the electron density distribution of a given system can be obtained. However, it needs further tools to extract the chemically relevant information from these charge distributions. Therefore, the major aim of density-based analysis tools is to find a quantitative description for chemical bonding to classify the different interactions. The concept of bonding is deeply rooted in the idea of interacting subunits, mostly atoms, but also functional groups or even whole molecules that can be transferred among different compounds. Hence, most density analysis tools are based on the partitioning of the global charge distribution, to obtain the total system property as a sum of atomic contributions. The partitioning scheme is therefore of fundamental importance and influences the chemical interpretation. In the following chapter three different approaches, the quantum theory of atoms in molecules (QTAIM), the electron localization functions (ELF) and the electron

localizability indicator (ELI) shall be introduced, vicariously for all other density based tools.

3.1 The Quantum Theory of Atoms in Molecules

3.1.1 Basic Formalism

Bader's QTAIM is not simply an instrument to obtain bonding properties but a complete theory defining boundaries between the atoms forming a system and enabling an evaluation of their individual properties.[1-4] The partitioning of the molecular charge density into these atomic regions is done *via* the zero-flux boundary condition

$$\nabla\rho(\mathbf{r}) \cdot \mathbf{n}(\mathbf{r}) = 0, \tag{3.1}$$

with $\nabla\rho(\mathbf{r})$ being the gradient field and $\mathbf{n}(\mathbf{r})$ the normal vector on the surface enclosing the atomic basins. With reservations, the fulfillment of this boundary condition ensures that the atomic union is a proper open system to which quantum mechanics applies (especially the virial theorem as often emphasized by *Bader*, s. also Chapter 3.1.2). Alternatively, the atom in a molecule can be defined as the union of the nucleus, denoted as the source of all the paths of steepest ascent, and its gradient bundle. All properties O_Ω of this atom in a molecule can be obtained as the average of the appropriate operator density over the atomic basin

$$O_\Omega = \int_\Omega \rho_\Omega d\mathbf{r}. \tag{3.2}$$

Consequently, the total molecular property can be obtained as the sum over atomic contributions, which can be derived individually. This holds for both – one- and two-electron operators. From a chemical point of view, group properties can be calculated, and compared between different compounds.

However, besides atomic or group properties, bonding between two atoms is at the center of chemical investigation. Information about particular interatomic interactions can be gained via the gradient paths. Each gradient path has its source and sink at a so-called critical point (CP), i.e. a maximum, minimum or saddle point in the charge density. These CPs can be classified according to the (*rank, signature*) convention (Table 3.1).

The rank is defined as the number of non-zero eigenvalues in the Hessian matrix, i.e. the matrix containing all second derivatives of the charge density with respect to the spatial coordinates. The signature is calculated as the algebraic sum of the signs of the Hessian eigenvalues.

Table 3.1. Stationary points in the charge density.

topological object	**signature λ_i**	**$(n(\lambda_i), \sum \frac{\lambda_i}{\lvert\lambda_i\rvert})$**	**designation**
local maximum	–, –, –	(3, –3)	nucleus
local minimum	+, +, +	(3, +3)	cage critical point (CCP)
saddle point 1	+, +, –	(3, +1)	ring critical point (RCP)
saddle point 2	–, –, +	(3, –1)	bond critical point (BCP)

All critical points can be interpreted in chemical terms. The nucleus, although introducing a cusp in the electron density, is denoted by a local maximum, while its opposite, the so-called three-dimensional sink, can be interpreted as a cage critical point. The two saddle points are either termed bond critical point (BCP) or ring critical point (RCP) depending on their orders. The BCP is linked *via* the bond paths, i.e. the gradient of maximum electron density, with the two atoms on whose shared zero-flux surface it is positioned. According to Bader's theory, the existence (or absence) of a BCP and therefore a bond path is a sufficient criterion to denote the occurrence (or lack) of a chemical bond, although this stern interpretation has been doubted (Chapter 2.1.2). The bond paths have also been termed privileged exchange channels or preferred carriers for quantum-mechanical exchange to point out their connection to the quantum mechanical fundament of bonding.[5]

The total 3D network of bond paths is called a molecular graph and denotes the pairwise interactions present in the molecular system. However, the bond paths or BCPs can be associated with all kinds of chemical interactions and it is one of the most challenging quests within the QTAIM approach to extract sensible chemical information from these features. In principal, all critical points can be characterized by their values of charge density and their corresponding second derivative – the Laplacian $\nabla^2\rho$. Precisely, the Laplacian is defined as trace of the Hessian matrix at a given point. Consequently, it contains the information about the curvature of the electron density, which can be

interpreted as charge concentrations (CC, negative values) and charge depletions (CD, positive values). The Laplacian is related to the kinetic and potential energy, *G* and *V*, respectively, *via* the virial theorem, which states

$$\frac{1}{4}\nabla^2\rho(\mathbf{r}) = 2G(\mathbf{r}) + V(\mathbf{r}). \tag{3.3}$$

Consequently, the energy type in excess at a given point can be determined *via* the Laplacian and therefore a classification of bonds is possible into the dichotomic chemical system of covalent *vs*. ionic/polar. The BCP of a typically covalent bond exhibits high values of ρ and negative values of $\nabla^2\rho$ ($2G < |V|$) e.g. as it is found for C–H. The binding energy is supposed to be gained from charge accumulation in the interatomic region and therefore due to electron pairing and exchange. On the other side, for an ionic or strongly polarized bond (e.g. like Li–C) one expects values of $\rho < 1$ and positive values of $\nabla^2\rho$ ($2G < |V|$). For those interactions one observes separated charge accumulations localized within the boundaries of the interacting atoms, and the binding energy results from classical electrostatic attraction. This classification scheme works quite well for the second and also mostly for the third period but fails for heavy atoms whose outer shells are too diffuse and exhibit only small values of ρ and hence also for $\nabla^2\rho$. This is especially the case for transition metals or third row anions. Furthermore, the exceptional cases of molecules like F_2 or CO should be mentioned, which display positive Laplacian values due to the BCP being situated already in the core charge depletion region. Therefore, further bond classification schemes have been developed taking the individual curvatures of the Hessian or energy ratios into account (a detailed overview is given in [6, 7])

A further possibility to gain deeper insight into the electronic structure of a given molecule is an in-detail discussion of the Laplacian, which can also be analyzed by topological means. As mentioned before, the Laplacian can be interpreted in terms of charge accumulations and depletions, and its illustration in form of contour maps or isosurfaces allows the exposure of regions of nucleophilic or electrophilic attacks. Additionally, the shell structure of the isolated atoms is quite well represented by the density accumulations and depletions denoted within $\nabla^2\rho$. However, this correspondence is lost for all d-block elements. It has been shown that the binding or lone electron pairs

can be assigned to the local minima in the Laplacian distribution and have been termed valence shell charge concentrations (VSCCs).

One of the great advantages of discussing the topological features of ρ is that the molecular electron density distribution is an actual observable. Hence, we can gain direct access to the molecular information and derive chemical interpretations. Since a broad range of theoretical methods enables its simulation at different levels of theory, direct experiment-to-theory comparisons are possible.[8-11] This implies that the QTAIM can be universally applied to all of them – solid state and isolated gas-phase systems, experimental and theoretical ones – which is definitely one of its greatest strengths.[6, 12] Additionally, with the existence of a BCP a "definite" topological criterion is given to judge the presence of interatomic interactions and a principal classification of these interactions is possible, which is especially useful in terms of chemical interpretation. Both features have led to a wide application of the QTAIM. However, Bader's approach was also severely criticized.

3.1.2 Shortcomings, Criticism and Developments

First of all, the absoluteness of the one-to-one correspondence of bond path to actual chemical bonding has been doubted many times, especially for so-called non-bonded or repulsive interactions.[13, 14] For example, these interactions have been observed for endohedral fullerenes like He@C_{60}, neighboring anions or eclipsed biphenyl, which exhibits a bond path between the adjacent (repulsive) hydrogens of the two rings.[15-17] Although it has been emphasized to differentiate between bonding (chemical interaction) and binding (energy lowering due to bonding),[5] a strict correspondence between the existence of a bond path and chemical bonding cannot be adhered to.

To handle actual binding, an evaluation of energy contributions would be necessary, which has been attempted by use of the interacting quantum atom (IQA).[18, 19] Within the IQA approach the partitioning is accomplished *via* the density matrices and the total molecular energy is split into intra- and interatomic contributions. The individual energy contributions can then be related to different interactions between two atoms such as Coulomb, exchange, correlation etc. but also take into account the effective many-body contribution due to the deformation of the atoms within the molecular system compared to the free species. While the IQA opens up many interesting possibilities, the

concept is still in its infancy. For the definition of bonding regions within the QTAIM the use of probability distributions has been tested. However, the mathematical backbone for this approach is still under development.[20, 21] As a further analyzing tool the source function has been evolved from Green's propagator to trace back the origin of density contributions at a given point, e.g. the BCP.[22-24] The findings gained from the analyses of the source function for a series of *d*-block element compounds bear surprising resemblance to the ELF or delocalization/localization indices descriptions while only being dependent on the electron density. However, it has also been stated that the source function lacks the deeper physical comprehension of extent and kind of electron sharing which is provided by the aforementioned methods.[23, 25]

Besides the ambiguity within the chemical interpretation of the QTAIM features, Bader's approach has also suffered from fundamental criticism of its quantum chemical roots. Since the partitioning *via* the zero-flux condition is the all-dominant criterion within the QTAIM, the allegation of their non-uniqueness is of profound importance and was followed by a heated and still open discussion in the literature.[26-31] In detail, it has been stated that besides the surface which is used within Bader's approach to define the atom in molecule, there exists an infinite number of solutions to the zero-flux condition. The obtained surfaces (except one) pass through the nuclei and follow a gradient path, and hence, have to be excluded by an additional condition. Related to this feature, the inconsistent treatment of the nucleus cusp is criticized, which is excluded for the proper definition of the zero-flux surface, but included as a topological feature to define the (3,–3) critical point and therefore the basin attractor. Furthermore, the atomic partitioning is not well defined for electronic or vibrational excited states and might provide no separation into atoms at all or multiple atomic domains, though it has been discussed that this might be rooted in the Born-Oppenheimer approximation.

Bader himself has always emphasized the origin of the space-separation into atomic basins in Schwinger's variation principle.[29, 32] However, it has been discussed that Schwinger's principle cannot be applied to the zero flux atomic domains, because the underlying conditions of Schwinger's approach are not necessarily fulfilled for the zero-flux surfaces of QTAIM.[26, 27] A counter example has been constructed by adding density spikes to the reference wavefunction, which created additional artificial surfaces. This might also be related to the appearance of non-nuclear attractors or nuclei-free atomic basins, as they have been observed for lithium metal and related systems.[33, 34]

3.2 Real Space Functions for the Description of Electron Localization

Whenever covalent chemical bonding is discussed, one assumes a localized pair of electrons somewhere in the intermediate region of the respective two atoms. From the quantum chemical point of view this raises the question of whether the degree of electron localization can be calculated to obtain precise information about the regions of electron pairing. The first choices for discussing electron probability domains are perhaps molecular orbitals; however, these canonical orbitals are strongly delocalized and take several atomic centers into account. Localized equivalents can be derived by unitary transformations following various procedures without changing the total energy. Nonetheless, these transformations are not unique and may even result in qualitatively different chemical interpretations of bonding.[35] In the following chapter, alternative, orbital-independent descriptions of electron localization shall be introduced, which are either based on the pair density or related to the Fermi hole function.

3.2.1 The Electron Localization Function

For a localized electron pair one can assume that (1) there is a high probability of finding two electrons with opposite spins in one region and (2) there is only a small probability of exchange with other electrons (of same spin) outside this region. The Pauli repulsion for such a localized electron pair is therefore comparatively small. Hence, the key concept for understanding electron localization is the Fermi hole as a direct consequence of the Pauli Exclusion Principle. Or conversely spoken, if the electron is localized, so is its Fermi hole.[36]

As a pioneering approach, *Becke* and *Edgecombe* developed "*a simple measure of electron localization*" based on the probability of finding a second same-spin electron near the position of a reference electron, which was further developed by *Savin*.[35, 37] With respect to the conditional pair density P_{cond}, the short-range behavior of an electron at $\mathbf{r}_2$ approaching the reference electron at $\mathbf{r}_1$ is measured, which implies "scanning" the Fermi hole of the reference electron. The Taylor expansion of the spherically averaged conditional pair density around the position $\mathbf{r}_1$ of the reference electron is derived as

$$P_{cond} = \frac{1}{3}(\tau - \tau_w)(\mathbf{r}_1 - \mathbf{r}_2)^2 + \ \dots, \tag{3.4}$$

with the real kinetic energy being defined as

$$\tau = \sum_i (\nabla\varphi_i)^2, \tag{3.5}$$

and the local kinetic energy density τ_w (*Weizsäcker* kinetic energy density) in the absence of Pauli repulsion (one-particle case) as

$$\tau_w = \frac{1}{8}\frac{|\nabla\rho|^2}{\rho}. \tag{3.6}$$

Hence, the approximation of the conditional pair probability is related to the increase of kinetic energy density D_σ due to Pauli repulsion

$$D_\sigma = \frac{1}{2}\left[\sum_i (\nabla\varphi_i)^2 - \frac{1}{8}\frac{|\nabla\rho|^2}{\rho}\right]\rho. \tag{3.7}$$

It is obvious that D_σ will vanish in the case of a localized single, σ-spin electron, whose kinetic energy is identical to τ_w. The same holds for a pair of localized σ, σ‘-spin electrons. Hence, D_σ can be interpreted as a measure of electron localization, however, the function itself does not exhibit any significant structure. In enhancement, D_σ is scaled by the kinetic energy density of the uniform electron gas, D_σ^0, which is obtained analytically as

$$D_\sigma^0 = c_f \rho^{5/3}. \tag{3.8}$$

Furthermore, the final form of the electron localization function (ELF) was derived as

$$\eta = \frac{1}{1 - \left[\frac{D_\sigma}{D_\sigma^0}\right]^2}, \tag{3.9}$$

to obtain comparable values between zero and one, which can be interpreted in terms of low and high electron localization, respectively.

The essential quantity within *Becke* and *Edgecombe’s* derivation of the ELF is the HF same spin pair density to express D_σ. However, multi-determinantal wavefunctions would yield a different ELF expression. Therefore, *Savin et al*. have continued the ELF

approach but started from quite different premises and yielded an equivalent expression based on the Pauli kinetic energy density.[37] This bears the conceptual advantage that the kinetic energy density can be obtained from the first-order density matrix for any kind of wavefunction. Nonetheless, also in *Savin's* expression the scaling *via* the uniform electron gas is the essential feature to gain any chemical insight from the ELF. It is the arbitrary reference to the uniform electron gas that enables the ELF to exhibit the atomic shell structure in terms of regions with high electron localization and intermediate regions of low electron localization. *Bader et al.* has claimed that the incomplete homeomorphism between ELF and the Laplace function is due to this arbitrary reference.[38, 39]

When interpreting the ELF, one should consider a few important points. In principle, high ELF values correlate with high electron localization and low ones with high delocalization, which is related to a low or high amount of Pauli repulsion, respectively. However, the ELF can never reveal any information about the actual magnitude of Pauli repulsion. Furthermore, one should discuss the term "Pauli repulsion" with caution, since it is more a vague chemical concept than a sharply defined quantity. Another problem arises with the interpretation of ELF values lower than the uniform gas limit, i.e. below 0.5. Obviously, it makes no sense to talk about a system being more delocalized than the uniform electron gas, but these systems can solely be described as exhibiting more Pauli repulsion than the homogenous reference. Additionally, low ELF values refer by no means to low values of the charge density as has been claimed in the literature. However, one can relate the ELF values to the nodal properties of the occupied orbitals, since the ELF expression is based on the orbital slopes *via* $\nabla\varphi_i$.[40] Furthermore, whenever discussing ELF values exhibited by heavier elements, one has to take into account the penetration of the valence shell by the penultimate shells, which causes a lowering of the ELF value.[41]

In analogy to QTAIM, the continuous, differentiable scalar field of the ELF can be discussed by topological means. However, there is generally more than one basin associated with one nucleus. Within the ELF approach, a basin is defined as the region of all the points whose gradients terminate at the same (3,–3) critical point or ELF attractor. As mentioned before, the ELF distribution for an atom exhibits a radial sequence of spherical attractors, separated by ELF minima. The ELF repellors define the surfaces (*separatrix*) separating the atomic shell basins from each other. In general, if the electron

density is integrated over these basins, one yields approximately the chemically assumed amount of electrons for each shell. Besides the shell structure of the core basins, the chemical interpretation focuses on the patterns revealed in the valence shell. For the ELF, a multitude of basins associated with one or more nuclei can be found and classified by their shape, space location and electron population. Depending on the synaptic order, i.e. the number of nuclei related to one basin, the basins are interpreted in terms of lone pairs, two-center-two-electron bonds or even multi-center bonds. Compared to the QTAIM analyses, this bears the great advantage that complicated and delocalized bonding patterns can also be described and investigated, while the bond path is always associated with a two-body interaction only (a good overview about particular bonding situations and their ELF description is given in ref. [42, 43]).

3.2.2 The Electron Localizability Indicator

As mentioned in the previous chapter, the ELF suffers from the fundamental criticism of including an arbitrary reference in its definition, which is, however, necessary to obtain any chemical information. Additionally, the inclusion of correlation effects in the definition of the ELF, though attempted, has not yet been asserted.[44] As an improvement on the ELF concept, *Kohout et al*. developed the electron localizability indicator (ELI), which is freed from the dependence on the uniform electron gas and can be extended to the correlated level.[45-48]

To answer the question of electron localization on a more fundamental basis, one has to return to the dependant motion of electrons. All information about electron correlation is contained in the pair density, which can be split in different spin contributions to describe Fermi and Coulomb correlation, separately. In the following, we will focus on the Fermi correlation only case and therefore rely on the same spin pair density $\rho_2^{\sigma\sigma}$. The σ-spin pair density can be expressed in terms of two non-interacting density distributions at $\mathbf{r}_1$ and $\mathbf{r}_2$ and a correlation factor $f^{\sigma\sigma}$

$$\rho_2^{\sigma\sigma}(\mathbf{r}_1,\mathbf{r}_2) = \frac{1}{2}\rho^{\sigma}(\mathbf{r}_1)\rho^{\sigma}(\mathbf{r}_2)\left[1 + f^{\sigma\sigma}(\mathbf{r}_1,\mathbf{r}_2)\right]. \tag{3.10}$$

Now, if one considers the total space being divided into loges Ω, the number of σ-spin electron pairs $D_2^{\sigma\sigma}$ within these loges can be determined as

$$D_2^{\sigma\sigma} = \int_{\Omega} d\mathbf{r}_1 \int_{\Omega} d\mathbf{r}_2 \; \rho_2^{\sigma\sigma}(\mathbf{r}_1, \mathbf{r}_2) = \frac{1}{2}\left[\bar{\mathrm{N}}_2^{\sigma}(\Omega) + F^{\sigma\sigma}(\Omega)\right], \tag{3.11}$$

with the averaged number of σ-spin electrons being defined by

$$\bar{\mathrm{N}}_2^{\sigma}(\Omega) = \int_{\Omega} \rho^{\sigma}(\mathbf{r}_1) d\mathbf{r}_1, \tag{3.12}$$

and the correlation between the σ-spin electrons as

$$F_2^{\sigma\sigma}(\Omega) = \int_{\Omega} d\mathbf{r}_1 \int_{\Omega} d\mathbf{r}_2 \; \rho^{\sigma}(\mathbf{r}_1)\rho^{\sigma}(\mathbf{r}_2) f^{\sigma\sigma}(\mathbf{r}_1, \mathbf{r}_2). \tag{3.13}$$

If maximum electron correlation is interpreted in terms of maximum localization, $D_2^{\sigma\sigma}$ measures the localizability of same-spin electrons as follows. If there is exactly one σ electron per loge, the electrons are maximum correlated and $D_2^{\sigma\sigma}$ is obtained as zero. For any case with more than one σ electron per loge, the values of $D_2^{\sigma\sigma}$ are greater than zero. In other words, if there is no electron correlation ($F^{\sigma\sigma}(\Omega) = 0$), the average number of same spin electrons per loge is obtained as the total σ-spin density

$$D_2^{\sigma\sigma} = \bar{\mathrm{N}}_2^{\sigma}(\Omega) = \int_{\Omega} \rho^{\sigma}(\mathbf{r}_1) d\mathbf{r}_1. \tag{3.14}$$

Following the ELF concept, the ELI function was defined as

$$\Upsilon^{\sigma}(\mathbf{r}_1) = \frac{1}{1 + \left(c_q D_2^{\sigma\sigma}\right)^2}, \tag{3.15}$$

with c_q being a normalization factor dependent on the loge separation criterion. This criterion can either be charge-based or regulated by the amount of σ-spin electron pairs per loge.

However, the analytical form of $F^{\sigma\sigma}$ is unknown in most cases, and hence $D_2^{\sigma\sigma}$ has to be approximated by a Taylor expansion around the reference point $\mathbf{r}_1$. This Taylor expansion has individual forms for correlated and uncorrelated wavefunctions and can be extended to obtain proper descriptions within *post*-HF approaches. Furthermore, it could

be proven that for the HF case, ELF and ELI adopt quite similar forms and total distributions

$$\Upsilon_{HF}^{\sigma}(\mathbf{r}_1) = \frac{1}{1 + \left(\frac{\tau_P^{\sigma}(\mathbf{r}_1)}{c_q^{'} \rho^{5/3}(\mathbf{r}_1)} \right)^2}. \tag{3.16}$$

3.2.3 Comparison and Criticism

In general, the ELI approach can be viewed as an improvement on the ELF formalism, overcoming most of its deficiencies. For the ELF, the dependence on the uniform electron gas as well as the neglect of correlation effects in its definition have been criticized many times. Furthermore, single-determinant approaches should be preferred within the ELF formalism, since the ELF is not unique beyond this approximation. Additionally, the interpretative ambiguity of values below the homogenous gas limit has to be mentioned at this point, since this feature weakens the chemical significance of ELF results.

The ELI is based on a mathematical non-arbitrary definition and extendable to a variety of theoretical methods, both correlated and uncorrelated ones. In analogy to ELF, ELI can be discussed by means of topological analyses and depicts comparable information without the interpretative ambiguity. It has already been applied to a range of peculiar bonding situations and has proven its quality as an analyzing tool equivalent or even superior to the ELF.[49-51] Furthermore, the ELI patterns can be traced back to particular orbital contributions, which allow an interpretation in terms of σ- or π-involvement as an additional feature.

Besides the introduced QTAIM, ELF and ELI formalisms, there are many more methods for bonding analyses available. Comparable to the localization functions, the localized orbital locator[52, 53] or the approach of domain averaged Fermi holes[54] shall be mentioned selectively herein. As a useful tool for the investigation of electrostatic interactions, the three-dimensional visualization of the electrostatic potential is referred to; this can furthermore be combined with Hirshfeld partitioning[55-57] to gain insight into intermolecular polarization effects. In analogy to the hitherto discussed methods, the topological analysis of the electrostatic potential has been introduced recently.

Beyond these analyzing functions, there is a variety of orbital based approaches – localized and canonical ones. Canonical (or molecular) orbitals feature the advantage of incorporating the correct system symmetry and do therefore not suffer from non-uniqueness due to their invariance to unitary transformations. However, in many cases including most of the compounds in this thesis, canonical orbitals cannot be interpreted in terms of significant chemical information due to their complicated delocalized shape. Alternatively, localized orbitals can be discussed e.g. *Weinhold's* natural bond orbitals (NBO).[58, 59] Within the NBO procedure, NPA charges (natural population analysis) can be obtained in a pre-step, which have proven their convenience for analyzing charge transfer effects for molecular fragments e.g. in transition metal complexes (Part II).

While only a very selective and brief overview has been given about quantum chemical methods (HF, DFT) and bond analysis tools (QTAIM, ELF, ELI) within the first part of this thesis, the huge variety of theoretical approaches is already obvious at this point. Nonetheless, all these techniques suffer from specific shortcomings where they must be handled with caution and applied within the correct framework. Furthermore, the method-dependency of some results has to be taken into account and contradicting conclusions may be drawn employing varying techniques. Hence, obtaining reliable data with appropriate methods and their chemically non-ambiguous interpretation remains the true quest in computational chemistry and will therefore be the topic of all following chapters.

PART II

Chemical Bonding in Transition Metal Compounds

Chapter 4

Introduction

Despite their importance in many parts of chemistry, transition metal elements are considered notoriously difficult to handle by a large fraction of theoretical chemists and molecular physicists.[1, 2] Since most of the highly accurate wavefunction methods such as multireference approaches, CASPT2 (complete active space self-consistent field with second order perturbation theory) or MR-CI (multireference configuration interaction) cannot be applied to transition metals (or only with severe restrictions), difficulties in obtaining precise benchmark studies still remain.[3] The reasons for these troubles are numerous but can be narrowed down to the complicated electronic structure of transition metals, which is characterized by dense lying states causing near-degeneracy correlation between diffuse *ns* orbitals and contracted, partially filled (*n*-1)*d* orbitals.[4] Additionally, many transition metal complexes are paramagnetic and therefore open-shell systems. In combination with many low-lying excited states, this further hampers the attempt to determine the correct spin state.[4, 5]

However, with the rise of DFT[6], especially gradient corrected and hybrid functionals (see also Chapter 1.1), the situation has changed noticeably. Many molecular properties of transition metal compounds such as their structural parameters,[7, 8] spectroscopic (NMR, UV/VIS)[5] and energetic[1, 2] properties can now be obtained with impressive accuracy. Furthermore, the employment of small-core effective core potentials[9-11] (ECPs) and the implementation of suitable approximations in many standard quantum chemical software packages (e.g. ZORA[12], Douglas-Kroll-Hess[13]) facilitates the handling of relativistic effects.

Although the modeling of transition metal compounds is now possible by standard quantum chemical tools, the breakdown of the valence shell concept for *d*-block elements remains a conceptual problem. For all the transition metals the penultimate shell is involved in chemical bonding and the influence on specific atomic properties of the (n-1)*d* electrons may even dominate over that of the valence *ns* orbitals. The intermixture of penultimate and valence shell also becomes very obvious when the atomic shell structure is studied by analyzing tools such as ELF or the Laplace function (see Chapter 1.2). Since the perception of distinguishing between electronic shells is conceptually related to the definition of the valence configuration, it is interesting to note that both real space functions (ELF as well as the Laplacian) exhibit dramatic changes within the shell structure of transition metal atoms compared to main group elements. For the Laplace function the valence shell structure simply vanishes for increasing nuclear charge since Laplace contributions from different shells are summed up within the same spatial region. Hence charge concentrations and depletions smooth each other and no alternation of maxima and minima can be detected for the *d*-block elements (for a detailed discussion see e.g. ref. [14]).

Within the ELF contour plots the polarization of the penultimate shell can even be visualized (Figure 4.1). While the inner electrons produce the typical ELF ring attractors that can be interpreted in terms of the atomic shells, four maxima can be separated in the penultimate *d*-shell. Hence, when discussing bonding effects within transition metal compounds on the basis of ELF or the Laplace distributions, one has to be aware of the overlaying of valence and penultimate shell electrons.[15-18]

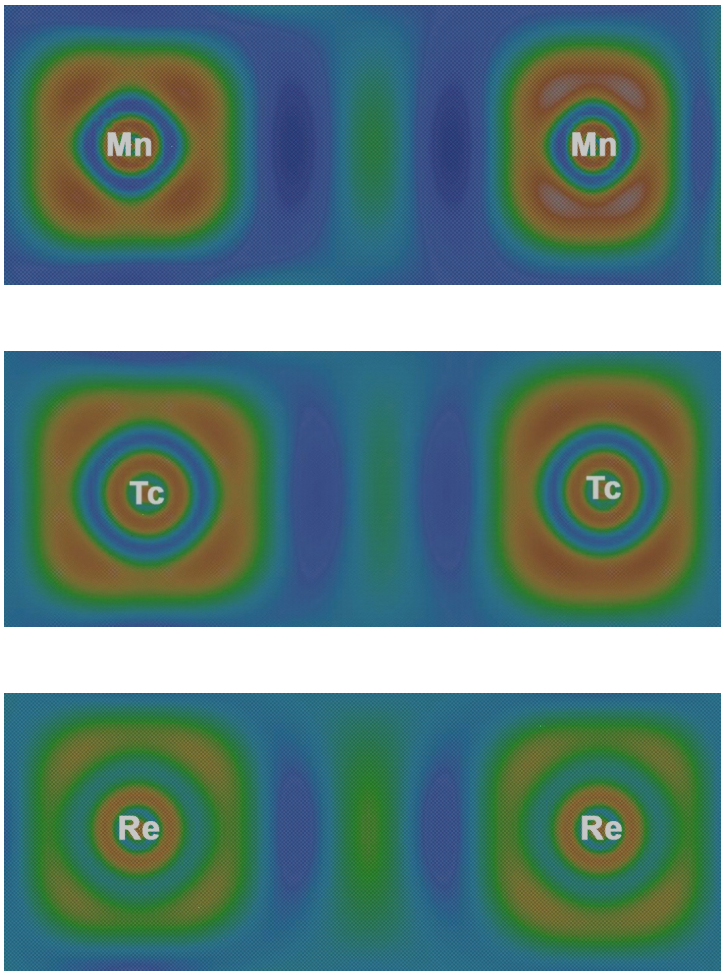

Figure 4.1. ELF contour plots for $[M_2(CO_{10})]$ with M=Mn, Tc, Re.

Although all transition metals exhibit the polarization of the penultimate *d*-shell, the 3*d* elements are exceptions within their own class. Since they are the first elements to exhibit *d* orbitals, the 3*d* orbitals lack radial nodes and are hence particularly small. Consequently, the radial maxima of 3*s*, 3*p* and 3*d* orbitals are all positioned within similar radial range. For chemical bonding, the ligand valence orbitals have to overlap with the metal 3*d* orbitals, however, experiencing Pauli repulsion from the outermost core shells (3*s* and 3*p*). Thus, weak bonds in transition metal chemistry do not derive from too diffuse and weakly bound valence electrons as in heavier main group chemistry, but from prohibitively small *d* orbitals. The consequences of this feature are numerous and very obvious in *d*-block chemistry. First of all the overall bond strengths increase towards the heavier elements, which is opposite compared to main group chemistry and can be directly related to the orbital characteristics discussed above. In these terms, even for equilibrium structures, many transition metal compounds exhibit stretched bonds, especially within the 3*d* series, which is closely related to low-lying excited states. These excited states can even account for the color of many transition metal complexes (in

particular those containing 3*d* metals), since light within the visible spectrum is absorbed to excite electrons into these unoccupied orbitals. A detailed discussion on the influence of radial nodes for chemical bonding can be found e.g. in ref. [19].

In the following chapters, an overview about bonding patterns in transition metal complexes will be given in view of the particular electronic structure of the *d*-block elements. Special emphasis is put on interactions between the metal atoms as well as on the specific kinds of bonding between bridging ligands such as carbenes and borylenes and the individual metal centers. In Chapter 5 an overview of metal–metal interactions is given and the particular features of metal–ligand and metal–metal bonding are discussed with respect a series of dinuclear iron complexes. In the subsequent chapter (Chapter 6), the concept of Fischer and Schrock carbenes is introduced and extended to borylenes to explain the varying characteristics of borylene ligands in differing M–B bonding motifs. In Chapter 7, the dependency of QTAIM and ELF results for bonding analysis on the functional is discussed using a selection of bridging borylenes and carbenes, including the prototypical complex of *Hermann at al*.[20] Finally, two borylene-supported dinuclear cobalt and nickel complexes are analyzed and compared in terms of their individual M–B and M–M bonding features.

Chapter 5

Bonding Patterns in Dinuclear Iron Complexes – an Overview of Metal–Metal Interactions

Transition metal carbonyl complexes are among the most prominent and well-studied classes of organometallic compounds due to their vast structural diversity and applicability. Carbonyl complexes are used as common reagents in organometallic synthesis since the CO ligand can easily be substituted to create systems with novel and unusual features, e.g. as the herein discussed boron transition metal complexes (Chapter 4 and 5).[1] Beyond this, they have proven their significance as homogeneous or heterogeneous catalysts,[2] for reasons which are related to the experimental accessibility of the CO ligand and its efficient, synergetic binding (i.e. good σ-donor and π-acceptor ability) to transition metals. Due to this favorable metal–ligand interaction a variety of bonding motifs have been observed for the CO ligand, ranging from terminal to different

types of bridging coordination.[1, 2] However, the borderline between these two situations is subtle and several metal clusters are known which exhibit both conformers – terminal-only as well as bridged (e.g. the gas-phase potential energy surface of $Co_2(CO)_8$ is characterized by three minima corresponding to terminal, semi-bridging and bridging coordination. However, only the doubly bridged conformation is found in solid state).[3, 4] Nevertheless, the binding differs considerably for terminal and bridging states.[5] In agreement with lower CO stretching frequencies, the electron density found in only one π^* orbital of the bridging CO is greater than that allocated in two orthogonal π^* levels of the terminally bound CO. Hence, considering dinuclear metal complexes, electron density can effectively be transferred between the two metal atoms *via* the CO bridge without the requirement of a direct metal–metal bond.

The question about the existence and nature of a direct metal–metal interaction has been a matter of debate[6] ever since the structure determination of the first dimeric metal carbonyls, namely $[Fe_2(CO)_9]$[7] and $[Mn_2(CO)_{10}]$[8]. Although it might be answered straightforwardly with respect to the 18-electron rule, doubts about the presence of an actual M–M bond came from early analyses of experimental[9] and theoretical[10] deformation densities, which did not detect any significant charge accumulation at the metal–metal midpoint. In addition, long-range M···CO interactions were evoked as the predominant source of stability in early calculations,[11] and molecular orbital considerations from the late 1970s[12, 13] classified the metal–metal interaction as predominantly repulsive. Later, experimental studies revealed at least small, covalent M–M bonding contributions in unsupported metal dimers[14, 15] and sustained the idea of delocalized bonding *via* the bridging ligand in supported examples.[16, 17]

In this context, the case of the triply bridged $[Fe_2(CO)_9]$, **1**, is a primary example for studying bridged metal carbonyls and it has been investigated with various methods and techniques (e.g. [18] and references therein). Historically, the short Fe–Fe distance of only 2.523 Å (only 0.05 Å longer than in the elemental iron) substantiated the belief in direct metal–metal bonding.[19] However, very early calculations indicated that the iron 3*d* orbitals would have to undergo severe distortion to form a direct bond, and would prefer a through-bond mechanism *via* the three CO bridges.[13, 20] Hence, already from these pioneering studies the absence of a direct Fe–Fe bond was concluded and related to the structural constitution of the central metal–bridge–metal unit. Later, a more detailed analysis revealed a small direct Fe–Fe attractive interaction, hidden under the

overwhelming metal–metal repulsion.[21, 22] This behavior indicates that a fine balance between attractive and repulsive forces takes place in the central metal–bridge–metal unit, which is influenced by the nature of the participating metals and the acceptor and donor qualities of the bridging ligand. In this context the special role of 3*d* metals is interesting to note. Due to the contracted character of the nodeless 3*d* orbitals (s. Chapter 4), they are less effective in both cases, M–M bonding as well as π back-bonding to the terminal CO ligands.[23] Thus a number of CO bridges is preferred within the 3*d* metal carbonyls. Conversely, the more diffuse and polarizable orbitals of the heavier analogues enhance both interactions, which is why a structural change from bridged to terminal preference is observed within the carbonyls of iron, ruthenium and osmium.[3] Beyond this, the interplay of indirect bonding *via* the bridge and direct metal–metal interaction has also been addressed by altering the bridging ligand[24] or the bridge geometry.[25] In view of this work, a systematic study on the changes in the charge density distribution occurring on structural deformation of the triply bridged $[Fe_2(CO)_9]$, **1**, is presented in the following chapter.

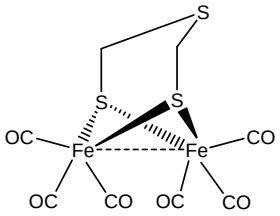

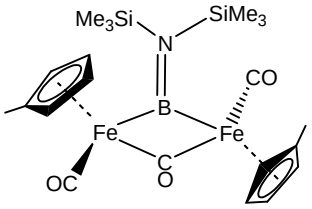

Scheme 4.1. Structures of the diiron complexes $[Fe_2(SCH_2SCH_2S)(CO)_6]$, **2**, and $[Fe_2\{BN(SiMe_3)_2\}Cp'_2(CO)_3]$, **3,** (Cp': η^5-C_5H_4Me).

To study the influence of the bridging ligand itself on a broader range, two dimeric iron complexes have been selected and compared to phosphorus bridged and semibridged analogues (Chapter 5.3). The trithiolane complex $[Fe_2(SCH_2SCH_2S)(CO)_6]$, **2**, has gained special importance as a model for the active site in [Fe-only] hydrogenases and the question of direct metal–metal bonding is therefore closely related to biological reactivity.[26] Beyond this, $[Fe_2\{BN(SiMe_3)_2\}Cp'_2(CO)_3]$, **3**, has been chosen since borylenes have been identified to be closely related to the ubiquitous CO ligand. Similar to the transition metal carbonyls, B–R ligands adopt the same coordination modes – terminal-[27], doubly-[28, 29] and triply-[30] bridging as well as semi-bridging[31]. However, theoretical studies revealed even better σ-donation and π-acceptor capabilities for the borylenes compared to CO.[32] Hence, apart from better steric protection of labile metal

centers by larger borylene ligands like {$BN(SiMe_3)_2$}, they offer enhanced electronic stabilization. Since **3** provides both CO and borylene bridges, the similarities and differences within both metal-ligand interactions can be studied in detail.

5.1 Computational Details

All optimizations were performed at the B3LYP/TZVP[33-37] level of theory using the Turbomole package[38-40] (version 5.10), based on coordinates obtained from X-ray diffraction studies. For the bridged-to-terminal metamorphosis partly fixed internal coordinates were used to obtain the correct deformation angle, while all other coordinates were optimized. The electronic structure analyses were performed at the density functional theory level. Initially, the gradient-corrected functional BP86[41, 42], the B3LYP[33-36] hybrid functional and the BHLYP[43] hybrid functional were compared. As the basic topology of charge density and ELF did not depend on the functional, only the B3LYP results are reported herein. Charge-density analyses used the AIM2000[44] program package. The ELF was analyzed with the TopMod program[45, 46].

5.2 Bridged-to-Terminal Metamorphosis in Fe_2CO_9

Comparable to the study of *Macchi et al.* regarding $[FeCo(CO)_8]^-$[25], the effect of structural distortion upon the electron density and ELF distribution in **1** was studied to identify the influence of the bridge geometry on the Fe–Fe interaction. Since no high-resolution experimental data has been available (as in the case of *Macchi et al.*), the investigation is based on the fully optimized structure of **1** (model **1**). By gradually altering the original Fe–Fe–C angle of 51.2° of one CO bridge towards 60° (model **2**), 70° (model **3**), 80° (model **4**) and 90° (model **5**), a semi-bridged conformation was finally obtained. In addition, one bridging CO ligand was fully removed to yield $[Fe_2(CO)_8]$ (model **6**).

However, none of the studied models features an Fe–Fe bond path and only for model **6** was an ELF valence basin associated to the metal–metal interaction detected (the divergence between ELF and QTAIM results is an interesting feature to be noted in this context; see Appendix A for Figure A1). Only for a totally unsupported and therefore strongly deformed conformation (not reported here), a bond path and hence a bond

critical point is obtained. Also in the case of $[FeCo(CO)_8]^-$, the metal–metal bond path evolved quite late on the conversion from bridged to terminal. In summary, this seems to provide further evidence for the effective charge transfer *via* the bridging CO ligands that overwhelms the direct metal–metal interaction.

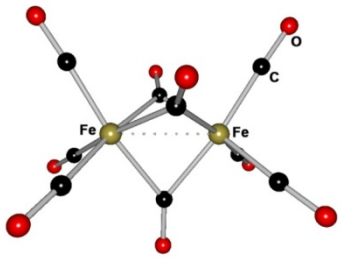

Figure 5.1. Structure of $[Fe_2(CO)_9]$, **1**.

Nevertheless, it is interesting to note that in apparent contradiction to the through-bond interaction mechanism, the supported species exhibit shortened M–M distances and elongated M–CO bonds compared to the terminal examples.[47] Table 5.1 summarizes the structural changes observed throughout the conversion of **1**. First of all, going from the original structure (model **1**) to one with a more unsymmetrical bridging mode, the Fe–Fe distance is noticeably shortened (2.520 to 2.473 Å, except for model **3**) with a minimum for the doubly-bridged structure **6** (2.454 Å). Hence, two CO bridges arranged in-plane with the metal–metal axis seem to decrease the repulsive forces between the iron centers and therefore entail a shorter metal–metal distance compared to the triply bridged case (see Appendix A for Figure A1). Furthermore, one can observe the conversion of the deformed CO group from bridged, with elongated C–O distance (1.165 Å), to terminal (1.142 Å).

Table 5.1. Selected structural data in Å of the bridged-to-terminal conversion.

model	Fe–Fe	Fe–$C_{termial}$	Fe–C_{bridge}	Fe–$C_{bridge*}$	C-O_{bridge}	C-$O_{bridge*}$	C-$O_{terminal}$
1	2.530	1.829	2.009	2.009	1.165	1.165	1.142
2	2.529	1.81-1.84	2.010	2.010	1.164	1.152	1.141
3	2.559	1.80-1.85	1.90-2.01	2.009	1.170	1.142	1.141
4	2.512	1.80-1.85	2.01-2.06	2.033	1.165	1.135	1.141
5	2.473	1.79-1.85	1.97-2.01	2.009	1.169	1.132	1.13-1.14
6	2.454	1.81-1.82	1.979	-	1.165	-	1.141

*deformed bridge.

5.3 Metal–Metal Interactions in Supported Diiron Complexes

The discussion in this chapter was mainly focused on the mere existence of a direct metal–metal interaction in dimeric complexes, and the structural features that might influence the occurrence of a bond path were investigated. Besides the nature of the bridging ligand altering the central structure motif, it also influences the strength of σ and π bonding capabilities and therefore the magnitude of through-bond interaction between the metal atoms. In the following chapter four bridged and semi-bridged complexes shall be presented, with some of them featuring a direct metal–metal bond path. However, the analysis of interactions between metal atoms within the framework of QTAIM is not straightforwardly accomplished. Although a thoroughly considered set of correspondence rules for interpreting topological QTAIM features in terms of chemical concepts has been worked out for main group light atom molecules, it cannot easily be extended to transition metals. It has been stated that heavy atoms exhibit an inherently different "chemical constitution" which can be accounted to (1) the coexistence of contracted 3*d* and diffuse 4*s* orbitals in the valence shell, (2) the large total amount of core electrons and (3) the huge atomic size – features which all leave recognizable traces in the Laplacian distribution (see also Chapter 3.1: breakdown of the correspondence between atomic shell structure and minima/maxima within the Laplacian distribution for transition metals).[47-49] Hence, the QTAIM properties displayed by heavy atom interactions might differ considerably from those of light atoms, which has opened a still ongoing debate about the nature of metal–metal bonds. It shall be noted in passing that the influence of approximations to include for relativistic effects on the topology of the electron density has also been investigated.[50] In summary, BCPs between transition metals exhibit very low density and Laplacian values clustering around zero. Hence a set of further energy criteria has been established to classify the metal–metal interactions as predominantly closed-shell or open-shell/shared (see for e.g. [47, 48, 51]). Moreover, the symmetry and shape of the Laplacian distribution along the bond path might offer valuable information about the bond polarity and has been emphasized as a much more significant criterion for bonding analysis in heavy atom compounds than the BCP properties.[48] Since all complexes studied in this chapter are strictly symmetric with respect to the metal–metal interaction, it seems, however, legitimate to assume a homopolar and therefore shared interaction in first approximation between the metal atoms in accordance to ref. [48].

$[Fe_2(SCH_2SCH_2S)(CO)_6]$, **2**

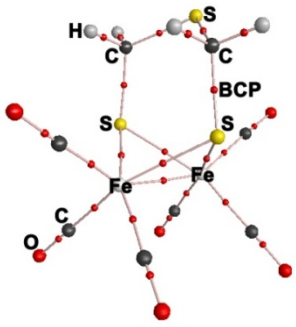

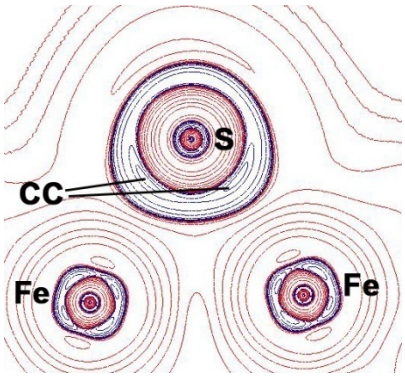

$[Fe_2\{BN(SiMe_3)_2\}Cp'_2(CO)_3]$, **3**

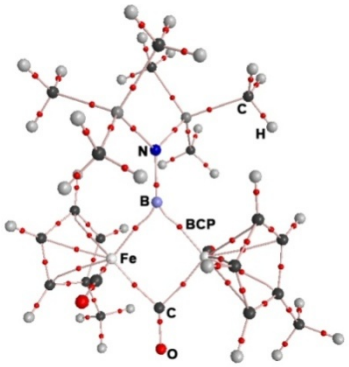

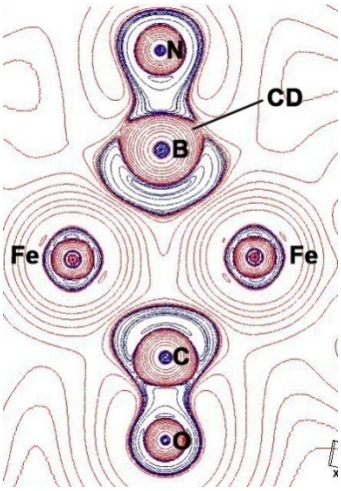

$[Fe_2(CO)_6(PH_2)_2]$, **4**

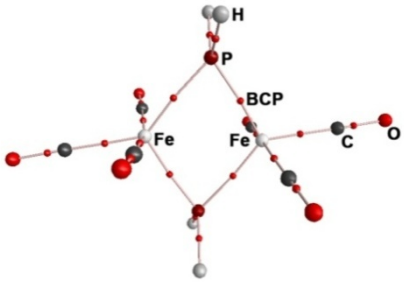

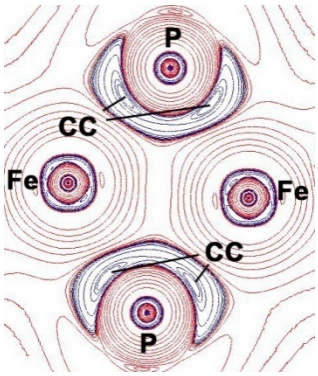

$[Fe_2(CO)_6(PF_3)_2]$, **5**

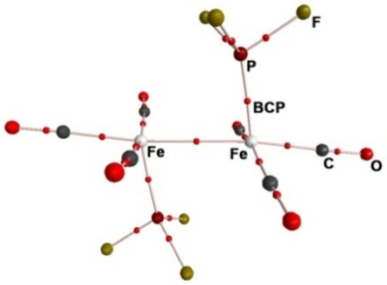

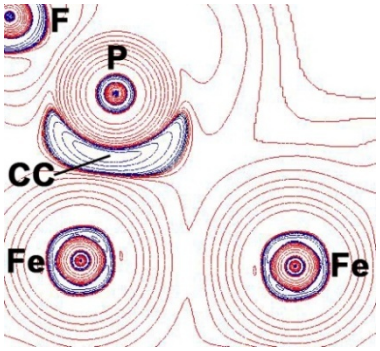

Figure 5.2. Molecular graphs and Laplacian maps; BCPs are indicated as red dots; charge accumulations ($\nabla^2\rho < 0$) are printed in blue, charge depletions ($\nabla^2\rho > 0$) in red. CC: charge concentration, CD: charge depletion.

For studying the influence of the bridging ligand on the metal–metal interaction, four complexes have been selected with iron in the formal oxidation states 0 and +1. $[Fe_2(SCH_2SCH_2S)(CO)_6]$, **2**, can be obtained from the reaction of 1,2,4-trithiolane with **1** and has cast interest as model system for [Fe-only] hydrogenases.[26] The two Fe^{+1} centers are doubly bridged by sulfur atoms and exhibit a distance of 2.512 Å in the X-Ray determined structure (2.532 Å in the optimized structure), which is roughly comparable to that found in **1** (2.520 Å). Moreover, a bond path is observed between the two metal atoms (see molecular graph in Figure 5.2) with the values of ρ and $\nabla^2\rho$ at the BCP being 0.324 eÅ^{-3} and 1.464 eÅ^{-5}, respectively (see also Table 5.2). As expected from the chemical point of view, the iron–sulfur interactions can be classified as dative or closed-shell with significantly positive values of the Laplacian (av. 4.135 eÅ^{-5}; compared e.g. to values of $\nabla^2\rho$ ranging between –16.60 and 5.34 eÅ^{-5} for S–N and S–C bonds[52]). The contour plot of the Laplacian within one of two iron–sulfur–iron planes features two VSCCs pointing from the sulfur atom to the particular metal centers. However, no significant charge accumulation is detected between the metal atoms.

Similarly, $[Fe_2(CO)_6(PH_2)_2]$, **4**, consists of two $[Fe(CO)_3]$ fragments being doubly bridged by phosphido ligands. The iron–iron distance is found to be slightly elongated to 2.673 Å in the optimized structures compared to **1**. However, in contrast to **2**, no bond path was detected between the metal atoms. The BCP properties of all iron–phosphorus bonds feature low density (0.564-0.602 eÅ^{-3}) and positive Laplacian values (2.619-2.697 eÅ^{-5}), which are approximately comparable to the dative iron–sulfur bonds in **2**. Within the Laplacian contour map (see Figure 5.2) two individual VSCCs can be observed on both phosphorus atoms pointing at the respective metal centers.

The dinuclear iron complex **3** can be obtained from $Na[Cp'Fe(CO)_2]$ and Br_2BNMe_2 *via* salt elimination and hydrolysis (as well as the corresponding ruthenium compound) and features an iron–iron distance of 2.548 Å (X-Ray structure).[53] Within the doubly bridged complex no BCP was detected between the metal atoms. The iron–boron bonds feature very different properties compared to the former dative metal–sulfur and –phosphorus interactions with very low values of $\nabla^2\rho$ (0.318 and 0.418 eÅ^{-5}). This might be accounted to the Lewis acidity of boron which modifies the charge concentration in the outermost shell and hence shifts the BCP into a region of flat Laplacian distribution. Additionally, it is interesting to note the differences between the

borylene and CO bridges in the Laplacian contour plots. While the carbon atom is surrounded by a continuous shell of charge concentration, the boron atom exhibits a gap of charge depletion symmetrically positioned along the boron-nitrogen bond, enabling nucleophilic attack along this coordinate (see Figure 5.2). Unlike the former third row atoms, both bridging centers exhibit only a single VSCC pointing at the midpoint of the metal–metal axis. The interpretation of this feature will be discussed extensively in the following chapters.

Table 5.2. BCP properties of selected bonds.

Compound	Bond	ρ [eÅ^{-3}]	$\nabla^2\rho$ [eÅ^{-5}]
2	Fe1–Fe2	0.324	1.464
	Fe1–S1	0.483	4.137
	Fe2–S1	0.495	4.134
	Fe1–S2	0.482	4.137
	Fe2–S2	0.495	4.134
	Fe–CO*	0.948	13.857
3	Fe1–B	0.662	0.418
	Fe2–B	0.683	0.318
	Fe–CO_{bridge}*	0.827	5.054
	Fe–$CO_{terminal}$*	1.055	15.121
4	Fe1–P1	0.564	2.619
	Fe1–P2	0.601	2.697
	Fe2–P1	0.602	2.687
	Fe2–P2	0.566	2.623
	Fe–CO*	0.928	13.728
5	Fe1–Fe2	0.281	0.842
	Fe1–P1	0.781	4.238
	Fe2–P2	0.781	4.237
	Fe–CO*	0.902	13.006

*values averaged

$[Fe_2(CO)_6(PF_3)_2]$, **5**, could only be obtained in a semi-bridged conformation. Compared to **4** (2.673 Å), the iron–iron distance of 2.630 Å is found to be considerably shortened as well as one of the iron–phosphorus bond lengths (2.092 compared to 2.233

and 2.265 Å in **4**). Since the semi-bridged arrangement cannot ensure the metal–metal interaction *via* the bridge, the direct metal–metal bond overwhelms the through-bond mechanism and a bond path is observed between the iron atoms. Similar to **2**, the corresponding $BCP_{Fe–Fe}$ provides low density (0.281 $eÅ^{-3}$ compared to 0.324 $eÅ^{-3}$) and Laplacian values (0.842 $eÅ^{-5}$ compared to 1.464 $eÅ^{-5}$). In the semi-bridged conformation only one VSCC is observed between the phosphorus atom and one iron center (see Figure 5.2), which seems to be more consistent with a terminal ligand than a bridging one in this context. In agreement with **2**, no charge accumulation is detected between the metal atoms.

To scrutinize the differences leading to occurrence or absence of the Fe–Fe BCP, the canonical molecular orbitals of **2-5** have been investigated. For the sulfur-bridged **2**, the attractive orbital interactions between the metal centers exceed the repulsive ones in magnitude and energetic weighting. Moreover, the Fe–S orbital interactions appear less pronounced compared to the according Fe–P ones in **4**, supporting the perception of weaker $M–E_{bridge}$ bonds in **2**. Due to the butterfly structure of the sulfur bridges, a different set of metal-*d* orbitals accounts for the metal–metal interaction *via* the bridging ligand, which seems to be less opportune for the through bond mechanism than the arrangement in **3** and **4**.

Within the canonical set of occupied orbitals of **5**, no interaction between both metal centers and the PF_3 entities is detected, which can most probably be attributed to the semi-bridged structure. It should be mentioned that this is in contradiction to **2**, in which the iron *d*-orbitals feature an out-of-plane interaction concurrently with both sulfur atoms. For the borylene-bridged **3**, the classification of orbital interactions is far more complicated, since most of the molecular orbitals are strongly delocalized due to the larger substituents compared to **4** and **5**. Nevertheless, the interplay between the bridging boron atom and the iron centers appears to be very pronounced, while repulsive Fe–Fe interactions overbalance attractive ones.

In addition to the QTAIM, ELF and MO studies, NPA charges have been obtained to examine the extent of charge transfer from and to the bridging moieties (Table 5.3). Firstly, it is quite interesting to note that only **2** exhibits a negatively charged bridging ligand. All other complexes feature positively charged bridging entities, although a very low charge sum (0.065 e) is observed for PH_2. In terms of charge transfer, the metal

centers within **2** shift charge *to* the bridge, while the complexes **3**-**5** feature an opposite transfer *from* the bridge to the metal atoms. This may be attributed to the more efficient back-donation occurring in Fe–P and Fe–B interactions compared to the Fe–S bonds, and is in line with the findings obtained from MO investigations. Nevertheless, in all cases a negative charge is observed for the iron centers, ranging from -0.119 e (**3**) to -0.330 e (**5**).

Table 5.3. NPA charges for compounds **2**-**5** in [e].

Compound	Fe	Σ_{Ligand}	monodentate ligand equivalent[a]
2	-0.146	-0.201	-0.101
3	-0.119	0.464	0.232
4	-0.320	0.065	0.065
5	-0.330	0.158	0.158

[a]Since some of the employed ligand systems are bidentate, their total charge sum Σ_{Ligand} has been halved to obtain a mono-dentate charge equivalent, which is comparable to the monodentate species PH_2 and PF_3.

5.4 Conclusions

In summary, a series of structural arrangements and bridging ligands has been investigated in this chapter. The influence of the bridging motif has been studied along the bridged-to-terminal conversion path in $[Fe_2(CO)_9]$ (Chapter 5.2). Additionally, the effect of the ligand nature itself has been examined in a number of dimeric iron complexes bridged by CO, borylene, phosphorus and sulfur ligands (Chapter 5.3). The established assumption of a competitive interplay between direct metal–metal bonding and through-bond interaction *via* the bridge is supported by many indications discussed on the previous pages. Whenever the bridging arrangement and the overall binding strength of the bridging ligand ensures the metal–metal interaction *via* the through bond mechanism, the direct M–M interaction is overwhelmed and no M–M bond path is detected (e.g. in **1**, **3** and **4**). However, if the symmetric bridging situation is disturbed (artificially be fixed coordinates or due to the nature of the ligand e.g. in **5**) or the interaction between metal centers and bridging entity weak in terms of unfavorable orbital interplays and less effective back-donation, the through-bond mechanism succumbs and a M–M bond path is observed.

Chapter 6

Extension of the Fischer/Schrock Concept from Carbenes to Borylenes

In the previous chapter (Chapter 5), the stabilization of the highly reactive class of borylenes within the coordination sphere of transition metals has already been presented. In view of the variety of reported synthesized transition metal borylene complexes, the thermodynamic stability of these compounds is now well established.[1-3] In addition, the M–BR bond has been found to be even more stable against homolytic dissociation than comparable M–CO interactions.[4] However, due to the high polarity within most boron ligand systems and the small HOMO-LUMO gap,[4, 5] borylene complexes are often reactive towards nucleophiles and hence kinetically labile. Thus, borylenes have to be stabilized by either electron releasing or bulky substituents. While steric protection is mainly provided by the transition metal fragment, electronic stabilization originates predominantly from π donating substituents.[3] In this context, the class of aminoborylenes BNR_2 (R=CH_3, $SiMe_3$) has been found to offer interesting qualities in

terms of steric protection by bulky substituents (e.g. $SiMe_3$ groups) and enhanced ligating properties. The HOMO energy of BNR_2 is further increased compared to the ubiquitous CO ligand, while two appropriate non-degenerate π orbitals are available (for details see ref. [4]). Hence, back-bonding from the metal center can occur *via* an in-plane or out-of-plane orbital combination, yet is competing with the B=N double bond (s. Scheme 6.1). It has been stated that this might be the reason why aminoborylenes act primarily as σ donors and less as π acceptors, compared to borylenes with weak π donating substituents like BCH_3.[6] Generally, the BR σ donation dominates over transition metal back-bonding, when the substituent R at the boron atom is a strong π donor. In these cases, the bonding is mainly determined by Coulombic attraction between the charge provided by the boron center and the Lewis acidic metal fragment.[7] However, M→B–R π back-donation becomes significantly larger and may even overwhelm R–B→M donation for the cases of R being a weak π donor. Nevertheless, also for these boron–metal interactions, covalent bonding contributions seem to be less important compared to charge attraction between Lewis acid and base. In summary, the HOMO of B–R features distinct lone pair character enabling excellent σ donation, while the nature and π accepting capabilities of the LUMO depend on the conjugative abilities of the substituent R.[7-9]

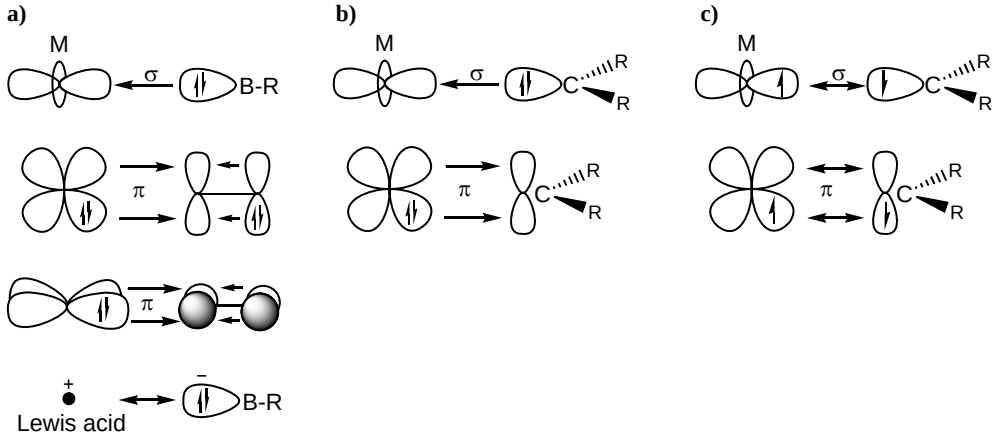

Scheme 6.1. Schematic representation of the dominant orbital interactions for a) transition metal borylenes with π donor substituents, b) Fischer carbenes and c) Schrock carbenes according to ref [8].

6.1 Computational Details

All single point calculations were performed at the B3LYP/TZVP[10-14] level of theory using the Turbomole package[15-17] (version 5.10), based on coordinates obtained from X-ray diffraction studies. The electronic structure analyses were performed at the density functional theory level. Initially, the gradient-corrected functional BP86,[18-20] the B3LYP[10-13] hybrid functional and the BHLYP[21] hybrid functional were compared. As the basic topology of charge density and ELF did not depend on the functional, we report only the B3LYP results. Charge-density analyses used the AIM2000 program package.[22] The ELF[23] was analyzed with the ToPMoD[24, 25] program.

6.2 Fischer and Schrock Carbenes

Initial calculations on carbenes suggested the singlet configuration of the borylene ground state regardless of the substituent R.[4] In combination with the excellent σ donor capabilities of BR and the lone-pair-shaped HOMO, the transition metal–boron bond was thus classified as donor-acceptor interaction, while "true" double bonding was excluded.[6] A comparable situation is found in Fischer-type carbene complexes, in which the singlet carbene donates electrons into an empty d_{z^2} metal orbital and accepts electron density from d_{xz}(M) into its LUMO (see Scheme 6.1). In contrast, carbene fragments of Schrock complexes exhibit a triplet spin state, and feature true double bonding in the sense of actual electron pairing. Following the Fischer/Schrock concept, carbenes are classified based on their substituents, generation and the nature of the transition metal, in order to gain a qualitative classification of their bonding.[26, 27] Fischer-type complexes most commonly contain late transition metals of low oxidation states (e.g. in transition metal carbonyl compounds) and prototypically feature π donor carbene substituents. *Per contra*, Schrock complexes commonly consist of early transition metals in high oxidation states (e.g. polyfluorinated tungsten complexes) and a carbene center with adjacent σ or weak π donors (e.g. halogens). The individual kinds of M–C interaction have been taken into account to explain the qualitatively different chemical behavior of both classes of carbenes. While carbene ligands in Fischer complexes react as electrophiles (as do most of the borylenes, *vide supra*), Schrock complexes exhibit nucleophilic carbene centers. In this context, the dominant influence of the nature and oxidation state of the transition

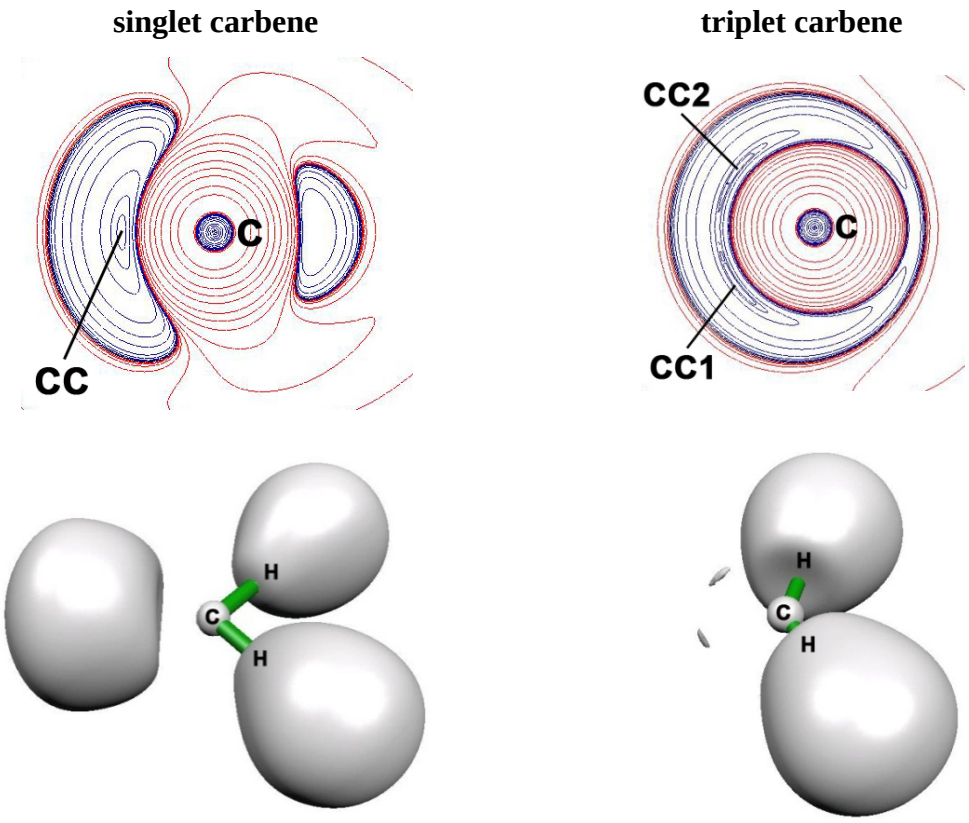

Figure 6.1. Laplacian contour plots (contour plane is perpendicular to H–C–H plane; charge accumulations ($\nabla^2\rho < 0$) are printed in blue, charge depletions ($\nabla^2\rho > 0$) in red; CC: charge concentration) and ELF isosurfaces (singlet carbene: isovalue 0.95; triplet carbene: isovalue 0.815) of singlet and triplet carbene.

metal on the M–C bond, and hence the reactivity, has been emphasized by theoretical as well as experimental work.[27-31] However, it has also been pointed out that the oxidation state of the metal alone is not a reliable criterion for predicting electrophilic or nucleophilic reactivity.[32] Therefore, further criteria for the classification of Fischer and Schrock carbenes with respect to their chemical behavior have to be taken into account.

In addition to MO analyses, carbenes have also been investigated by topological analysis of their charge density distribution and significant differences have been found in the Laplacian distribution of Fischer and Schrock carbenes.[33] In précis, Fischer complexes exhibit less covalent bonding, lower double bond character and bond orders in line with the classification of donor-acceptor interactions. The Fischer-type carbene centers feature charge depletions in the π plane, perpendicular to the plane defined by M–CR_2, while Schrock complexes provide increased covalent bond character and larger

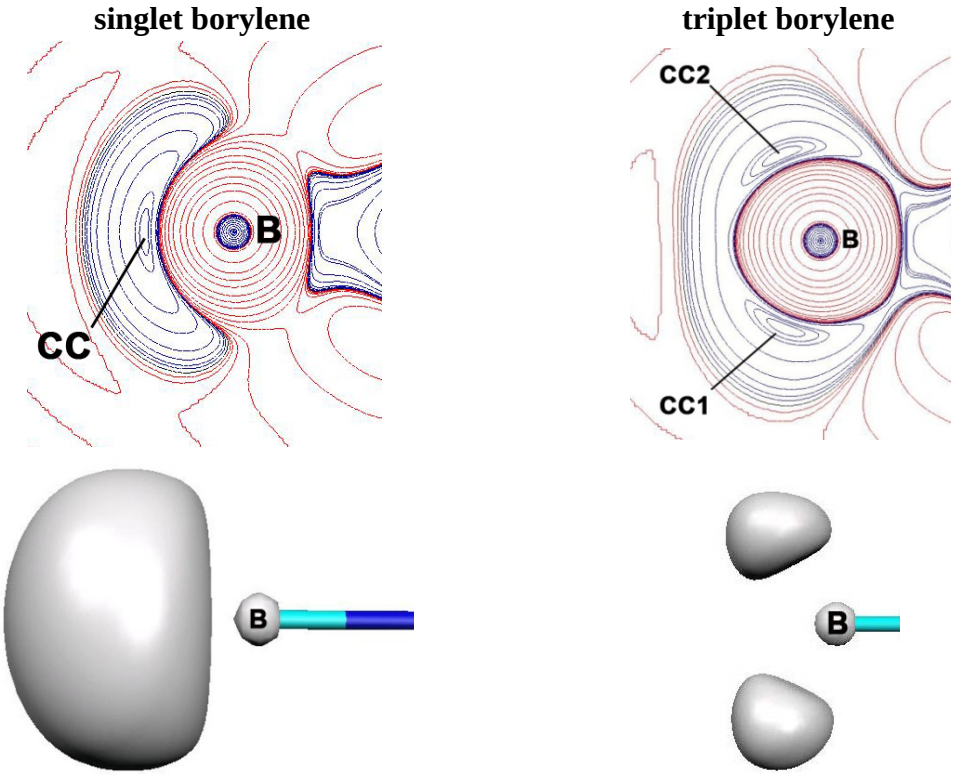

Figure 6.2. Laplacian contour plots (contour plane is perpendicular to $BNSi_2$ plane; charge accumulations ($\nabla^2\rho < 0$) are printed in blue, charge depletions ($\nabla^2\rho > 0$) in red; CC: charge concentration) and ELF isosurfaces (singlet borylene [$BN(SiMe_3)_2$]: isovalue 0.95; triplet borylene: isovalue 0.87) of singlet and triplet borylene.

bond orders. Furthermore, the charge concentration in Schrock carbene complexes is significantly increased in the p(π) direction and the carbene center appears shielded by charge density in the π plane.[33-35] Hence, in reverse, the prediction of chemical behavior and thus the classification along the Fischer/Schrock concept is also possible *via* topological analysis.

6.3 Comparison between Singlet and Triplet Borylenes and Carbenes

According to the Fischer/Schrock system, most of the obtained borylene complexes may be classified as Fischer-type according to the borylene-substituents and the nature of the transition metal. In addition, bonding patterns as well as chemical reactivity of most borylenes are in line with those observed for Fischer carbenes. Hence, one may ask if (1) a classification of borylenes in analogy to Fischer/Schrock carbenes is possible, and, closely related, if (2) Schrock-type borylenes can be prepared.

Aiming for an answer to both questions, the isolated singlet and triplet species of carbenes and (amino)borylenes have been investigated by means of QTAIM and ELF analysis to scrutinize similarities as well as differences. From Figures 6.1 and 6.2 the remarkable resemblance between carbenes and borylenes in the individual spin states becomes apparent. The singlet carbene, as well as the corresponding borylene, features a single VSCC which may be interpreted as the σ donating, lone-pair shaped HOMO. In addition, a corresponding ELF attractor is found for both species with an integrated electron density of 2.13 eÅ^{-3} and 2.16 eÅ^{-3} for the carbon and boron atoms, respectively. Furthermore, the area of charge depletion enabling nucleophilic attack appears in both Laplacian distributions.

In contrast, the triplet analogues feature two VSCCs as well as two ELF attractors. For the carbon species, the individual ELF attractors integrate to 0.77 eÅ^{-3} and 0.78 eÅ^{-3}, while the corresponding boron basins feature an increased integrated density of 1.05 eÅ^{-3} and 1.06 eÅ^{-3}. In view of the orbital scheme for Schrock carbenes (see Scheme 6.1), this corresponds well to two separated electrons for actual double bonding with the metal fragment. As mentioned before, the triplet carbon atom appears shielded by charge density in the Laplacian distribution, in line with the weak or non-electrophilic reaction behavior. Similarly, the boron center is enclosed by an area of continuous charge concentration, although the VSCCs appear distinctly more separated in the borylene case.

6.4 Exemplary Fischer- and Schrock-type Borylene Complexes

From comparing ELF and QTAIM results for the singlet and triplet configuration of the isolated carbenes and borylenes, the analogy between both families of compounds (when of equal spin state) appears strikingly obvious. Hence, from a conceptual point of view, the formation of Schrock-type borylene complexes featuring similar properties and bonding patterns compared to the carbene species should be possible. However, the task of preparing actual Schrock-type borylene compounds seems to be challenging due to inherent limitations in the synthetic routes normally employed for the formation of borylene transition metal complexes.[3, 36] While Schrock-type carbene compounds are most commonly obtained via α-H abstraction,[27] this may not be feasible with highly Lewis acidic borylene sources. However, very recently, Sabo-Etienne and coworkers presented the preparation of a borylene by double α-H migration from a borane complex

and loss of H_2, which may be an elegant possibility to obtain Schrock-type borylenes.[37] Alternatively, Schrock-type borylenes may be available *via* borylene transfer to early transition metals in high oxidation states with free coordination sites.[38] So far, this challenge has only been met by means of matrix isolation techniques; F_2TiBF, **6**, was prepared and characterized very recently *via* infrared spectroscopy.[39] In accordance with the QTAIM and ELF results for the isolated triplet borylene, **6** features two VSCCs and ELF attractors (results not shown). The ELF basins corresponding to the supposed metal–boron double bond integrate to 1.50 eÅ^{-3} and 1.54 eÅ^{-3} each, and hence agree well with two electron pair bonds. Furthermore, the Laplacian distribution exhibits the typical characteristics associated with Schrock-type carbenes or borylenes.

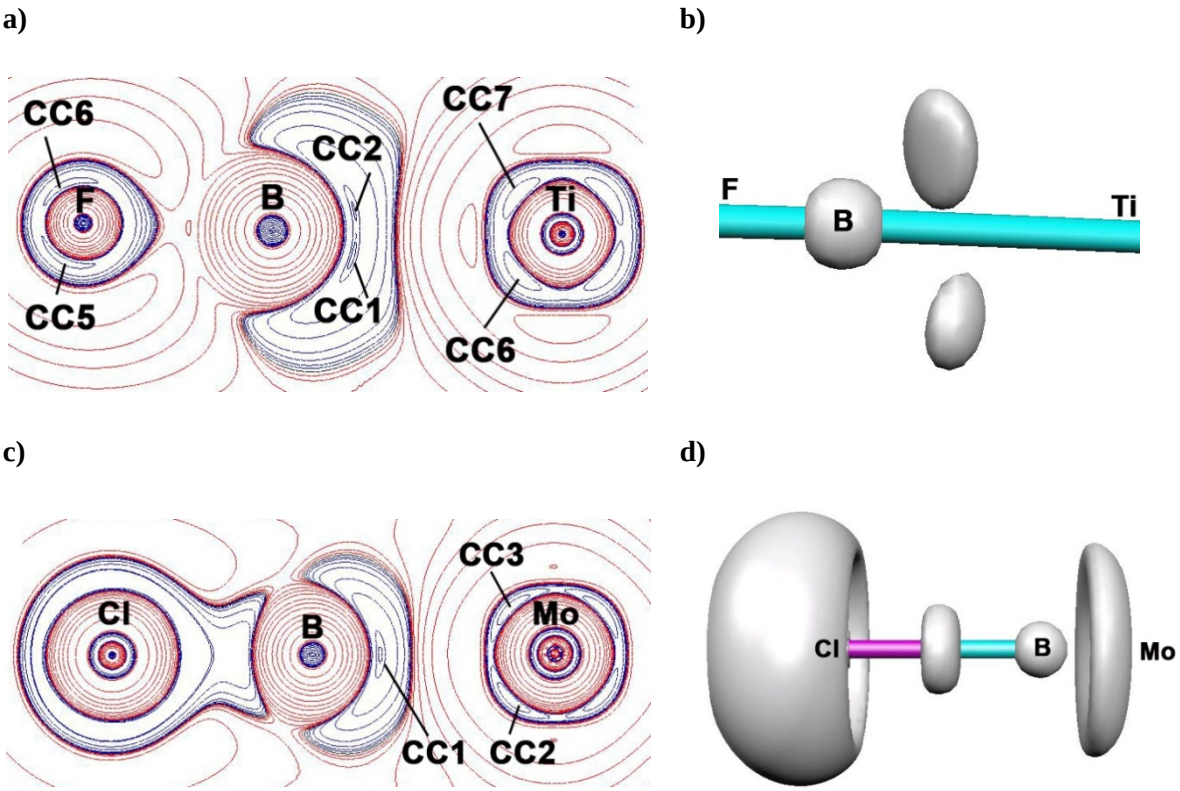

Figure 6.3. Laplacian contour plots (charge accumulations ($\nabla^2\rho < 0$) are printed in blue, charge depletions ($\nabla^2\rho > 0$) in red) and ELF isosurfaces (η=0.95 and 0.85 for b) and d), respectively) of a,b) Cp_2TiBF (**7**) and c,d) $(OC)_5MoBCl$ (**8**).

Based on the structure of **6**, modified titanium complexes were investigated such as Cp_2TiBF (**7**), $(CH_3)_2TiBF$ and F_2TiBNH_2, all of them showing Schrock-type ELF and QTAIM characteristics. In particular, **7** shall be discussed in detail, since promising attempts have already been undertaken to prepare similar derivatives.[38] In Figure 6.3a

and b, the two VSCCs (CC1 and CC2) and corresponding ELF attractors are depicted, respectively. Furthermore, the charge concentrations of the boron-bound fluoride lone pairs (CC5 and CC6) as well as polarized valence density around the titanium atom can be observed (Figure 6.3a). However, compared to the free triplet borylene, the boron center in **7** appears less shielded by charge density, which may also be caused by the highly electronegative fluoride substituent. The integrated densities of the two ELF basins associated with the Ti–B double bond integrate to 1.43 eÅ^{-3} and 1.53 eÅ^{-3} and are thus close to values expected for two electron pair bonds.

A sizeable variety of (presumably) Fischer-type borylene complexes have already been obtained and crystallographically characterized, among them $M(CO)_5BN(SiMe_3)_2$ (M = Cr, Mo, W),[40] $M(CO)_5BSi(SiMe_3)_3$ (M = Cr, Mo)[41] and $MnCp(CO)_2B^tBu$[42]. For convenience and to stay within the Fischer scheme, a pentacarbonyl molybdenum fragment was chosen and combined with a simple chloride-substituted borylene, i.e. $Mo(CO)_5BCl$ (**8**). The analogous *tert*-butyl derivative, $Mo(CO)_5B^tBu$, has also been analyzed, yielding almost identical results, which are thus omitted. In contrast to **7**, the Fischer-type complex **8** exhibits only one VSCC pointing from the boron center towards the metal atom and a single, ring-shaped ELF attractor (see Figure 6.3c and d, respectively). The polarization within the valence and penultimate shell of the molybdenum center (CC2 and CC3) is comparably pronounced in comparison to Figure 6.3a (CC6 and CC7), and may thus simply be attributed to the symmetry lowering within the ligand field in both cases. Furthermore, the domains of charge depletion around the boron atom, which have been very pronounced for the isolated singlet borylene, appear decreased, probably due to the diffuse charge density provided by the chloride substituent. Interestingly, no single ELF attractor is found corresponding to the VSCC, but instead a ring-shaped basin was observed comparable to results observed for $Cr(CO)_5BSi(SiH_3)_3$.[40] However, an integration of the corresponding ELF domain has been problematic due to the ambiguous assignment of electron density to the ring region. Hence, no electron density values can be provided here. Nevertheless, from comparing the plots within Figure 6.3, a chemically significant difference between both types of borylenes can be detected, despite their very similar halogenide substituent. Thus, the discrepancies between both complexes **7** and **8** are predominantly caused by the nature and oxidation state of the coordinated metal fragment.

However, within these studies a series of compounds (carbenes as well as borylenes) have been examined which feature contradicting ELF and QTAIM results, thus precluding a classification along the introduced guidelines. The origin of these ELF/QTAIM discrepancies may be various, including shortcomings in the theoretical setup of both approaches (see also Chapter 1.2). These deviations themselves are interesting from a methodological point of view. However, they eliminate a broad application of QTAIM and ELF for the classification of borylenes and carbenes. Nevertheless, the cognate nature of borylenes and carbenes is emphasized by the presented data and the possible existence of Schrock-type complexes may establish a new area of research within borylene chemistry. Hence, obtaining definitive synthetic proof for the existence of "Schrock"-borylenes remains a challenging task for ongoing experimental work within the field of boron transition metal chemistry.

6.5 Outlook

In summary, the striking similarities between the QTAIM and ELF features of isolated carbenes and borylenes with respect to their spin state have been illustrated. Although the preference for the particular spin configuration strongly depends on neighboring substituents, the formation of both borylene species should be possible in analogy to carbenes. Hence, boron and carbon species should exhibit comparable bonding patterns in terms of Fischer- or Schrock-type interactions with respect to adjacent substituents and the nature and oxidation state of the transition metal. An extension of the Fischer/Schrock concept from carbenes to borylenes should therefore be possible, enabling an easy classification of bonding and a prediction of their reactivity patterns. The differences between Fischer- and Schrock-type borylene complexes have been discussed in terms of their ELF and QTAIM characteristics and convenient, chemically significant criteria have been provided for distinguishing the respective bonding types.

Chapter 7

Dependency of AIM and ELF Results for Bonding Analyses on Exchange Correlation Functional

As discussed in the previous chapters, boron containing ligands are well suited for transition metal coordination due to their high similarity compared to their carbon equivalents, and especially the ubiquitous CO ligand. The isoelectronic relationship between many boron and carbon ligand systems results in resembling structural motifs, observed for both, carbon and boron transition metal compounds.[1-5] In the following chapter, we concentrate on the comparison between carbene and borylene bridged dinuclear manganese complexes,[6, 7] to understand the underlying differences and similarities in terms of bonding patterns. Very recently, an experimental electron-density (ED) study has investigated the electronic structure of [{(η^5-C_5H_5)$(OC)_2Mn$}$_2$B−*t*Bu] (**9**).[8, 9] Analysis of the charge density of **9** by Bader's Quantum Theory of Atoms In

Molecules[10] (QTAIM) suggested not only the absence of a direct Mn–Mn bond expected from the 18-valence-electron rule, it also indicated two Valence Shell Charge Concentrations (VSCCs) connecting the bridging boron atom to each of the two manganese centers.[9] According to the interpretation of VSCCs in terms of lonely and bonding electron pairs (Chapter 2), this would more consistent with a substituted borane than with the expected delocalized borylene description of the bridging ligand (analogous to bridging carbonyl ligands[11]).

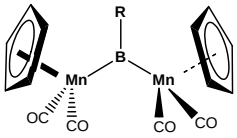

9; R = $C(CH_3)_3$

10; R = $N(CH_3)_2$

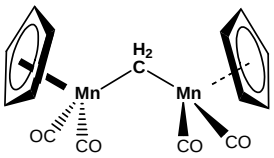

12

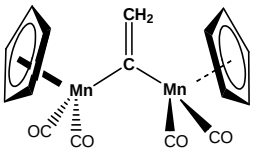

11

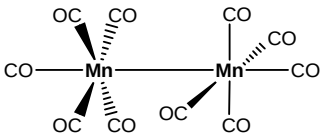

13

Given the prototype nature of **9** as complex with a bridging boron ligand, and the somewhat unexpected results of the experimental QTAIM study (accompanied by computations at the BP86/TZVP level),[9] we provide here a systematic computational study on **9** and its homologous amido-substituted complex **10**.[6, 7, 9, 12, 13] as well as the closely related carbon-bridged complexes **11**[14] and **12**. Historically, **11** represents the first methylene-bridged complex ever obtained,[15] and its early electron-density measurement has been interpreted to exhibit a direct Mn–Mn bond[16] (this Mn–CH_2–Mn moiety has been taken as a prototypical dimetallacyclopropane ever since; see also ref. [17]). Complex **12** in turn represents a related prototypical vinylidene-bridged complex. We compare the electronic structure and bonding features of these four bridged complexes, taking the unsupported dinuclear $Mn_2(CO)_{10}$ complex **13** as a reference with a direct Mn–Mn bond. We employ various methods such as QTAIM, the Electron Localization Function (ELF[18, 19]), and Natural Population Analyses (NPA[20]), based on density functional calculations to study the fine changes in the electronic structures. Our aim is to answer the following questions:

a) Is there a direct metal-metal bond in any of the complexes **9**-**12**? There has been substantial discussion of the question of metal-metal bonding in supported multinuclear carbonyl complexes,[21-25] also with bridging alkyne ligands,[26, 27] and both QTAIM and ELF have been employed in this context.[11, 26-36].

b) Is the bridging ligand in **9** or **10** a borylene with three valences, or does the bridge exhibit two well-defined localized two-center bonds, as suggested by the two VSCCs between the bridging boron and the two manganese atoms observed[9] experimentally for **9**? In view of the isoelectronic relationship, this question has also to be answered for the methylene and vinylidene bridges in **11** and **12**? It turns out that the interpretation of these questions depends in an unexpected way on the computational level (choice of exchange-correlation functional) employed, and we thus compare different methods (chapter 7.2.2 and 7.2.3).

c) Finally, we wish to compare the donation and back-donation from and to the bridging ligand for **9**-**12**, in the context of a classification of the binding ability of boron- vs. carbon-centered bridging ligands,[37] and in view of the competition between bridge and direct metal-metal bonding.[11]

7.1 Computational Details

All structure optimizations and harmonic frequency analyses were performed at the B3LYP/TZVP[38-42] level of theory using the Turbomole package[43-45] (versions 5.8 and 5.9). As starting point for the structure optimizations we used either coordinates from X-ray diffraction studies directly, or modified them to construct structural derivatives.

For the electronic structure analyses, subsequent single-point calculations were performed. In view of qualitative discrepancies of our B3LYP/TZVP data with the results of the experimental QTAIM study[9] (see below), we carried out further analyses with the gradient-corrected non-hybrid functionals BP86[46, 47] and BLYP,[40, 41, 46, 48] with the BHLYP hybrid functional[48] incorporating as much as 50% Hartree-Fock exchange. Addition of an f-function for the manganese atoms (TZVPP basis) changed the results negligibly (data not reported). Also, structures optimized with the other functionals

(BP86, BLYP, BHLYP) give almost the same QTAIM and ELF results (data not shown) as the B3LYP/TZVP structures, and we can thus restrict our discussion to the latter.

QTAIM analyses used the AIM2000[49] program package, whereas the ELF was analyzed and computed with a locally modified version of the TopMod program.[50, 51] The ELF isosurfaces were visualized with the Molekel software.[52] Natural population analyses[20] were performed with Turbomole 5.9.

7.2 Optimized Structures

The recurring entity of the complexes **9** to **12** is the dicarbonyl-cyclopentadienyl manganese unit, which is related to the remaining organometallic fragment by a C_2 symmetry operation in the *trans* isomers studied. The well-studied reference compound **13** exhibits overall crystallographic C_2 symmetry, but the computations converge to a more symmetrical D_{4d} structure. All computed distances and angles are within acceptable

Table 7.1. Selected distances (in Å) for the B3LYP/TZVP-optimized structures.

Compound		Theory	Experiment
9	Mn···Mn	2.841	2.78190[a]
	$Mn–B_{bridge}$	2.037, 2.034	2.0215, 2.0206[a]
	B–C	1.614	1.6092[a]
10	Mn···Mn	2.857	2.790[6]
	$Mn–B_{bridge}$	2.047, 2.048	2.03, 2.03[6]
	B–N	1.404	1.39[6]
11	Mn···Mn	2.836	2.799[16]
	$Mn–C_{bridge}$	2.026, 2.025	2.026[16]
12	Mn···Mn	2.806	
	$Mn–C_{bridge}$	1.981	
	C_{bridge}=C	1.326	
13	Mn···Mn	3.034	2.9042[32], 2.9078[54]

[a] Supporting material in ref. [9].

deviation from the available crystallographic data, and the structures are confirmed as minima on the potential energy surface. The dimanganese decacarbonyl, **13**, is probably the paradigmatic example of an unsupported Mn–Mn single bond (but note that some 1-3 interactions have been discussed even in this case[11, 32]). Its Mn–Mn bond length will be the reference value, ranging between 2.903 Å and 3.033 Å,[32, 53, 54] dependent on the means of determination (see also Table 7.1). Obviously, measured and optimized Mn–Mn distances of the bridged compounds **9** to **12**[6, 13] are all significantly shorter and range from 2.806 Å to 2.857 Å. Together with the 18-valence-electron rule, this has been the main reason for the assumption of a direct metal-metal bond in these and related complexes.

7.3 QTAIM Analysis

B11LYP/TZVP results. Figure 1 provides molecular graphs and $\nabla^2\rho$ contour plots for **9-13** obtained with the B3LYP hybrid functional. We note first of all, that no Bond Critical Point (BCP) and thus no bond path is found between the two manganese atoms for any of the bridged systems **9-12**, in contrast to the unsupported bond in reference complex **13**. The Mn–Mn midpoint is located in an area of positive $\nabla^2\rho$ and low ρ in all bridged systems **9-12**. This agrees with the experimental results for **9**[9] and is consistent with the good bridging abilities of both borylene- and carbene-type ligands.

It is a general observation in QTAIM analyses of (so far carbonyl- or alkyne-bridged) di- or oligonuclear carbonyl complexes[11, 26, 27, 30] that direct metal-metal bonds compete with delocalized bonding via the bridge, and strong symmetrical bridges with good π-acceptor ligands tend to exclude direct M–M bonds (the same holds for results obtained with ELF[34, 55]). The VSCCs associated with the bridged bond are connected to the bridging ligand in all cases. Delocalized bonding via the bridge dominates thus clearly over the direct Mn–Mn bonding in all of **9-12**, in contrast to **13**. The latter has a negative Laplacian at the BCP (which exists on the straight Mn–Mn connection line, cf. Figure 7.1) but with a clear local maximum in $-\nabla^2(\rho)$, comparable to F_2[8] (see extensive discussion of the bonding in **13**,[28, 32, 33, 53, 56] as reviewed also in ref. [11]). We will see below that the ELF analyses provide a similar picture. There have been arguments that

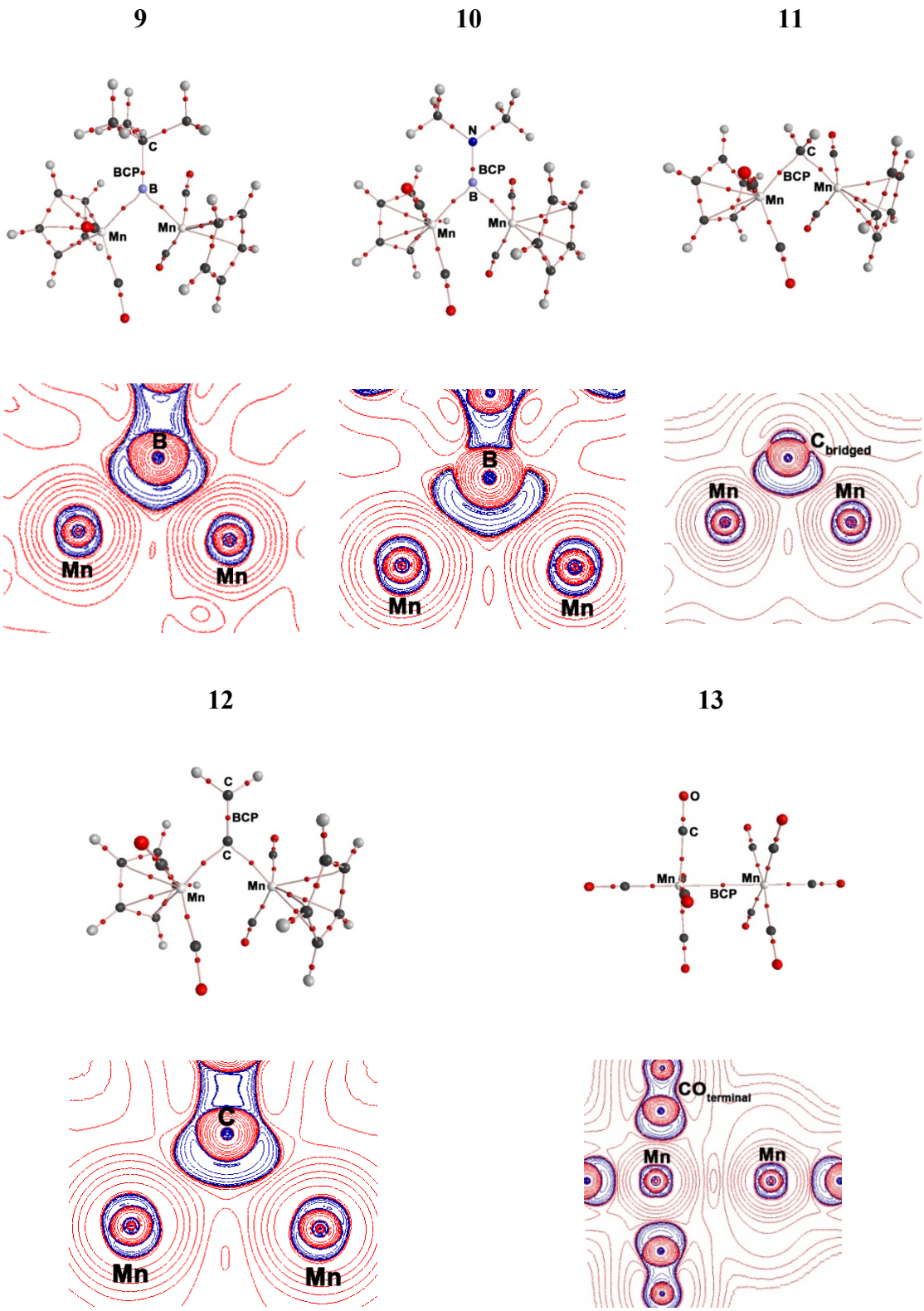

Figure 7.1. Molecular graphs and Laplacian maps; BCPs are indicated as red dots; charge accumulations ($\nabla^2\rho < 0$) are printed in blue, charge depletions ($\nabla^2\rho > 0$) in red. B3LYP/TZVP results.

weak M–M interactions may nevertheless be present but may not be identified using the standard instruments of QTAIM (but with alternative instruments like plots of the total energy density or the source functions, or orbital decomposition of the electron density).[26, 27, 29, 35, 36, 57] Inspection[9] of the source function for **9** indicated strongly delocalized bonding, and the ratio |V|/G was low. For the present discussion it suffices to note that bonding via the bridge dominates in all four cases, as the electrons from those metal d-orbitals potentially able to establish a direct Mn–Mn bond instead are delocalized mostly into the acceptor orbitals of the bridge. In this, the four ligands studied here resemble bridging carbonyl or alkyne ligands.[11, 21-36] Note that the density topology in small ring systems may also be influenced by the core densities of the atoms in the perimeter.[58]

Table 7.2. BCP properties of selected bonds.

Compound	Interaction	ρ [eÅ^{-11}]	$\nabla^{10}\rho$ [eÅ^{-13}]
9	Mn–B	0.658	–0.004
		0.662	–0.004
10	Mn–B	0.642	0.158
		0.640	0.165
11	Mn–$C_{bridged}$	0.685	3.452
		0.685	3.446
12	Mn–$C_{bridged}$	0.739	4.155
		0.739	4.171
13	Mn–Mn	0.160	0.119

The bond paths between the bridging atom and the two manganese centers in **9** to **12** exhibit a pronounced inward curvature at the bridging atom (s. Figure 7.1). This is known to indicate bond delocalization[10] and is thought[59, 60] to be related also to the donation of charge density from the bridge to the two metal centers. Near the manganese centers, the bond paths are almost linear. This cannot be taken to indicate low back donation, as the relevant manganese d-orbitals point almost completely into the direction of the bridging ligand. The values of $\rho(\mathbf{r}_{BCP})$ and $\nabla^2\rho(\mathbf{r}_{BCP})$ for these bonds are in all cases slightly asymmetric for the two Mn–B sides (no symmetry constraint was applied during the optimization). Borylene complex **10** has small negative $\nabla^2\rho(\mathbf{r}_{BCP})$ values, complex **9** equally small positive ones at the BCPs. Both manganese-boron interactions may thus be

taken as borderline cases between closed-shell dative and covalent shared bonding. The M–C_{bridge} bonds in **11** and **12** exhibit comparable values of $\rho(\mathbf{r}_{BCP})$ and $\nabla^2\rho(\mathbf{r}_{BCP})$. The latter ones are positive, which would be consistent with more ionic Mn–C bonds in **11** and **12** than Mn–B bonds in **9** and **10** (see also below). We note in passing the expected,[11] relatively pronounced positive $\nabla^2\rho(\mathbf{r}_{BCP})$ values for terminal dative carbonyl metal-ligand interactions.

For the complexes **9**, **11**, and **12**, the B3LYP/TZVP calculations provide one VSCC near the bridging atom, pointing towards the Mn–Mn midpoint. This is similar to the QTAIM description of bridging carbonyl[11, 30, 31, 56] and phosphane[55] ligands but clearly contradicts the experimental QTAIM results for **9**, which provided two B–Mn bond VSCCs, each one of them pointing from the bridging boron atom towards one of the Mn centers.[9] While the experimental study is thus more consistent with a description of the bridging ligand as a substituted borane, the B3LYP/TZVP picture is that of a delocalized three-center bond of a genuine borylene. Interestingly, the calculations do provide two B–Mn VSCCs for **10**. That is, the result is already in tune with the substituted-borane approach. However, the separation between the two attractors in $\nabla^2\rho$ is only marginal (see below). We will discuss below that the actual interpretation obtained by theory for **9**, **10**, and **12** depends remarkably on the computational level. At all levels, an additional VSCC is located between the bridging atom and each of its substituents (two in case of the CH_2 bridge in **11**).

In agreement with the experimental QTAIM study of **9**,[9] the valence shells of the metal atoms in **9** to **12** feature six VSCCs in an octahedral configuration with one of the edges of the octahedron pointing towards the cyclopentadienyl ligand. All other ligands face regions of charge depletion. This is interesting, as within QTAIM the cyclopentadienyl ligand behaves thus topologically as a single (six-electron) donor ligand. We note in passing that, in agreement with previous work,[11] eight VSCCs in a distorted cubic arrangement are found for each manganese atom in **13**.

Dependence on exchange-correlation functional. Given the discrepancy between the number of computed (B3LYP/TZVP) and experimentally obtained B–Mn bonding VSCCs in **9**, we have compared charge densities obtained with different functionals (BP86[46, 47], BLYP[40, 41, 46, 48], B3LYP[38, 40, 41] and BHLYP[40, 41, 48]). It is

known that the local density approximation (LDA) and the generalized gradient approximation (GGA) tend to suffer from self-interaction errors and provide metal-ligand

Table 7.3. Number of attractors in $-\nabla^2\rho$, with $\nabla^2\rho$ values, and separatrix $\nabla^2\rho$ values (in eÅ^{-5}) for the di- or trisynaptic VSCCs at the bridge.[a]

VSCC	$\nabla^2\rho$ values	BP86	BLYP	B11LYP	BHLYP
9[b]	separatrix	*2*: –5.561, –5.359	*2*: –5.896, –5.683	*1*: –6.287	*1*: –7.554
	attractor	–5.324	–5.663		
10	separatrix	*2*: –5.247, –5.226	*2*: –5.566, –5.546	*2*: –5.769, –5.788	*1*: –6.871
	attractor	–4.872	–5.218	–5.699	
11	separatrix				
	attractor	*1*: –14.863	*1*: –15.740	*1*: –16.639	*1*: –18.973
12	separatrix	*2*: –16.466, –16.478	*2*: –17.210, –17.222	*1*: –18.281	*1*: –20.757
	attractor	–16.406	–17.178		

[a]B3LYP/TZVP structures. Number of attractors in italics. [b]Experimentally determined values for 1 are:[9] –7.493 eÅ^{-5} and –6.566 eÅ^{-5} for the two VSCCs and –4.868 eÅ^{-5} for the separatrix.

bonds in transition-metal complexes with an overestimated covalent character.[61-64] On the other hand, the semi-local exchange holes of GGA-type functionals like BP86 or BLYP are also thought to simulate non-dynamical correlation (Chapter 1).[62, 65] Hence, exact-exchange admixture renders the bonds more polar but may also reduce the amount of non-dynamical correlation simulated. It should be noted that there is no clear preference in the literature for one type of functional when it comes to transition metal systems. The abovementioned balance between minimal self interaction and adequate simulation of nondynamical correlation is difficult to achieve. While B3LYP is clearly the most popular functional in main group chemistry (albeit it also has been shown to exhibit severe shortcomings even in organic chemistry), it appears that the optimum amount of exact-exchange admixture varies for different systems and different properties

(see, e.g., discussions in refs. [27, 64, 66-72]). B3LYP incorporates 20% and the BHLYP functional 50% HF exchange, and thus a comparison of these two hybrid functionals with the BP86 and BLYP GGA functionals should provide insight to an interrelation between charge transfer between metal and bridging ligand (and *vice versa*) and the computed features in $\nabla^2\rho$.

The number of VSCCs for Mn–L_{bridge}–Mn bonding depends on this exact-exchange admixture for all bridged complexes but **11** (Table 7.3). At all levels, the latter methylene-bridged complex exhibits only one VSCC, consistent with the delocalized three-center bonding picture that is common also for bridging carbonyl ligands.[11, 30, 31, 56] In contrast, with GGA functionals (BP86, BLYP), complexes **9** and **12** feature two VSCCs and thus a localized two-center bonding picture. Exact-exchange admixture changes this to a delocalized picture with one VSCC already at B3LYP level (and also with 50% exact exchange at BHLYP level). Finally, the amido-substituted borylene complex **10** has two VSCCs at B3LYP *and* BLYP, BP86 levels, and switches to one VSCC only at BHLYP level (pure HF results give the same qualitative topology as BHLYP for all complexes; data not shown). In all bridged complexes except **11**, the Laplacian distribution near the bridging ligand appears thus borderline between one and two VSCCs, thereby explaining the unusual dependence on the exchange-correlation functional. Apparently the nuclear configurations of complexes **9**, **10**, and **12** are close to a catastrophe point within Bader's topological theory of molecular structure, indicating a borderline between two topologically different bonding situations.[10, 73] A somewhat related situation has very recently been observed for the Co-(C_2) QTAIM bond topology in an alkyne-bridged dicobalt complex, where either one or two Co–C bond paths were obtained, with qualitative differences even between closely similar, crystallographically independent molecules.[26] The topologically unstable situation was attributed to a very shallow density distribution in the Co-(C_2) triangles marking the interactions between the two cobalt centers and the bridging alkyne ligand, and it was argued that discrepancies may well be caused by measurement errors or artifacts in the multipole refinement of the experimental charge density.[26] As shown here, a bifurcating bonding situation may also cause a high sensitivity to the computational level.

The visualization as contour plot of $\nabla^2\rho$ (Figure 7.2) indicates, that the splitting into two VSCCs at BP86 or BLYP level for **9** (and also for **12**; data not shown) is not

very pronounced, certainly less so than suggested by the experimental Laplace map for **9**[9] (see footnote b to Table 7.3; note that the experimental density distribution around boron is also more asymmetric than computationally suggested). This is confirmed by the values of $\nabla^2\rho$ given in Table 7.3: In those cases where a splitting into two VSCCs occurs (**9**, **10**, and **12** with BLYP and BP86, and additionally **10** with B3LYP), the separatrix $\nabla^2\rho$ values are only slightly less negative than the attractor with the lower $|\nabla^2\rho|$ value. For **9** and **12**, the separatrix value is only about 0.02-0.06 eÅ^{-5} or 0.2%-0.7% below the attractor value (separation is somewhat clearer with BP86 than with BLYP), compared to more than 1.6 eÅ^{-5} or 25% determined experimentally (footnote b to Table 5.3). The separation is more pronounced for **10** with GGA functionals (about 6%-7% for BLYP and BP86) but becomes less with the B3LYP hybrid functional (1.2%), *cf.* Table 7.3.

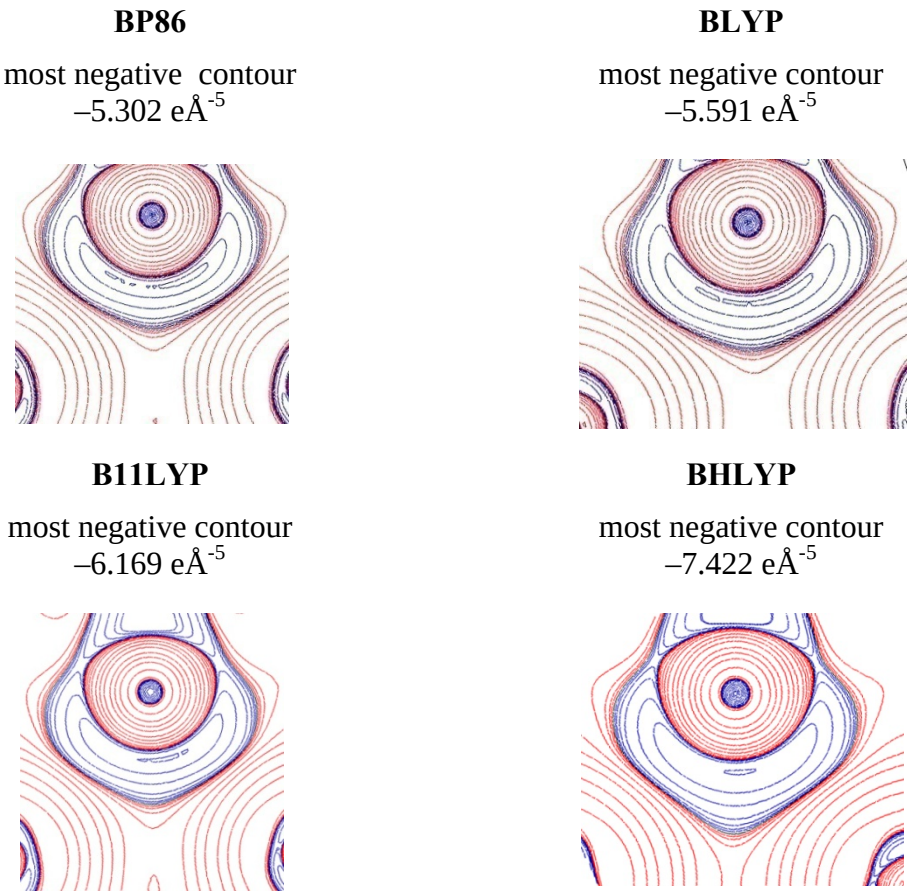

Figure 7.2. Contour plots of $\nabla^2\rho$ for **9** with different exchange-correlation functionals (the area around bridgehead atom is shown).

As we go from BHLYP to B3LYP to BP86 or BLYP, we notice furthermore that the overall region of negative $\nabla^2\rho$ becomes wider and more distinct (Figure 7.2), indicating the expected enhanced covalency at GGA level. We note also that, as the two

VSCCs present at GGA level merge into one VSCC at hybrid level, the $\nabla^2\rho$ value at the attractor of the corresponding merged basin is more negative than those at the two previously separate attractors (Table 7.3). Additionally, increased exact-exchange

Table 7.4. NPA charges for atoms and molecular fragments.[a]

		BLYP	B11LYP	BHLYP
9	Mn1[b]	–0.395	–0.397	–0.345
	Mn2[b]	–0.385	–0.386	–0.331
	B[b]	0.752	0.780	0.800
	$MnCp(CO)_2$ **9**	–0.146	–0.156	–0.160
	$MnCp(CO)_2$ **10**	–0.078	–0.085	–0.089
	B(*t*–Bu) ligand	0.224	0.241	0.249
10	Mn[c]	–0.355	–0.352	–0.295
	B	0.683	0.705	0.724
	$MnCp(CO)_2$[c]	–0.114	–0.116	–0.111
	$B(NMe_2)$ ligand	0.228	0.231	0.222
11	Mn[c]	0.058	0.058	0.056
	C	–0.529	–0.541	–0.561
	$MnCp(CO)_2$[c]	0.093	0.100	0.114
	CH_2 ligand	–0.187	–0.200	–0.227
12	Mn[c]	–0.217	–0.220	–0.223
	C	–0.034	–0.038	–0.056
	$MnCp(CO)_2$ [c]	0.181	0.121	0.127
	CH_2=C ligand	–0.237	–0.242	–0.255

[a]*Functional*/TZVP//B3LYP/TZVP results. [b]Experimental QTAIM charges for **9**[9] are –0.73 e and –0.76 e for the two Mn atoms, +1.04 e for B, and overall +0.69 e for the bridging ligand. [c]Averaged over both $MnCp(CO)_2$ fragments.

admixture renders $\nabla^2\rho$ at the single attractor more negative even for **11**, while the qualitative topology remains unchanged. We may generalize these observations by stating that exact-exchange admixture in the hybrid functionals accumulates charge in the region below the bridging atom pointing towards the Mn...Mn midpoint, at the expense of the regions close to the direct Mn-bridge connection lines.

On the other hand, a change in the number of VSCCs with different functionals is not accompanied by large changes in the BCP properties $\rho(\mathbf{r}_{BCP})$ and $\nabla^2\rho(\mathbf{r}_{BCP})$. These respond marginally, with a slightly more positive $\nabla^2\rho(\mathbf{r}_{BCP})$ value upon increasing exact-exchange admixture, consistent with the abovementioned more ionic metal-ligand bonding. Finally, it is worth mentioning, that at none of the computational levels employed, a Mn–Mn BCP appears for any of the four complexes **9-12**.

To what extent is the change in the topology of the charge density with the functional related to charge transfer from and to the bridging ligand? Table 7.4 summarizes NPA charges for the bridge and the metal fragments, as well as for manganese and the bridging atom, in **9** to **12**, comparing different functionals. We note first a pronounced inequivalence of the two metal fragments for **9**, in contrast to the other three complexes. This is related to the conformation of the alkyl substituent on boron. In case of the two boron complexes **9** and **10**, there is moderate yet notable net charge transfer from the bridging ligand to the two $MnCp(CO)_2$ moieties. This contrasts with the methylene and vinylidene complexes **11** and **12**, where charge transfer of similar magnitude occurs *to* the bridge. These observations are consistent with the more pronounced curvatures of the L–Mn bond paths at the bridging atom for **9** and **10** compared to **11** and **12** (*cf.* Figure 7.1): Significant donation from the bridge to the metal fragments is expected to enhance the curvature.[11, 9, 60]

The lower electronegativity of boron vs. carbon is particularly notable from the charge of the bridging atom itself, which is appreciably positive for **9** and **10**, strongly negative for **11** and weakly negative for **12**, reflecting charge distributions within the various bridging ligands, as well as the donation/back-donation between bridging ligand and metal fragments. With the exception of **11**, the manganese centers themselves exhibit negative partial charges, most significantly for the boron complexes **9** and **10** (Table 7.4). The extensive backbonding in **11** (and the resulting slightly positive charge on the manganeseatoms) has already been discussed previously as origin of the high stability of

the methylene-bridged complex[17, 74] (albeit under the pretext of a metallacyclopropane topology with direct M–M bond). Bridging carbene ligands are of potential interest in catalysis and various applications, and their extent of donation/back-donation has therefore been under extensive discussion.[75] Bridging boron ligands have been rarely studied, and therefore their bonding is of current interest. The charges in Table 7.4 suggest that a) the significant thermochemical stability of bridged borylene complexes[13] may derive partly from electrostatic contributions (cf. fragment charges of **9** and **10**), and b) the appreciably positive charge at boron explains the accessibility towards nucleophilic attack at the bridging ligand.[12, 76-78]

Turning to the dependence on the functional (Table 7.4), we see *more* charge transfer from the bridge to the metal fragments for the boron complexes **9** and **10** with increasing exact-exchange admixture from BLYP to B3LYP to BHLYP (with the exception of the BHLYP result for **10**, which is lower, for as yet unknown reasons). That is, the enhanced „localization“ of charge with exact-exchange admixture works from the bridge to the metal. The situation is reversed for the carbon-bridged complexes **11** and **12**, where the net charge transfer *to* the bridge increases with increasing exact exchange. All four systems have thus in common that the overall charge transfer is enhanced with exact-exchange admixture, but the direction differs between boron and carbon ligands.

The experimentally obtained QTAIM charges for **9**[9] indicate even more charge transfer from the bridging ligand to the manganese centers (cf. footnote b in Table 7.4). This larger bond polarity is well in line with previous comparisons between QTAIM and NPA charges.[20]

7.4 ELF Analysis

The electron localization function (ELF[18, 19]) provides an alternative real-space function for the analysis of non-trivial bonding situations. While the ELF exhibits certain similarities to the negative of $\nabla^2\rho$ in terms of topological analysis,[79] it differs from the latter in a number of points, e.g. in the precise position of the attractors or in the number of attractors for covalent bonds.[80] The ELF has an extensive history of application to transition metal systems (see, e.g., reviews in refs. [19, 81]), including questions of metal-metal bonding in polynuclear carbonyl and related clusters.[34, 82-87] For example, the ELF

shows no direct M–M bonding attractors for the tris-carbonyl-bridged Fe–Fe interaction in $Fe_2(CO)_9$[34] or for the bridged edge in the C_{2v} isomer of $Fe_3(CO)_{12}$,[87] in both cases yielding conclusions consistent with the QTAIM results (as another example, no direct Rh–Rh-bonding attractors are found on the carbonyl-bridged faces of $Rh_6(CO)_{16}$[34]). The topological discussion of the ELF is typically based on the synaptic order of its attractors and the associated basins,[88, 89] where monosynaptic valence attractors are assigned to lone pairs, disynaptic attractors to 2-center bonds, and attractors of higher synapticity to delocalized multicenter bonding.

Consistent with the QTAIM results above, none of the bridged complexes **9** to **12** exhibits a direct Mn–Mn bonding attractor (cf. Figure 7.3), in contrast to the unsupported complex **13**, which exhibits a disynaptic bonding attractor at an ELF value of 0.42. The delocalized Mn–bridge–Mn bonding is apparent from the saddle-shaped areas of the ELF = 0.7 isosurfaces in Figure 7.3. Interestingly, further increase of the isosurface value reveals in some cases the separation into different attractors with associated basins in ELF, dependent again on the exchange-correlation functional.

Table 7.5. Number of trisynaptic (*disynaptic*) ELF attractors associated with the bridge-Mn bond; dependence on the functional.

Compound	BLYP	B11LYP	BHLYP
9	1 (*2*)	1 (*2*)	1 (*0*)
10	1 (*2*)	1 (*2*)	1 (*0*)
11	1 (*0*)	1 (*0*)	1 (*0*)
12	1 (*2*)	1 (*0*)	1 (*0*)

The trends in this case are closely consistent with the behavior of the VSCCs in the density, as discussed above: At BHLYP hybrid level with 50% HF exchange, only one trisynaptic attractor with ELF values near 0.82-0.88 is observed in all cases **9**-**12** (*cf.* Table 7.5). It points towards the Mn…Mn midpoint, as is the case for the corresponding VSCC. Consistent with the discussion for $-\nabla^2\rho$ (*cf.* Figures 7.1, 7.2), a decrease of exact-exchange admixture tends to diminish the high-ELF area in this trisynaptic domain and creates high-ELF attractors close to the connection line between manganese and the

bridging atom. While no further attractors are found for the methylene-bridged complex **11** at any level (Table 7.5), already at B3LYP level complex **10** develops two disynaptic attractors in addition to the central trisynaptic attractor. This is also the case for **9**, albeit in a less pronounced fashion (the two disynaptic attractors and their basins are clearly nonequivalent). In case of **12**, the B3LYP results exhibit only the trisynaptic attractor, whereas two disynaptic attractors appear additionally at BLYP level. This behavior is

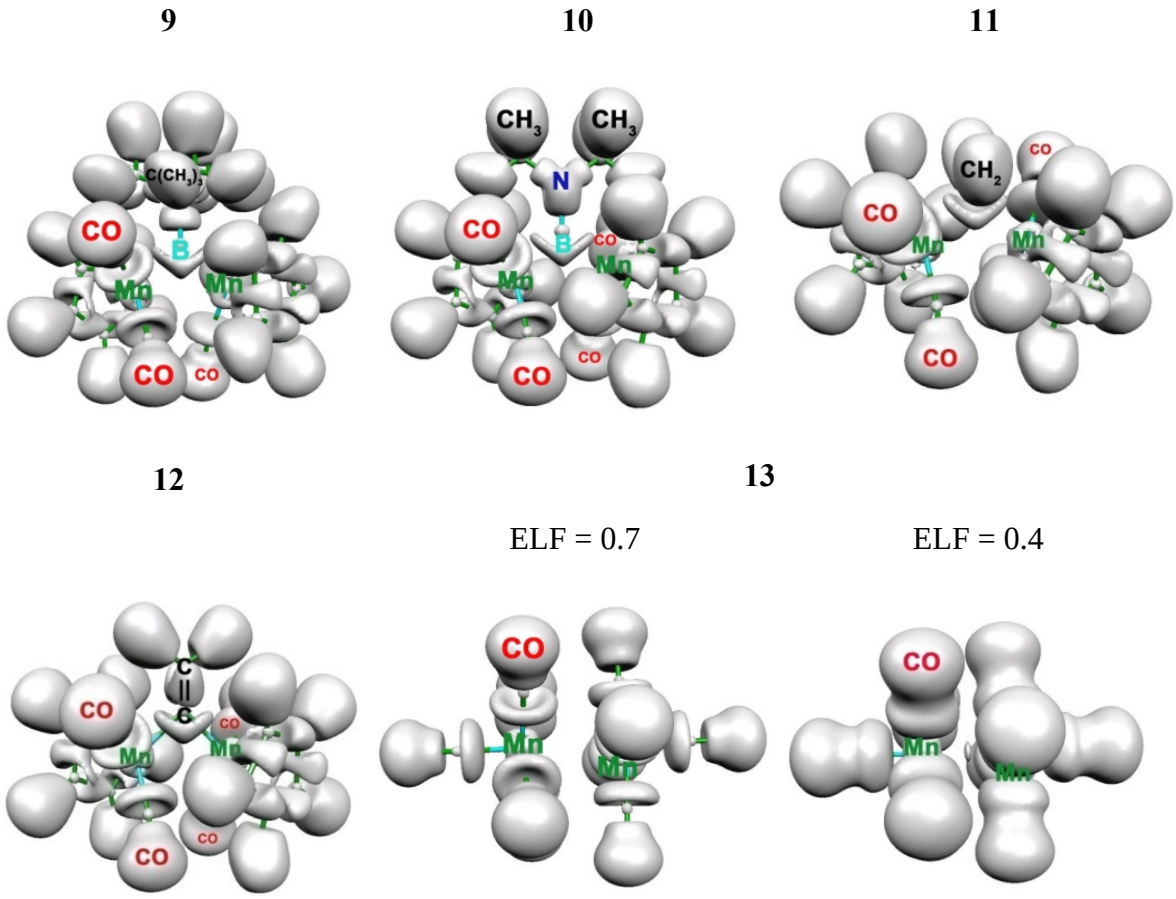

Figure 7.3. ELF isosurface plots; B3LYP/TZVP results; ELF = 0.7 isosurfaces, unless noted otherwise.

consistent with the pronounced bond covalency at GGA level and enhanced charge transfer to or from the bridge discussed above. The overall trends in $-\nabla^2\rho$ and ELF are thus very similar (wider areas of very negative $\nabla^2\rho$ and high positive ELF values at GGA *vs*. hybrid level). However, the development of disynaptic VSCCs in the density destroys the trisynaptic ones, whereas the trisynaptic ELF attractors survive even when the disynaptic ones appear. Again, we see close similarity but subtle differences between

these two quantities. As for the density, the di- and trisynaptic ELF basins at GGA (BLYP) level tend to be separated only little. To give just one example, the ELF values at the tri- and disynaptic attractors for **10** (BLYP data) are 0.815 and 0.830, respectively, whereas the separatrix (merging of the three domains) is at ELF = 0.806 (in contrast, the single trisynaptic attractor at BHLYP level is at ELF = 0.883). Thus we conclude that the ELF for these systems (except for **11**) is close to a bifurcation point between two different bonding topologies, just as observed for $-\nabla^2\rho$. This explains again the extreme sensitivity to the computational level, notably to the exchange-correlation functional.

The manganese valence regions are characterized by an approximately octahedral distribution of ELF attractors, similar to the arrangement of the VSCCs around the metal centers in the QTAIM analysis (*cf.* Figure 7.4 for a comparison).[80] As had been noted previously,[34] the non-bonding valence localization regions around coordinated metal centers tend to be arranged in the form of a dual polyhedron with respect to the ligand framework.

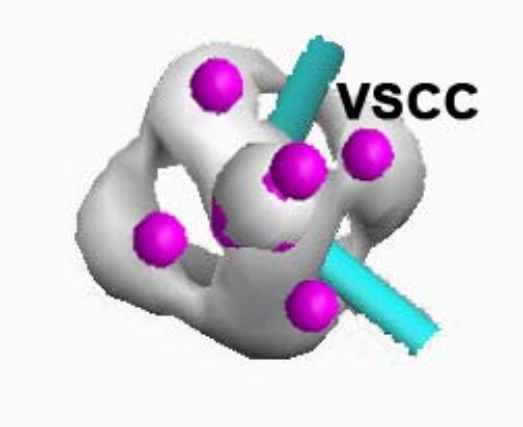

Figure 7.4. VSCCs in $-\nabla^2\rho$ (purple) mapped on ELF distribution (isosurface in grey with ELF = 0.73) around a manganese atom in **12**.

7.5 Conclusions

Both QTAIM and ELF analyses of the borylene-bridged complex **9** confirm the absence of significant direct Mn–Mn bonding, as had been suggested by the experimental charge density study. Indeed, in none of the systems studied here we find any QTAIM or ELF evidence for a direct Mn–Mn bond. This is most remarkable for the methylene complex **11** (and probably also for the vinylidene complex **12**), because this was often taken as *the*

prototype of a dimetallacyclopropane. All four bridging ligands in our title systems **9-12** may serve as good to excellent π-acceptors towards the $MnCp(CO)_2$ organometallic moieties. Charge transfer from metal-metal-bonding MOs into empty orbitals on the bridge provides a mechanism for preventing the direct Mn–Mn bond. The two residues are thus held together mainly by delocalized bonding across the bridging ligand, consistent with previous analyses for carbonyl complexes (see, e.g. ref. [11] and papers cited therein). The consistency between the descriptions by QTAIM and ELF is remarkable, because the ELF has a different connection to electron pairing and localization (and to the Pauli principle) than $-\nabla^2\rho$ and thus provides a complementary independent approach (Chapter 2).

Unexpected behavior has been found for the synapticity of the VSCCs and of the ELF attractors for the bridge in **9-12**. The methylene complex **11** exhibits the most clear-cut situation. A Mn–C–Mn three-center bonding picture is obtained at all computational levels, with only one VSCC or ELF basin associated with the bridgehead. We have found a striking qualitative dependence on the exchange-correlation functional in DFT calculations for the remaining bridged complexes **9**, **10**, and **12**: Depending on the exact-exchange admixture in the functional, the two boron bridges in **9** and **10** and the vinylidene bridge in **12** may involve delocalized three-center bonding across the bridge (as indicated by only one VSCC or by one trisynaptic ELF attractor) or separate into two two-center bonds (two VSCCs or overall three ELF attractors). GGA-type functionals like BP86 and BLYP favor a separation, whereas exact-exchange admixture in hybrid functionals like B3LYP or BHLYP shifts matters increasingly into a three-center bonding situation by accumulating charge in the area between the bridging atom and the Mn…..Mn midpoint. Thus, for **9**, BP86 or BLYP calculations agree qualitatively with the recent experimental charge density study by exhibiting two separated VSCCs (as well as two disynaptic and one trisynaptic ELF basins). In contrast, hybrid functionals collapse these basins (one VSCC in $-\nabla^2\rho$, one trisynaptic ELF basin). In these complexes, we are close to bifurcation points in both $-\nabla^2\rho$ and ELF, and slightly altered charge transfer from or to the bridge may switch matters from one to the other bonding situation. We should note, however, that the separation between the two VSCCs in **9** even at GGA-level is much less pronounced than found by the experimental charge density analysis. Of course we cannot disregard the role of the multipole expansion in the experimental

determinations. Further work on comparable nontrivial bonding situations should be rewarding, both by experimental electron density studies and by computations.

Comparing finally the boron- and carbon-bridged complexes in this study, the main difference is the net charge transfer *from the bridge* to the two Mn atoms in the borylene complexes **9** and **10** compared to the net charge transfer *to the bridge* in the methylene and vinylidene bridged complexes **11** and **12**. This reflects the overall better donor and diminished acceptor capabilities of borylene compared to carbene ligands as bridging units in this context. A positive charge at boron explains furthermore the accessibility to attack by nucleophiles at the bridging atom.

Chapter 8

Structure and Bonding in Supported Dinuclear Cobalt and Nickel Borylene Complexes

In the previous chapters, the question of direct metal–metal bonding as well as the numerous similarities between carbon ligands such as vinylidene or Fischer-/Schrock-type carbenes and the class of borylenes have already been discussed. Particularly, the comparison between carbenes and borylenes of identical spin state adduced the perception of differing bonding motifs according to the electronic configuration of the ligating center and the close cognation of both species, carbenes and borylenes (Chapter 6). However, the study on dimanganese complexes in Chapter 7 pointed at the dependence of QTAIM and ELF results on the applied level of theory. In précis, topological techniques such as QTAIM or ELF may be convenient to obtain deeper

insight into the electronic structure of intriguing chemical compounds, but have to be handled with care to circumvent misleading or even invalid chemical interpretations.

In the following chapter, a combined experimental and computational study on a pair of novel homodinuclear borylene 3*d* complexes is presented, providing further insight in transition metal–boron interactions. Especially in view of the dominant influence of the transition metal nature on the M–B bonding pattern, the comparison between connatural manganese (**9** in Chapter 7), cobalt and nickel complexes seems to be a promising approach to gain better knowledge about the parameters fine-tuning the electronic structure. Hence, in analogy to subsequent studies, analyses of the topology of charge density,[1] the ELF,[2, 3] and atomic charges[4] are employed to evaluate the bonding situations around the bridging boron atom.

8.1 Computational Details

All single points calculations were performed at the B3LYP/TZVP[5-9] level of theory using the Turbomole package[10-12] (version 5.10), based on coordinates obtained from X-ray diffraction studies. The electronic structure analyses were performed at the density functional theory level. Initially, the gradient-corrected functional BP86,[13, 14] the B3LYP hybrid functional[5-8] and the BHLYP hybrid functional[15] were compared. As the basic topology of charge density and ELF did not depend on the functional, only B3LYP results are reported. Charge-density analyses used the AIM2000[16] program package. The ELF was analyzed with the TopMod program.[17, 18] Natural population analyses[4] were used to obtain partial atomic charges.

8.2 Experimental Background and Structure Determination

Since the following results were obtained as part of a collaboration with *Braunschweig et al.*, a short overview about the experimental background as well as the crystallographically determined structures shall be given (further details can be found in ref. [19] or [20]) For the synthesizes of the borylene bridged complexes $[\{(\eta^5\text{-}C_5H_4Me)Co\}_2\{\mu\text{-}(CO)\}_2\{\mu\text{-}BN(SiMe_3)_2\}]$, **14**, and $[\{(\eta^5\text{-}C_5H_5)Ni\}_2\{\mu\text{-}(CO)\}\{\mu\text{-}BN(SiMe_3)_2\}]$, **15**, a photochemical approach has been employed. Equimolar amounts of $[(OC)_5M{=}BN(SiMe_3)_2]$ (M = Cr, W) and $[(\eta^5\text{-}C_5H_4Me)Co(CO)_2]$ were photolyzed in

tetrahydrofurane (thf) to yield dark red crystals of **14**, which could be structurally determined (see Scheme 8.1 and Figure 8.1a). In analogy, [{(η^5-C_5H_5)Ni}$_2${μ-(CO)}{μ-BN(SiMe$_3$)$_2$}] (**15**) has been obtained from the terminal tungsten borylene complex W(CO)$_5$BN(SiMe$_3$) (see Scheme 8.2 and Figure 8.1b) and characterized by X-Ray diffraction.

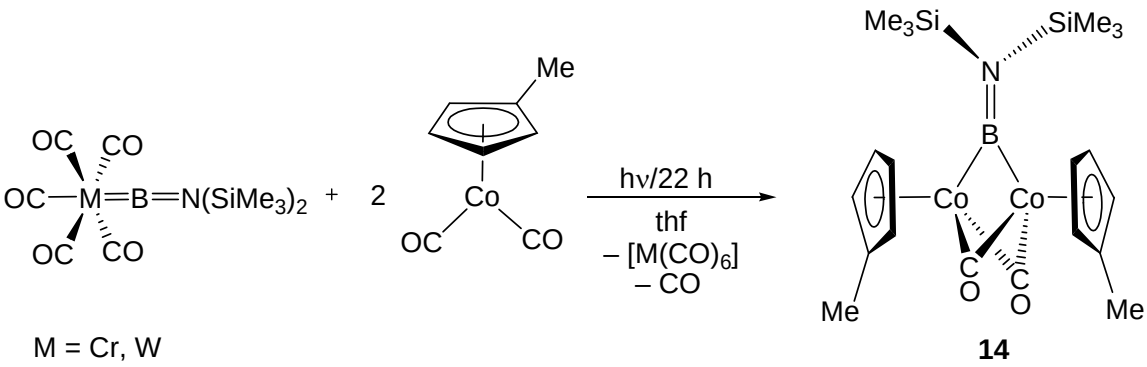

Scheme 8.1. Synthesis of the homodinuclear borylene complex [{(η^5-C_5H_4Me)Co}$_2${μ-(CO)}$_2${μ-BN(SiMe$_3$)$_2$}] (**14**) upon photolysis of [(OC)$_5$M=BN(SiMe$_3$)$_2$] (M = Cr, W) and [(η^5-C_5H_4Me)Co(CO)$_2$].

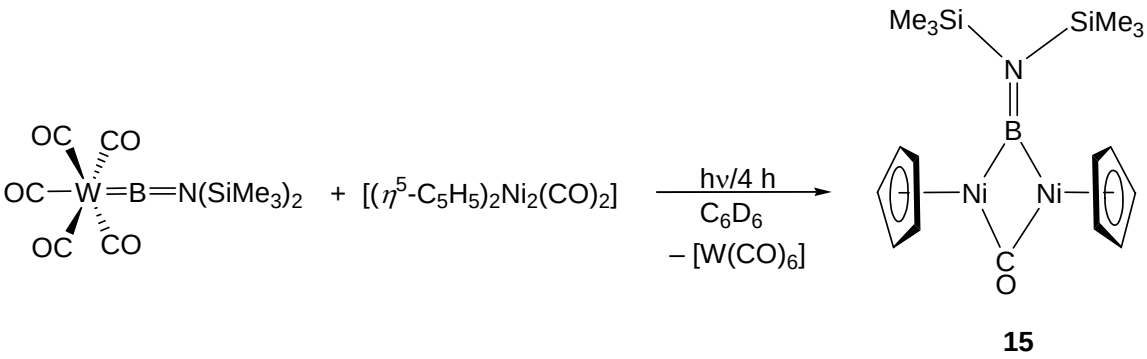

Scheme 8.2. Synthesis of the homodinuclear borylene complex [{(η^5-C_5H_5)Ni}$_2$-{μ-(CO)}{μ-BN(SiMe$_3$)$_2$}] (**15**) upon photolysis of[(OC)$_5$W=BN(SiMe$_3$)$_2$] and [(η^5-C_5H_5)$_2$Ni$_2$(CO)$_2$].

The molecular geometry of **14** closely resembles the structural arrangement of the bridged borylene complex [{(η^5-C_5H_5)Co(CO)}$_2${μ-BN(SiMe$_3$)$_2$}], **16**, with two terminal CO ligands.[21] As in **16**, the boron atom and both cobalt centers in **15** form an isosceles triangle with similar B−Co bond lengths of 1.983(2) Å [**16**: 1.952(2) Å], but with a considerably shorter Co−Co distance of 2.3489(4) Å [**16**: 2.493(5) Å] due to the bridging nature of the CO ligands (see also Chapter 2 for a detailed discussion of this effect).

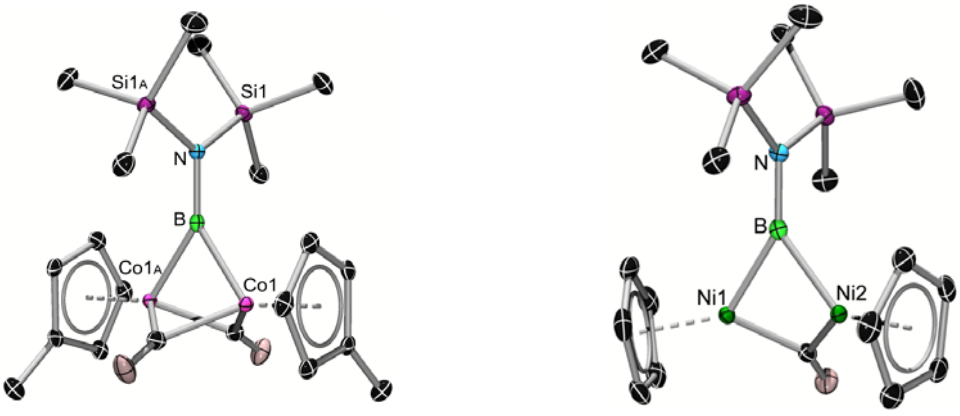

a **b**

Figure 8.1. a) Molecular structure of **14** in the solid state. Thermal ellipsoids are set at 50% probability. Hydrogen atoms are omitted for clarity. Bond length [Å] and angles [°]: B1−Co1 = B1−Co1A 1.983(2), Co1−Co1A 2.3489(4), Co1−C1 1.8665(16), Co1A−C1 1.9228(16), B1−N1 1.389(3); N1−B1−Co1−X_i 4, Co1−B1−N1−Si1 85. b) Molecular structure of **15** in the solid state. Thermal ellipsoids are set at 50% probability. Hydrogen atoms are omitted for clarity. Bond length [Å] and angles [°]: Ni1−Ni2 2.3414(2), Ni1−B1 1.921(14), Ni2−B1 1.937(14), B1−N1 1.384(17), N1−B1−Ni1−X_i 21, Ni1−B1−N1−Si1 88.[22]

The bridged bonding mode of the carbonyl ligands in **15** compared to **16** is presumably caused by the sterically more demanding (η^5-C_5H_4Me) rings and the resulting constrained geometry at the cobalt atoms. The cobalt−$carbon_{Carbonyl}$ bond lengths [Co1−C1: 1.8665(16) Å; Co1A−C1: 1.9228(16) Å], which are elongated in comparison to those in **16** [1.732(2) Å], are very similar to those observed in [(η^5-C_5Me_5)Co(μ-CO)]$_2$ [Co1−C1: 1.95(2) Å; Co2−C1: 1.99(2) Å][23] and are consistent with the bridging bonding mode of the carbonyl ligands (see also Chapter 5.2 for a detailed discussion on bond elongation upon terminal-to-bridged conversion). Due to the supporting nature of the CO ligands the centroids of the (η^5-C_5H_4Me) rings are nearly coplanar with the Co1-B1-Co1A plane (N1-B1-Co1-X_i: 4°). Compared to **16**, a shorter distance is found between the (η^5-C_5H_4Me) ring and the [$BN(SiMe_3)_2$] ligands, which results in an almost perpendicular arrangement (85°) of the Si1-N1-B1-Si1A plane with respect to the Co1-B1-Co1A plane (**16**: 54°). The B1−N1 bond [1.389(3) Å] is slightly shorter than in **16** [1.404(3) Å], indicating significant double bond character of the boron–nitrogen linkage.

Within the crystal structure of **15**, the {(η^5-C_5H_5)Ni} fragments are linked by a bridging borylene ligand [$BN(SiMe_3)_2$] and a single bridging CO group. The boron atom and both nickel atoms form an almost isosceles triangle, in which the Ni−Ni distance is 2.3414(2) Å and the Ni−B distances are 1.937(14) Å [Ni2−B1] and 1.921(14) Å [Ni1−B1]. Although the nickel–boron distances in **15** are slightly longer than that observed in other structurally characterized complexes,[24] these bond lengths are clearly within the range of borylene complexes containing a boron-3*d*-metal bond. The short B−N bond length [1.384(17) Å], together with the trigonal-planar geometry of the nitrogen atom, indicates the presence of a B=N double bond.

8.3 Bonding Analysis

In view of the subsequently presented studies on borylene supported dinulcelar complexes (see Chapter 7 and ref. [25, 26]), no direct metal–metal bond was anticipated for **14** and **15**. To put this on a firm basis, comparative analysis of bonding for **14**, **15**, and the diemanganese complex [(η^5-C_5H_5)$(CO)_2$Mn]$_2$BN$(CH_3)_2$, **10**, has been carried out, focusing on the charge density (using topological analyses of the Laplacian), natural charges, and the ELF. Apart from the question of direct metal−metal bonding, the nature of the bridge (i.e. delocalized three-center borylene *vs.* dimetalla-substituted borane) is of central interest.

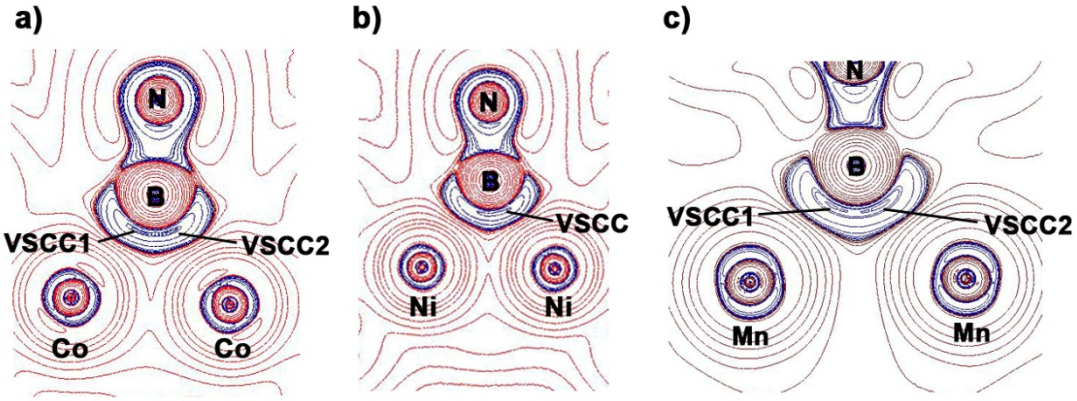

Figure 8.2. Comparative contour plots of $\nabla^2\rho$ for a) **14**, b) **15**, and c) **16**. Charge accumulations ($\nabla^2\rho < 0$) are blue, charge depletions ($\nabla^2\rho > 0$) red.

In agreement with subsequently described results, the present calculations generally indicate the absence of a direct M−M bond path in all borylene complexes studied. This is consistent with a dominance of bonding *via* the bridging ligands. Plots of the density Laplacian, $\nabla^2\rho$, in Figure 8.2 confirm this picture and indicate intriguing differences between the complexes concerning the number of VSCCs around the bridging boron atom: while the Mn and Co systems have two VSCCs pointing towards the metal centers plus one pointing towards the nitrogen substituent, the Ni system has only one "bridge-bonding" VSCC pointing towards the midpoint of the Ni−Ni connection line. Interestingly, these B3LYP results do not change with the functional, in spite of a relatively weak separation of the two VSCCs for **14** and **10**, in contrast to the results in Chapter 7. Hence, in the present analyses no bifurcation situation is observed with respect

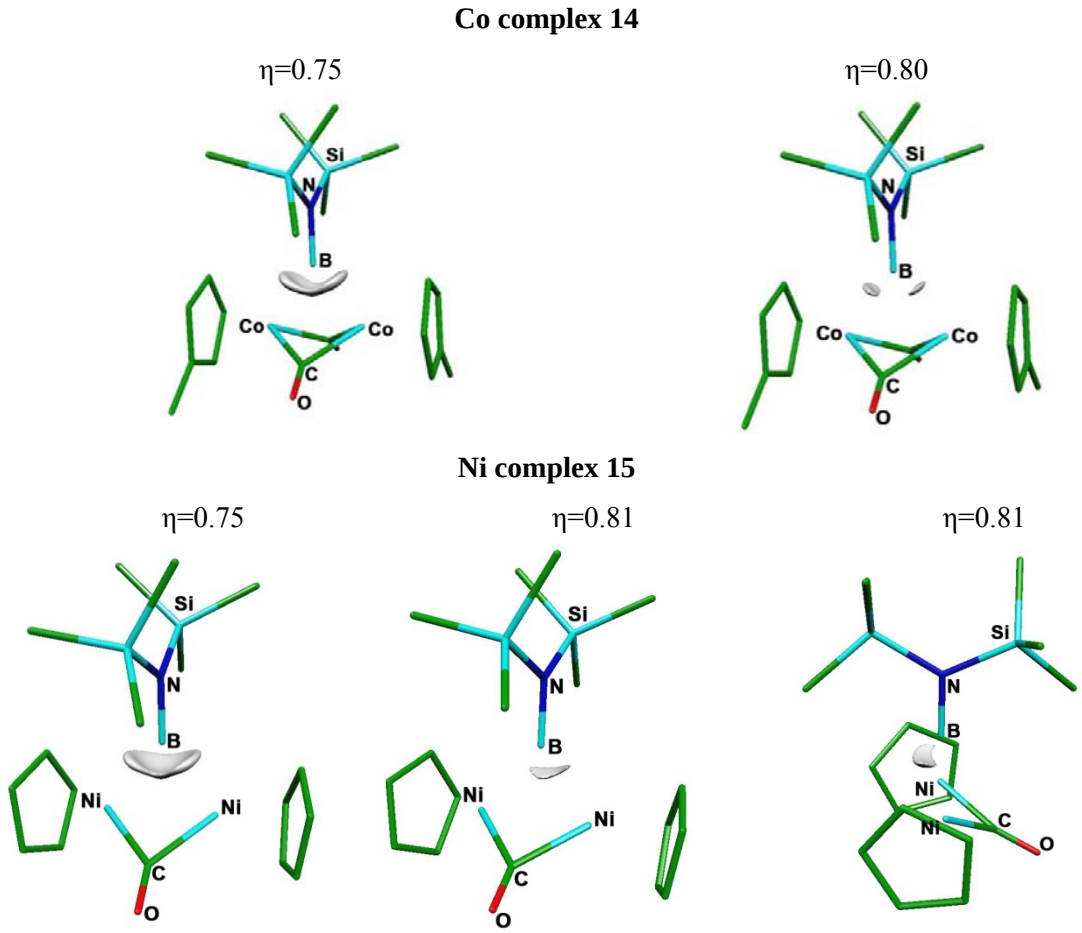

Figure 8.3. ELF isosurfaces (isosurface values given in each case) corresponding to the bridging M–B–M interactions (all other parts edited away) in **14** and **15** (with different views for **15**).

to the functional. This gives the differences between **14** and **15** appreciable significance: while the cobalt system **14** may be interpreted as a dimetallated borane, the Ni complex **15** is better represented as having a delocalized bridging borylene. As discussed in chapter 3, the reasons for these discrepancies may be rooted in the preferred spin state of the bridging ligand, taking into account the varying nature of the transition metal centers. According to the extended Fischer/Schrock concept introduced above, the borylene in **14** and **16** favors the formation of two actual electron pair bonds (as does vinylidene) due to a triplet configuration at the boron center. In contradiction, the boron atom in **15** features a singlet-type bonding pattern comparable to carbonyl ligands.

Table 8.1. BCP properties of selected bonds.

14	$\rho(\mathbf{r}_{BCP})$ [eÅ^{-3}]	$\nabla^2\rho(\mathbf{r}_{BCP})$ [eÅ^{-5}]
Co−B	0.7250	0.2884
	0.7251	0.2881
Co−CO[a]	0.8846	6.2247
	0.7896	5.0671
B−N[b]	1.4545	12.8417
15		
Ni−B	0.7535	0.7197
	0.7287	0.7644
Ni−CO[a]	0.9131	6.2144
	0.8921	5.9330
B−N[b]	1.4699	13.3564
10		
Mn−B	0.6593	0.1123
	0.6606	0.1433
Mn−CO[c]	1.0753	15.1323
	1.0025	13.8345
B−N[d]	1.4230	15.0272

[a]Bridging CO. [b][$BN(SiMe_3)_2$] ligand. [c]Terminal CO. [d][$BNMe_2$] ligand.

Consistent with the analysis of charge density, the ELF does not exhibit any basins that could be associated with a direct metal−metal bond. The ELF attractors corresponding to metal−boron interactions correlate closely with the number of VSCCs found in the Laplacian distributions. For **16** we find three valence basins, two pointing towards the respective manganese centers and one towards the midpoint of the Mn−Mn connection line. The latter is missing for **14**, which exhibits only the localized two-center attractors between boron and cobalt, consistent with a dimetalla-substituted borane. In contrast, **15** feature only the single central basin, consistent with the density Laplacian (*vide supra*). However, in contradiction to the latter, the attractor and its associated basin are pivoted away from the metal–boron–metal plane (see Figure 5.3). This may reflect the effects of Pauli repulsion with the orbitals of the single bridging carbonyl ligand. The fact that $\nabla^2\rho$ does not exhibit this off-center shift is interesting and may be an indication that the ELF displays Pauli repulsion in a more clear-cut way than the density Laplacian.

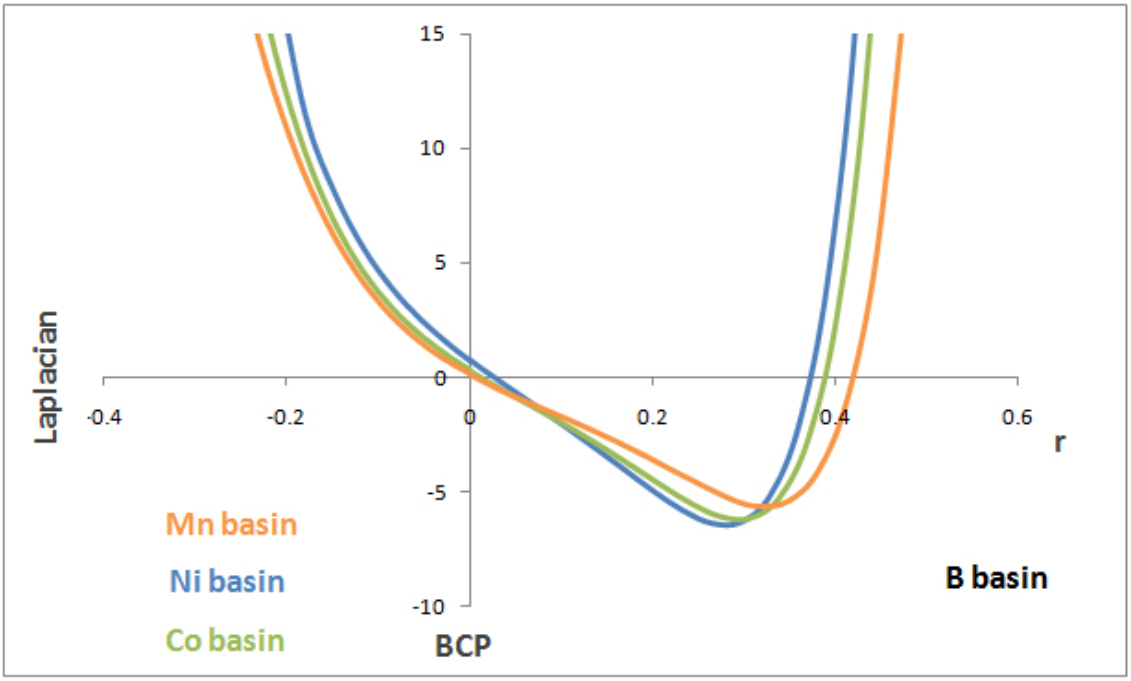

Figure 8.4. Plot of $\nabla^2\rho$ (in $e\text{Å}^{-5}$; distances in Å) in **10**, **14**, and **15** along the B−M bond path. The vertical axis marks the bond critical point.

The behavior of $\nabla^2\rho$ along the M−B bond paths (Figure 8.4) is highly likewise for all three complexes. However, the Ni complex exhibits steeper increases towards both the M and B basins. As a consequence, the value at the BCP in **15** is notably more

positive than for the other two complexes (Table 8.1). Given the rather sensitive dependence of the BCP properties on the position along the bond path (Figure 8.4), it would probably be an overinterpretation to rationalize this as a significantly more ionic bond for the Ni system. We note in passing the relatively similar BCP properties for the bridging CO ligands in **14** and **15** (these differ from the results for the terminal CO ligands in **16**).

Table 8.2. NPA charges for atoms and fragments.

Atom/Fragment	Co complex **14**	Ni complex **15**	Mn complex **10**
M	0.18962	0.56457	-0.44510
	0.18892	0.56259	-0.42781
Cp/MeCpa	–0.26184	–0.46396	0.05632
	–0.26197	–0.47309	0.05523
COb	–0.08262	–0.21723	0.11650
	–0.08257		0.12148
			0.12669
			0.10607
BNR2	0.31047	0.02715	0.10302

[a]Cp for the Ni and Mn complexes, Cp' for the Co complex. [b]Bridging CO ligand(s) for the Ni and Co systems, terminal CO ligands for the Mn complex.

As can be seen in previous studies (see e.g. Chapter 7), charge transfer between metal centers and the borylene bridge has been identified as important for the topology of $\nabla^2\rho$ around the bridging atom. Table 8.2 reports NPA charges for metal centers and ligands. The most notable features that distinguish the Ni complex from the other two systems are the rather pronounced positive charge of the metal center and the very small positive charge of the bridging borylene ligand. This suggests that the pronounced charge transfer from the bridging borylene to the metal centers previously observed for **10** holds also for the dicobalt complex **14** but not for the dinickel complex **15**. As a consequence of a larger charge accumulation near the bridging ligand in **15**, one VSCC with a large negative value of $\nabla^2\rho$ ($-6.709\ e\text{Å}^{-5}$ at the B3LYP level) is created rather than two VSCCs with less negative values as **15** ($2x\ -6.233\ e\text{Å}^{-5}$ at the B3LYP level), or **10** (-5.769 and $-5.788\ e\text{Å}^{-5}$ at the B3LYP level).[11] The relatively small charge transfer

from the bridging borylene ligand to the Ni centers in **15** reflects the poorer acceptor character of this late 3*d* metal, due to compactness and partially core-like character of the *d*-orbitals. Some backbonding contribution from the Ni atoms to the bridging carbonyl ligand is apparent from the negative NPA charge on that ligand, and the overall positive charges on the Ni−Cp fragments. In contrast, the Co−Cp' moieties in **14** bear slightly negative charges, and the bridging CO ligands are somewhat less negatively charged. Finally, the manganese complex **10** features very negative Mn−Cp fragments but appreciably positive terminal CO ligands (and pronounced charge transfer from the bridging borylene to the metal centers).[26]

One may expect a correlation of the B−N distances with the orientation of the bridging borylene ligand. Yet, no clearcut correspondence is observed, and the variations may be considered minor for **14** and **15**. Bonding analyses indicate a subtle interplay of in-plane and out-of-plane π-backbonding from metal *d*-orbitals to the bridging borylene fragment. While the orientation differs, in all three complexes components in the plane of the BNR_2 fragment and perpendicular to it may be identified. The former are generally distributed over a larger number of molecular orbitals than the latter. It appears that, in spite of some backbonding into B−N π* orbitals, the multiple-bonding character persists for any of the observed orientations.

8.4 Conclusions

We have reported the synthesis and structural characterization of the first homodinuclear borylene complexes featuring CO ligands in an unusual, symmetrically bridging position. Complex **15** represents furthermore the first nickel borylene species.

Quantum chemical analyses indicate the absence of direct metal–metal bonding in the title systems. Interestingly, the topology of charge density around the bridging boron atom in the dinickel complex is consistent with a delocalized borylene bridge, whereas the dicobalt system and previously studied manganese analogues exhibit a bonding situation of a dimetalla-substituted borane. The nickel borylene complex features less charge transfer from the bridging boron ligand to the metal fragments than the cobalt or manganese complexes, consistent with a poor acceptor character of the late 3*d* metal Ni.

PART III

Main Group Metals: Li–C Bonding and Intermolecular Interactions in Methyllithium

Chapter 9

Introduction

Since their discovery and the development of appropriate techniques (*Schlenk* and *Holtz*)[1], organolithium (RLi) compounds are amongst the most important auxiliaries currently available in preparative chemistry. They have proven especially useful as highly reactive nucleophiles and strong bases and applied in a plethora of organometallic reactions including anionic polymerization to carbolithiations and asymmetric catalysis.[2] A crucial step in all reactions including RLi is the addition of Lewis bases such as ether molecules or nitrogen bases yielding the huge class of base adducts, which are the actual educts in nearly all lithiumorganic reactions. Due to the strong relationship between structure and reactivity it is of fundamental importance to get insight into the structure forming principles of organolithium compounds and elucidate the changes occurring in the deaggregation process from the RLi oligomer to the base adduct. In the following section of this thesis (Part III) we will thus focus on both, isolated and donor-base

coordinated lithium organics and present a systematic study on structure formation principles and bonding features.

First, the basic structural motifs of the isolated organolithium species will be summarized to explain the requirement for specific computational tools (Chapter 9.1). Additionally, prevalent Li–C bonding concepts shall be surveyed as they are important to understand the underlying stereo-electronic patterns (Chapter 9.2). In the proceeding, quantum chemical methods are presented necessary for an appropriate description of extended systems (Chapter 10) and evaluated for the test cases of methyllithium (Chapter 11). To elucidate the electronic changes occurring on deaggregation, structures of methyllithium with coordinated donor bases like ether, TMEDA, TMCDA, (–)-sparteine etc. are examined in the following chapter (Chapter 12).

9.1 Aggregation of LiR – Structure Forming Principles

An important and ubiquitous feature in organolithium chemistry is the formation of aggregates and oligomeric structures with complicated three-dimensional distention. Generally, the structure of those is affected by three major factors:[2]

- Electrostatic interactions between the counter charges. Already in the seventies, *Streitwieser Jr.* proved that the correct structure of methyllithium could be obtained from a simple electrostatic model based on point charges (*Streitwieser-Bushby electrostatic model*).[3-5]

- The coordination sphere of the lithium atom. Commonly, lithium is commonly found in a coordination sphere of minimum three depending on the inclusion of solvent molecules or Lewis bases in the surroundings. Generally, it is assumed, that magnitude and type of coordinating neighbors influence the polarity of the Li–C bond and therefore the reactivity.[6]

- Extent and steric demand of the substituents at the lithiated carbon center. Besides bulky substituents influencing the stereochemical arrangement, the mere existence of a C_β atom allows alternative interactions in terms of agostic interactions or negative hyperconjugation as will be discussed later on.

For the donor base-free species, the Li_3 triangle μ_3-capped by a carbanionic C_α atom recurs as one of the most efficient structure forming principles. Based on this motif polyhedra are constructed, mostly containing a Li_4 tetrahedron or an octahedral Li_6 cluster.[6, 7] However, more exotic structures like the polymeric sandwich compound $[CpLi]_\infty$ or the π-stacked dimers $[PhLi]_\infty$ have also been observed.[8, 9] Overall, lithium organics come up with a surprising structural diversity that can be further extended including donor bases.

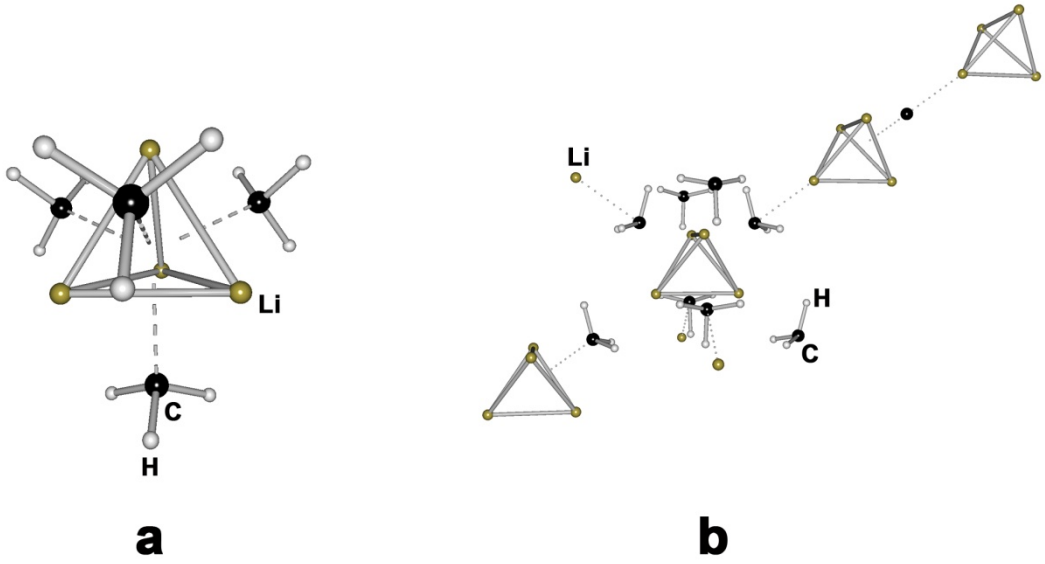

Figure 9.1. Tetrameric (a) and simplified polymeric (b) structure of methyllithium.

The simplest organolithium species is methyllithium, consisting of tetrameric $[MeLi]_4$ units linked to each other *via* long-range Li_3–C···Li interactions creating a three-dimensional network in solid state (Figure 9.1).[10] Due to this polymeric structure, methyllithium is insoluble in non-donating solvents like pentane and hexane and reactions are only possible, if the $[MeLi]_{4,\infty}$ network is prized open by donors. The intermolecular interactions between the $[MeLi]_4$ tetramers are known to be significant, to the extent that the preferred conformation of the methyl ligands differs between the crystal and the isolated (gas-phase) tetramer.[11, 12]

Besides MeLi, *tert*-butyllithium[13] and ethyllithium[14] are known to form tetrameric units. However, none of them exhibits the polymeric structure of the methanide species. Due to the presence of a C_β atom in ^{t}BuLi and EtLi, secondary Li···C_β interactions occur, rendering extended polymerization unnecessary and resulting in an ecliptical arrangement and shortened Li–C_β distances. Additionally it is assumed, that the shortened Li···Li distances observed when going from methyl *via* ethyl to *tert*-butyl are

caused by the increasing charge releasing capability of the carbanions along this line.[6] In the extreme case, the *t*butyl group provides so much electron density to the carbanionic center, that the electrostatic repulsion between the single lithium atoms is decreased and so are the distances between them. However, this concept has to be surveyed by means of charge and population analyses.

In all structurally determined binary hexamers, $[^{n}BuLi]_6$,[13] $[^{i}PrLi]_6$,[15] $[^{c}PenLi]_6$[13] etc. two of the eight present Li_3 triangles are not C_α-capped and arranged opposite of each other. Nevertheless, both tetrahedral and octahedral organolithium compounds are highly compact with a minimum of four coordination partners and show surprisingly little chemical reactivity compared to their donor-base coordinated equivalents. This refers already to the strong relationship between reactivity and structure that dominates organolithium chemistry.[16, 17] It is common knowledge, that the lowering of the aggregation degree by means of Lewis base addition is accompanied by an increase of reactivity.[2, 7] Generally, it is assumed that monomers are the reactive species, thus the organolithium compound first dissociates to monomers before it enters the reaction cycle.[18] However, dimer-based and further alternative reaction mechanisms have also been proofed.[19-23] Beyond the structural changes occurring during the deaggregation process, the modification in the electronic structure of the Li–C entities is yet an open question. One of the widely held notions is that the bond polarity within the monomeric species is increased compared to the higher aggregates,[24, 25] which causes the reactivity enhancement. However, DFT studies on isolated RLi clusters of lower aggregation state showed little changes or even opposite trends in the natural charges.[12, 16]

9.2 Prevalent Bonding Concepts in Organolithium Compounds

Most generally, lithium organics feature sigma 2-center-2-electron and 4-center-2-electron bonds in the Li_3C_α entities, but also 3-center-2-electron interactions have been commonly observed. Thereby, direct Li···Li bonds have always been out of question and only discussed in terms of delocalized interactions within metal clusters.[26] The amount of covalent contribution in the Li–C bond, however, is an issue of constant debate, bouncing between predominantly ionic and significantly covalent. The solubility of some lithiumorganics in nonpolar solvents like benzene (which is in contrast to the behavior of

other alkali-alkyls), high NMR Li–C coupling constants as well as the importance of orbital interactions have been indication for an essential covalent interaction which stands in contradiction to the high electronegativity difference.[27-29] Conversely, the *Streitwieser-Bushby electrostatic model*, QTAIM and population analysis confirm a highly ionic interpretation of the Li–C bond.[3-5, 25, 30] Indubitably, one can simply conclude with the statement of the Li–C bond being significantly polarized, while the precise amount of ionic and covalent contribution decisively depends on the individual case and the applied analysis method. However, tendencies in the Li–C polarity changes due to deaggregation and Lewis base coordination shall be surveyed in detail later on (Chapter 13).

Besides the direct Li–C_α bonding, lithium organics feature in many cases secondary interactions which have broadly been termed as agostic (from Greece "to hold closely to oneself").[31-33] From a Cambridge Structural Database study it becomes quite obvious that shortened Li···H–C (1.98-2.20 Å) contacts are very common in lithiumorganics giving rise to the assumption of stabilizing Li···H–C interactions.[34] However, an exact experimental investigation of these structural patterns is challenging and only possible *via* neutron diffraction, since hydrogens can hardly be determined within X-ray data due to their single electron being involved in bonding. Alternatively, NMR studies have been undertaken, since agostic interactions can be detected by an upfield shift or lowered coupling constants in the ^{1}H-NMR. Nevertheless, it is far more complicated to extract exact structural data from the NMR parameters.[35] Furthermore, the conformational divergence between the polymeric solid state and tetrameric gas phase structure of methyllithium supports the idea of additional Li···H–C interactions. However, the energy of those agostic interactions is very small and has been determined to 4.19 kJ/mol per C–H bond for the case of MeLi.[16] Consequently, it is of high dubiety to interpret these fine details in terms of chemical significance.

Related to agostic interactions, close Li···C_β contacts have been assigned to electron delocalization comparable to negative hyperconjugation or generalized anomeric effects.[36, 37] Prominent examples are the *n*-butyllithium hexamer (*n*-BuLi)$_6$ and tetrameric *tert*-butyllithium (*t*-BuLi)$_4$. In principle, negative hyperconjugation describes electron delocalization from lone pairs (e.g. of the carbanionic center) or $\pi \rightarrow \sigma^*$ molecular orbitals (Figure 9.2), stabilizing an eclipsed conformation. In contrast, the concept of (normal) hyperconjugation ($\sigma \rightarrow \pi^*$) has been employed to explain the

favored staggered arrangement of most organic molecules.[38-40] From the experimentalist's point of view, the concept of negative hyperconjugation has been successfully applied in terms of stabilizing the carbanionic center by the introduction of second row substituents in α-position. This stabilization effect becomes quite obvious in chemistry and structure of silyllithium compounds.[2, 41] Although the structural consequences assigned to hyperconjugation are quite obvious in many cases, the quantification of its influence on the total electron distribution is rather challenging. It has been attempted by orbital analysis as well as QTAIM.[42] Based on experimental (X-ray and neutron diffraction) as well as theoretical data, the charge delocalization due to hyperconjugation could be tracked by ellipticity profiles along the individual bond paths. However, the secondary interactions responsible for the preference of the *cis*-conformation could only be discussed in a very coarse way.

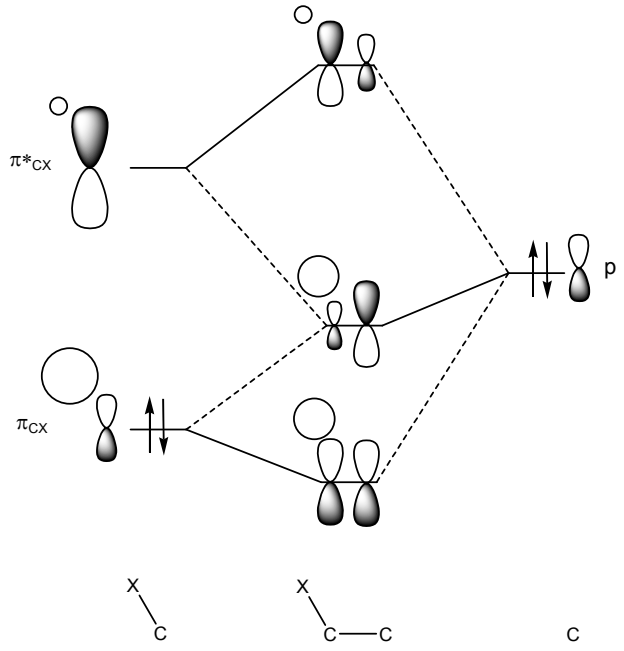

Figure 9.2. Negative hyperconjugation scheme according to Schleyer et al.[36]

In view of the tendency for aggregation and the complicated bonding patterns including many weak, nevertheless significant interactions, the handling of lithium organics with standard gas-phase DFT methods is problematic. Already from the example of methyllithium with its different conformations within gas-phase and solid state, it is obvious, that intermolecular interactions have to be taken into account. Therefore, explicit solid state calculations are necessary to evaluate the environmental influence.

Chapter 10

Computational Methods

Molecular quantum mechanics and the computation of solid state materials have been surprisingly independent research fields for many years. Even with the poor technical supplement of the 70s, molecular simulations and the prediction of system properties were already possible while solid state simulations were still very difficult and unfeasible in many cases due to the enormous complexity of even the simplest crystals or metals. Consequently, both research areas developed completely different approaches to solve the Schroedinger equation. While molecular quantum mechanics started off with HF techniques and are based on the hydrogen atom or molecule, the origin of solid state simulations lies in the description of the free electron gas and DFT methods. Although nowadays DFT approaches are also applied for molecular problems, one is faced to many particularities within the simulation of periodic systems. On the next pages a short introduction on the calculation of crystals and their efficient approximation *via* embedding schemes shall be given.

10.1 Periodic Simulations

Today solid state simulations are possible with a variety of programs (e.g. WIEN2K[1], VASP[2], CRYSTAL06[3]), following different strategies and models. In principle their differences can be summarized in the following issues.[4]

- *The model*. According to the physical and chemical phenomena that shall be investigated, the program comprises different models describing particular model systems. A good example for this is the description of defects. Either the defect is modeled *via* a supercell and repeated periodically, which might cause interaction potentials. Alternatively, the defect is located in the middle of a cluster which can cause surface effects. Both effects are expected to be negligible if the approximation is applied within its limits.
- *The Hamiltonian*. Most of the solid state programs are DFT-based. However, the research for alternative approaches is still going on due to the shortcomings of suitable functionals. For example, the CRYSTAL team implemented a perturbational method in their program packages opening the possibility for post-HF methods in solid state.[5, 6]
- *The basis set*. Many solid state programs employ plane wave approaches, which is quite natural for infinitely periodic problems. However, it makes actual comparison with molecular simulations difficult. Alternatively, Gaussian, numerical or other basis sets can be applied.
- *The overall computational scheme*. As within gas-phase programs there is an infinite leeway of how precisely implementing the different tools and their computational realization.

Since the CRYSTAL06 program was used for all solid state calculations in this work, we will predominantly concentrate on its formalism. Additionally, we will focus on the simulation of crystals in the proceeding and leave out the description of defects or slabs.

10.1.1 Basic Formalism

As with any (non-relativistic) quantum mechanical problem, the answer lies in the solution of the Schroedinger equation. However, due to the periodicity of the solid state

system (which is approximated to be infinite), the eigenvectors of the Schroedinger equation have to be translational invariant and incorporate the recurring patterns of the crystal. Hence, one has to think about a suitable wavefunction first. Schematically, this wavefunction should consist of two parts (s. Figure 10.1).[7]

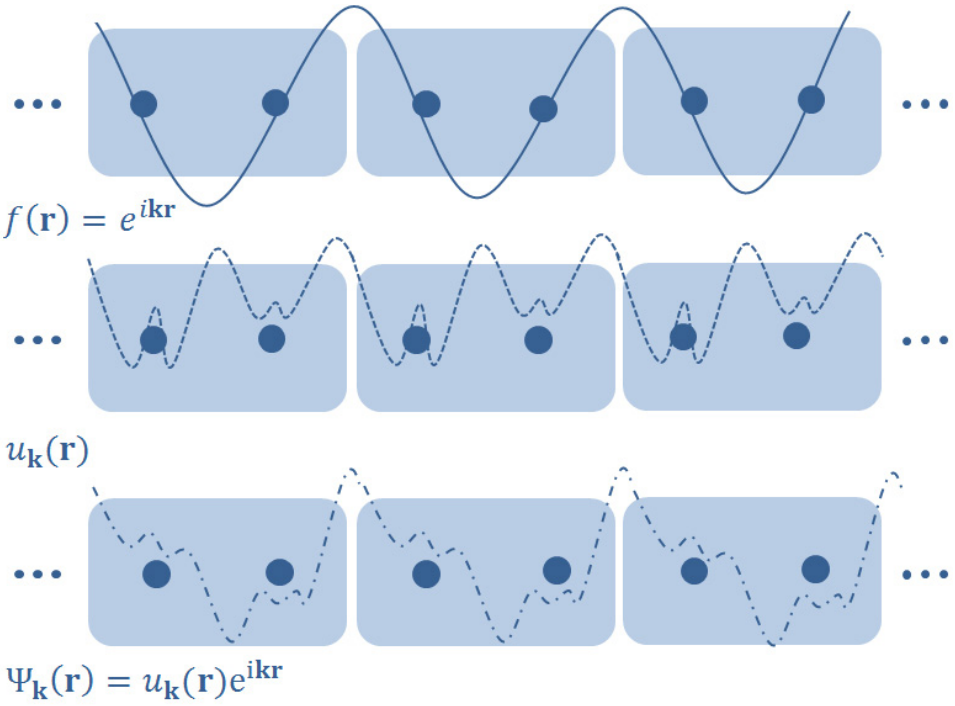

Figure 10.1. Construction of a Bloch function.

The Bloch wave is a simple plane wave of the form $f(\mathbf{r}) = e^{i\mathbf{kr}}$ and $\mathbf{k}$ being the wave vector. It preserves the infinite periodicity of the system. Additionally, one needs a function $u_{\mathbf{k}}(\mathbf{r})$, which represents the periodicity of the lattice and the atoms therein. It can be expanded in any basis set.

The superposition of these two components results in the *Bloch function*, which is the modulation of a plane wave by the lattice periodic function $u_{\mathbf{k}}(\mathbf{r})$. Depending on the basis set expansion of $u_{\mathbf{k}}(\mathbf{r})$ the plane wave in the Bloch function expression can be skipped. To provide a suitable solution for solid state quantum mechanics, the Bloch function has to fulfill two conditions.

Periodic Boundary Condition

To preserve the infinite periodicity of the lattice, these boundary conditions are applied. If the unit cell is expanded by the direct lattice vectors $\mathbf{a_1}$, $\mathbf{a_2}$ and $\mathbf{a_3}$, the wavefunction should have the same value after every shift by $\mathbf{a_1}$, $\mathbf{a_2}$ and $\mathbf{a_3}$.

$$\Psi_{\mathbf{k}}(\mathbf{r} + n_i\mathbf{a}_i) = \Psi_{\mathbf{k}}(\mathbf{r}), \tag{10.1}$$

with i = 1, 2, 3 and n being any integer.

Bloch Theorem

The potential energy of a perfect, infinite crystal must be a periodic function with the same periodicity as the lattice. Hence, for a translation by any direct lattice vector $\mathbf{g}$,

$$\mathbf{g} = n_1\mathbf{a}_1 + n_2\mathbf{a}_2 + n_3\mathbf{a}_3, \tag{10.2}$$

the potential energy does not change. Due to these symmetry requirements, the Schroedinger equation must also be translation invariant

$$\widehat{H}(\mathbf{r} - \mathbf{g})\Psi(\mathbf{r} - \mathbf{g}) = E\Psi(\mathbf{r} - \mathbf{g}). \tag{10.3}$$

It has been proven[8] by *Bloch* that eigenfunctions with the correct symmetry with respect to the translation invariant potential must obey the *Bloch Theorem*

$$\Psi(\mathbf{r} + \mathbf{g}; \mathbf{k}) = e^{i\mathbf{k}\mathbf{g}}\Psi(\mathbf{r}; \mathbf{k}). \tag{10.4}$$

It provides a relation between the values of the wavefunction at two equivalent lattice points *via* the phase vector $e^{i\mathbf{k}\mathbf{g}}$. If both conditions are fulfilled, one obtains the Bloch-function as suitable wavefunction for periodic systems. Based on this eigenfunction, one can solve the Schroedinger equation with dependence on the wave vector $\mathbf{k}$, more precisely, $\mathbf{k}$ marks the different solutions of the Schroedinger equation. However, $\mathbf{k}$ is also a point in reciprocal space.

First of all, so-called reciprocal space is a geometric construction following orthogonality rules with respect to direct space. The basis vectors $\mathbf{b_1}$, $\mathbf{b_2}$ and $\mathbf{b_3}$ of the reciprocal lattice are connected to the direct space lattice vectors $\mathbf{a_1}$, $\mathbf{a_2}$ and $\mathbf{a_3}$ *via*:

$$\mathbf{a}_i \cdot \mathbf{b}_j = 2\pi\delta_{ij}. \tag{10.5}$$

This implies that every reciprocal lattice basis vector $\mathbf{b}_j$ is orthogonal to the plane expanded by the direct lattice vectors $\mathbf{a}_{i\neq j}$ of unequal indices. Therefore, every symmetry element contained in direct space is mirrored in the reciprocal lattice. As the most important one, the concept of the periodically repeated unit cells is also found in reciprocal space *via* the construction of the *first Brillouin zone*. It can be received by connecting one **k** point with all its nearest neighbors and letting orthogonal planes pass through the midpoints. As the description of the unit cell in direct space is sufficient for classifying all properties of the full crystal, the characterization of the first Brillouin zone contains all information of the reciprocal space. This bears the advantage that only **k**-point solutions of the Schroedinger equation in the first Brillouin zone have to be evaluated.

However, the reciprocal lattice can actually be observed as diffraction pattern recorded from X-Ray scattering from crystals. Hence, the reciprocal lattice is also a construction to describe the diffraction from periodic structures, which is a periodic function itself. A well-suited method to describe any periodic function is the Fourier series. It connects

- Time- and frequency-dependence (e.g. within spectroscopy) or
- Local and wave-vector dependence (e.g. direct and reciprocal space).

Within a Fourier expansion every periodic function $f(\mathbf{r})$ can be expressed as superposition of sinus and cosines waves with amplitudes A(**k**) and B(**k**), respectively.

$$\tilde{f}(\mathbf{r}) = \sum_{\mathbf{k}=0}^{\infty} A(\mathbf{k}) \cos(\boldsymbol{kr}) + B(\mathbf{k}) \sin(\mathbf{kr})\, d\mathbf{k} \tag{10.6}$$

Consequently, the infinite periodicity of the function $f(\mathbf{r})$ is implicit in the Fourier expression $\tilde{f}(\mathbf{r})$. Reciprocal space can therefore also be termed Fourier space. Actually, if one has obtained a diffraction pattern from a crystal it is anti-Fourier-transformed to obtain the local atomic distribution in direct space. For describing properties or interactions in periodic systems the Fourier transform has a lot of advantages (see e.g. ref. [9]). Many techniques for solving integrals in solids like the Ewald summation[10] are based on the Fourier transforms of the local wavefunction. Ewald's technique is an efficient method to handle the Coulomb interaction in a periodic system. Every electron

in a given unit cell does not only interact with the other electrons of the same cell, but also with the images of all electrons in the adjacent cells. Within Ewald's approach the Coulomb integral is separated in a short-range part (interaction with the nearest neighbors), solved in direct space and a long-range component (interaction with the images in adjacent cells) calculated in reciprocal space. Normally, the latter is truncated when the overlap integral has fallen below a certain threshold.

However, as direct space is infinitely periodic, so is reciprocal space. Hence, one can obtain an infinite amount of eigenvalues for the Schroedinger equation, each linked to a **k** point. Therefore, the Hamiltonian matrix is of infinite size and impossible to handle at this stage. Great advantage is taken, however, if the Hamiltonian is represented in the basis of Bloch functions. In fact, one obtains a block-diagonalized matrix, with each block referring to one **k** point, i.e. to one solution of the Schrödinger equation. Hence, the matrix is still infinite but contains finite, independent blocks, which can be treated separately. Since the eigenvalues change only slightly for different **k** points, one samples the first Brillouin zone and solves the Schroedinger equation for these points. If the sampling (e.g. *via* Pack-Monkhorst mesh) is opportune, this is a feasible job.

10.2.2 Gaussian Basis Sets in Solid State Calculations

If $\hat{\mathrm{H}}$ is the one-electron Hamiltonian within the Born-Oppenheimer approximation, the solutions of the Schroedinger equation are called crystalline orbitals (*CO*). They are expanded in the basis of one-electron Bloch functions $\phi_j(\mathbf{r}, \mathbf{k})$,

$$\psi_n^{CO}(\mathbf{r}, \mathbf{k}) = \sum_j c_{jn}(\mathbf{k})\phi_j(\mathbf{r}, \mathbf{k}), \tag{10.7}$$

with coefficients c_{jn} to be determined. Atomic orbitals as well as plane waves are common choices to represent the one-electron Bloch functions, but, atomic orbitals are closer to molecular quantum mechanics. However, the use of atomic orbitals for solid state systems puts some severe restrictions to the basis set composition. Numerical instabilities due to quasi-linear dependence problems enforce the use of relatively small basis sets with few, often unsatisfactory diffuse functions compared to molecular calculations.[11] Since CRYSTAL employs Gaussian type basis sets, we will concentrate on the latter in the proceeding.

As within gas-phase calculations the one-electron basis functions are expanded as a linear combination of atomic orbitals (LCAO approximation). Though, they have to be replicated for all neighboring molecules in the adjacent **g**-cells to form the periodic component of the Bloch function. If $\chi_\mu(\mathbf{r}_\mu)$ is the μ-th atomic orbital with its origin at $\mathbf{r}_\mu$ in the 0-cell, the corresponding replica is $\chi_\mu^{\mathbf{g}}(\mathbf{r}-\mathbf{r}_\mu)$ in the **g**-cell. Accordingly, the Bloch function is obtained as:

$$\phi_\mu(\mathbf{r},\mathbf{k}) = \frac{1}{\sqrt{N}}\sum_{\mathbf{g}} e^{i\mathbf{k}\mathbf{g}}\chi_\mu^{\mathbf{g}}(\mathbf{r}-\mathbf{r}_\mu), \tag{10.8}$$

with N normalizing the function. Following a scheme very similar to the HF procedure, the Fock matrix $\mathrm{F}_{\mu\nu}^{\mathbf{g}}$ is built in direct space

$$\mathrm{F}_{\mu\nu}^{\mathbf{g}} = \langle\chi_\mu|\hat{F}|\chi_\nu^{\mathbf{g}}\rangle. \tag{10.9}$$

Since one can always refer to $\chi_\mu(\mathbf{r}_\mu)$ as positioned in the 0-cell due to translation invariance, a new lattice vector **m** = **g** – **g'** is introduced and the Fock matrix. If $\mathrm{F}_{\mu\nu}$ is then expressed in the basis of Bloch functions, one obtains:

$$\mathrm{F}_{\mu\nu}(\mathbf{k}) = \sum_{\mathbf{m}} e^{i\mathbf{k}\mathbf{m}}\,\langle\chi_\mu^0|\hat{F}|\chi_\nu^{\mathbf{m}}\rangle. \tag{10.10}$$

This expression can be interpreted as the Fourier transform of the Fock matrix and is solved for different **k** points. For calculating the individual sums that contribute to the Fock matrix, the Ewald summation technique is applied. This can be combined with a series of truncation schemes, since the estimate of the importance of interparticle interaction is relatively simple in direct space. Two aspects shall be mentioned here as specific for solid state simulations: the calculation of matrices in direct space and the integration in reciprocal space.[4]

10.2 Embedding Techniques

There are many possibilities to bridge the gap between pure gas-phase and full solid state calculations. All of them aim at the efficient description of the environmental influence and intermolecular interactions. The demand for these methods is high since many

molecular crystals cannot be described by solid state approaches due to their lack of extended symmetry and the size of their unit cells. Additionally, for solid state simulations, the choice of employable methods is limited (normally DFT and HF, treatment of relativistic effects etc.) and basis sets are restricted as discussed on the preceding pages. The answer to this problem are embedding schemes, which separate the system into a core region which is treated quantum mechanically and "embed" it into surroundings that can be modeled by different approaches and on different levels of theory. On the following pages, two relatively "simple" embedding schemes will be presented a) polarizable continuum models (PCM)[12-15] and the recently proposed periodic electrostatic embedded cluster model (PEECM)[16].

10.2.1 The Polarizable Continuum Model

The Polarizable Continuum Models (PCM) are amongst the computationally least expensive approaches available. However, they do not account for the microscopic charge distributions and specific interactions. Their performance is nevertheless of great interest due to their easy use and conceptual simplicity. The basic idea within the PCM is to surround the QM-treated cluster by a polarizable continuum modeled by a field of point charges located on the QM cavity surface. The interaction potential of these point charges with the QM cluster can then be evaluated to model the interplay between both regions as it is done e.g. in COSMO.[13] Within COSMO the dielectric continuum is approximated by a scaled conductor, which simplifies the boundary conditions.[17] The basic concept of this approach is to use an infinitely strong dielectric (i.e. a conductor with $\varepsilon = \infty$) to reduce the "interaction width" so that the alteration of the dielectric by the QM cluster can be neglected. The interaction potential of an infinitely strong dielectric surrounding can be simplified to a pure surface effect which can be modeled by infinitesimally small charges on the QM cavity surface. For the simulation of finite dielectrics these charges can be scaled. The QM cavity and the surrounding dielectric are interlinked by a response function which handles the modulation of the surface charges by the charge density of the QM cluster and *vice versa*. Typically, this approach is used to model the influence of solvent shells on the charge density of a solute. However, one can easily adopt this technique to estimate the electrostatic potential of a "crystal solvent" on the QM area.

10.2.2 The Periodic Electrostatic Embedding Cluster Model

Originally, the PEECM was developed to describe defects in solids at a computationally cheap level and without the disadvantages of the existing possibilities by *Sierka et al.*[16] It is based on a cluster approach where the extended periodic system is divided into a local region, which is treated with QM, and the surroundings, which are described by an electrostatic potential based on point charges. Additionally, an intermediate region is created to isolate the shell surroundings from the innermost QM portion and prevent overly polarization or "leak out"[18] effects on the inner part. In this section the positive charge of the cations is "smeared" due to replacement by pseudopotentials (ECPs).

The electrostatic interactions between the QM section and the surroundings are taken into account by an additional term $\mathrm{F}_{\mu\nu}^{emb}$ in the Fock or Kohn-Sham matrix as well as an additional term J^{emb} in the total energy.

$$\begin{aligned} \mathrm{F}_{\mu\nu}^{emb} &= -\sum_{\mathbf{L}}^{lattice\ unit\ cell}\sum_{j} q_j \int \frac{\mu(\mathbf{r}-\mathbf{R}_\mu)\nu(\mathbf{r}-\mathbf{R}_\nu)\delta(\mathbf{r}'-\mathbf{R}_j+\mathbf{L})}{|\mathbf{r}-\mathbf{r}'|} d\mathbf{r}d\mathbf{r}' \\ &= \sum_{\mathbf{L}}^{lattice\ unit\ cell}\sum_{j} q_j\,(\mu\nu|\delta_{jL}) \end{aligned} \tag{10.11}$$

$$\mathrm{J}^{emb} = \sum_{\mu\nu}^{cluster} P_{\mu\nu}F_{\mu\nu}^{emb} + \sum_{\mathbf{L}}^{lattice\ unit\ cell}\sum_{j}\sum_{a}^{cluster} \frac{q_j Z_a}{|\mathbf{R}_a-\mathbf{R_j}+\mathbf{L}|}, \tag{10.12}$$

where $\mathbf{L}$ represents a lattice vector in direct space and j is the index of an ionic point charge q_j at position $\mathbf{R}_j + \mathbf{L}$ outside the QM cluster. Consequently, the summation over $\mathbf{L}$ and j includes all periodic images of this point charge except those which are positioned in the QM or ECP regions. Gaussian basis functions μ and ν at positions $\mathbf{R}_\mu$ and $\mathbf{R}_\nu$ and nuclear point charges Z_a with corresponding positions $\mathbf{R}_a$ belong to the cluster. The elements $P_{\mu\nu}$ of the density matrix are used together with the appropriate Fock matrix elements $F_{\mu\nu}^{emb}$ to calculate the Coulomb energy between the electron density of the QM part and the point-charge lattice.

For the calculation of the lattice sums in $\mathrm{F}_{\mu\nu}^{emb}$ and J^{emb} the *periodic fast multipole method* is employed.[19-21] It is based on a multipole expansion[22-24] and provides an effective and computationally cheap method to calculate the Madelung potential of the

crystal in the local QM region. In the first step the point charge region is divided into near-field and far-field sections (comparable to the Ewald summation). All electrostatic interactions between the QM part and the point charges of the near-field are calculated analytically. The remaining interactions with the far-field are simulated via the periodic fast multipole method.

It should be mentioned at this point that both methods, the PCM and the PEECM are only applied to clusters with no covalent interactions to the embedding part. Otherwise, one would be faced to the problem of “dangling bonds” as it is known from QM/MM (molecular mechanics) or QM/Pot (potential function) methods.[25, 26]

Chapter 11

Validation of Embedding Techniques for Modeling Environmental Effects in Polar Organometallics

In view of its character as true physical observable, and due to its substantial information content, the electron density is a primary source of insight into the electronic structure of atoms, molecules or solids. At hand of Bader's QTAIM[1] (Chapter 3) not only quantum-chemically computed densities but also densities obtained experimentally by high-resolution X-ray diffraction and subsequent multipole refinement can be analyzed and evaluated.[2, 3] Consequently, the comparison of key topological indices of quantum-chemically computed and experimentally determined charge-density distributions has become an important field (see, e.g. refs. [4-15]). In many cases the qualitative features of experimentally and theoretically derived densities agree well. This holds, for example, for the presence or absence of bond critical points, or for the number or position of

attractors in the negative Laplacian, $-\nabla^2\rho$. On the other hand, deeper comparisons reveal often notable and qualitative differences (see ref. [16] and references therein) when discussing, e.g., the bond critical point (BCP) properties. This may have various reasons ranging from (a) deficiencies in the quantum chemical level (basis sets, electron correlation), (b) deficiencies in the quality of the experimental data set, (c) deficiencies in the multipole refinement procedure, and (d) differences between the electron densities measured in the solid state and those obtained from the (in most cases) gas-phase quantum chemical calculations (for various discussions of these points, see refs [4, 7, 8, 10-15]). Subsequently, especially the last point will be address. It seems particularly crucial, as an understanding of the environmental effects on the QTAIM parameters will allow the significance of the other aspects to be extracted. In particular, this is important for gaining better insight in the inaccuracies of the multipole refinement. Moreover, the influence of the environment on charge density and bonding of a molecule or cluster in a condensed-phase environment is also of fundamental importance in its own right.

In principle, a comparison of gas-phase calculations to explicit solid-state calculations with periodic boundary conditions (PBC) may provide the answer seeked. However, the PBC all-electron calculations on solids needed for charge-density studies are usually restricted to a) relatively small unit cells, b) Hartree-Fock (HF) or density functional theory (DFT) calculations and c) often limited basis sets in the case of atom-centered basis functions (as, e.g., in the frequently used CRYSTAL code[17], see also Chapter 10). In contrast, quantum-chemical methods for molecules provide much more flexibility regarding these computational aspects and can be done, e.g., at post-HF ab initio levels, with extended basis sets including diffuse functions, or in relativistic 2- and 4-component frameworks when dealing with compounds of heavier elements. Furthermore, the system size accessible is substantially larger. Differences between charge-density characteristics computed for the isolated molecule and the crystal have so far been examined mainly for hydrogen-bonded arrangements of some organic molecules.[7, 11-14] Then the environmental effects tended to be restricted to those parts of the molecules involved directly in hydrogen bonding. Explicit solid-state calculations are also often performed for typical ionic solids, but then usually there is no comparison to the gas phase (see for example refs. [18-21] and references therein).

Within the more general study of charge density and bonding in solids with polar metal-ligand bonds as, e.g., in organolithium compounds, explicit PBC all-electron calculations will often be limited due to the size of the unit cell and possibly low symmetry. This is related to the extended organic substituents and/or the additional chelate ligands coordinated to the electropositive metal centers. These systems nevertheless may exhibit pronounced interactions with their surroundings due to their polarity. Primary examples are the synthetically important organolithium compounds. They are known to exhibit large electrostatically dominated interactions in oligomers, chains, 2D or 3D networks. These intermolecular interactions are in turn of fundamental interest as they determine the chemical reactivity.

Alternatives to model environmental effects on charge-density distributions in such systems are thus needed. Hence, the primary aim of this chapter is the evaluation of the embedded-cluster approaches introduced in Chapter 10, which so far had not been studied in the context of charge-density analyses. Subsequently, the performance of a) the polarizable continuum models (PCM)[22-25] and b) the recently proposed periodic electrostatic embedded cluster model (PEECM)[26] compared to full PBC calculations will be surveyed.

During the course of the present work, Neugebauer *et al.*[27, 28] reported embedded-cluster QTAIM studies using Wesolowski's frozen-density embedding scheme.[29] The emphasis was on approximations to the kinetic-energy contribution of the embedding potential for coordinative bonds in $[F\text{-}H\text{-}F]^-$,[27] the BH_3….NH_3 complex, and the two transition-metal complexes $TiCl_4$ and $[Cr(CO)_6]$.[28] Our focus will be on crystal environmental effects in polar organometallics, and we will examine two different types of less sophisticated embedding schemes. As test case, the methyllithium (CH_3Li) crystal has been chosen. CH_3Li is the prototypical organolithium compound and of general interest in its own right. The crystal is highly symmetrical ($I\bar{4}3m$ space group) and thus a very suitable polar-organometallic benchmark system accessible to explicit PBC solid-state charge-density analyses. The intermolecular interactions between the $(CH_3Li)_4$ tetramers are known to be significant, to the extent that the preferred conformation of the methyl ligands differs between the crystal and the isolated (gas-phase) tetramer.[30] The interaction energies between the tetramers are thought to be substantial, and they invert the conformational preferences.[31] Furthermore, $[CH_3Li]_{4,\infty}$ is insoluble in non-donor solvents, and reactions are only possible if the $[CH_3Li]_{4,\infty}$ network is prized open by

donors. Changes in C–Li bond lengths in the solid compared to the isolated tetramer are further indications of appreciable intermolecular interactions. The PBC charge-density results will be used to validate the embedded-cluster schemes.

11.1 Computational Details

The abovementioned frozen-density embedding is expected to recover a significant portion of the environmental effects but involves significant effort in its implementation and application. While we appreciate its usefulness, two simpler models will be evaluated herein, a) the polarizable continuum models (PCM, Chapter 10.2.1)[22-25] and b) the recently proposed periodic electrostatic embedded cluster model (PEECM, Chapter 10.2.2).[26]

11.1.1 Embedded-Cluster Calculations

All single point calculations of isolated or embedded clusters were done with the TURBOMOLE 5.10[32-34] package. Coordinates were taken from the X-ray and neutron diffraction studies of Weiss *et al.*[35] Unfortunately, no high-resolution experimental charge-density data appear to be currently available. To extract exclusively the direct electronic effects of the environment, the structures have not been reoptimized at the various levels. All single-point calculations were done with an m5 grid and an SCF convergence threshold of 10^{-10} a.u.. For the PCM we employed Klamt's conductor-like screening model, as implemented in the COSMO[36] module of TURBOMOLE, with an infinite dielectric constant ε (results with finite ε differed relatively little and are not provided separately). Similarly, the PEECM calculations used the implementation in TURBOMOLE 5.10.[26] Full point charges were employed throughout. Lower charges enable a stepwise transition from isolated to full-point charge surrounding (for the dependency of BCP properties on employed charge models, see Appendix B). In the intermediate ECP layer of some of the PEECM models, ECPs were used for the Li cations.[37] Subsequent QTAIM analyses of all molecular or embedded-cluster calculations employed the AIM2000[38] program.

11.1.2 Solid-State Calculations

To enable direct comparison with the embedded cluster approaches, explicit PBC solid-state benchmark calculations on the CH_3Li crystal were done with the CRYSTAL06[17] code, which employs Gaussian basis sets. The default SCF convergence threshold of 10^{-8} a.u. was used. One- and two-electron integrals were truncated at pseudo-overlap thresholds below 10^{-16} a.u.. For the separation into short- and long-range interactions with respect to the Ewald summation, a penetration threshold of 10^{-8} a.u. was set. For k point integration a Pack-Monkhorst shrinking factor of 8 was applied. The charge-density distributions obtained with CRYSTAL have been analyzed with a development version of the TOPOND08 program.[39] We note in passing that comparable calculations with CRYSTAL98 gave somewhat different results, and results for the isolated tetramer differed significantly from the TURBOMOLE results, which was not the case for the CRYSTAL06/TOPOND08 combination (see below).

11.1.3 Functionals

For the incorporation of electron correlation, all calculations were done with density functional theory (DFT) methods. The direct comparison between embedded-cluster and PBC calculations was possible with the gradient-corrected non-hybrid BP86[40, 41] and the hybrid B3LYP[42-45] functional.

11.1.4 Basis Sets

The choice of the CRYSTAL code and atom-centered Gaussian basis sets for the PBC benchmark calculations has the advantage that identical basis sets may be employed as in the embedded-cluster calculations. There is a limitation to this: in the embedded-cluster calculations, we want to use extended basis sets with polarization and diffuse functions to describe as accurately as possible the QTAIM parameters. However, such basis sets usually cannot be employed in the CRYSTAL PBC calculations, as the most diffuse exponents will lead to numerical linear dependencies in the solid-state basis set and severe SCF convergence problems.[46, 47]

Initially, we were able to converge the PBC calculations only at BP86 level after significant modification of the TZVP[48] basis sets we had intended to use for the QTAIM

studies: a) the two most diffuse Li s-functions (α = 0.077, 0.0289) were replaced by two somewhat larger exponents (α = 0.0967, 0.0459) taken from a QZV basis.[49] On carbon, the two most diffuse s-functions (α = 0.2297, 0.09516) were replaced by one exponent (α = 0.1730, from the DZ basis[50]), and the outermost p-functions (α = 0.28888, 0.1006) were replaced by less diffuse ones (α = 0.4605, 0.1894, from the QZV basis[49]). On hydrogen, the two most diffuse s-functions (α = 0.3273, 0.1031) were replaced (α = 0.5193, 0.1541[51]). As will be seen below, this modified basis set, in the following denoted mod-TZVP, still gave reasonable charge-density distributions in the molecular calculations and allowed the direct comparison between the full crystal and embedded-cluster models.

Subsequently, we were able to converge B3LYP PBC calculations after only minor modification of the TZVP basis set. That is, we only removed the most diffuse s-function on Li (Li-TZVP-s basis). As this omission affected the results of the cluster calculations very little (*vide infra*), a direct comparison between B3LYP/TZVP molecular calculations and B3LYP/Li-TZVP-s PBC results became possible. We will report this comparison as well as the previous extensive BP86/mod-TZVP comparison, as the combination of the two levels provides additional insights into the effects of basis sets and functionals.

11.1.5 QM Cluster Definitions

The different definitions of QM clusters and ECP layers are illustrated in Figure 11.1, and the various embedding schemes are detailed in Table 11.1. The limiting cases of the comparison are the isolated $(CH_3Li)_4$ tetramer (model **1a**) and the full PBC calculation of the CH_3Li crystal (**4**). The smallest QM cluster in the embedding schemes (models **2a**, **3a**) is again the tetramer, which may be viewed as a Li_4 tetrahedron with face-capping methyl groups (Figure 11.1a). The first extensions explicitly or indirectly include the next neighbors within the unit cell. Within models **2b**, **2b'**, **3b** (Figure 11.1b), the adjacent four Li atoms are replaced by ECPs while the methyl groups are included either as explicit –1.0 point charges at the carbon atoms (model **2b'**) or within the PCM and PEECM embedding (models **2b**, **3b**). The full unit cell of composition $(CH_3Li)_8$, where the tetramer is surrounded by four additional Li atoms interacting with the inner face-

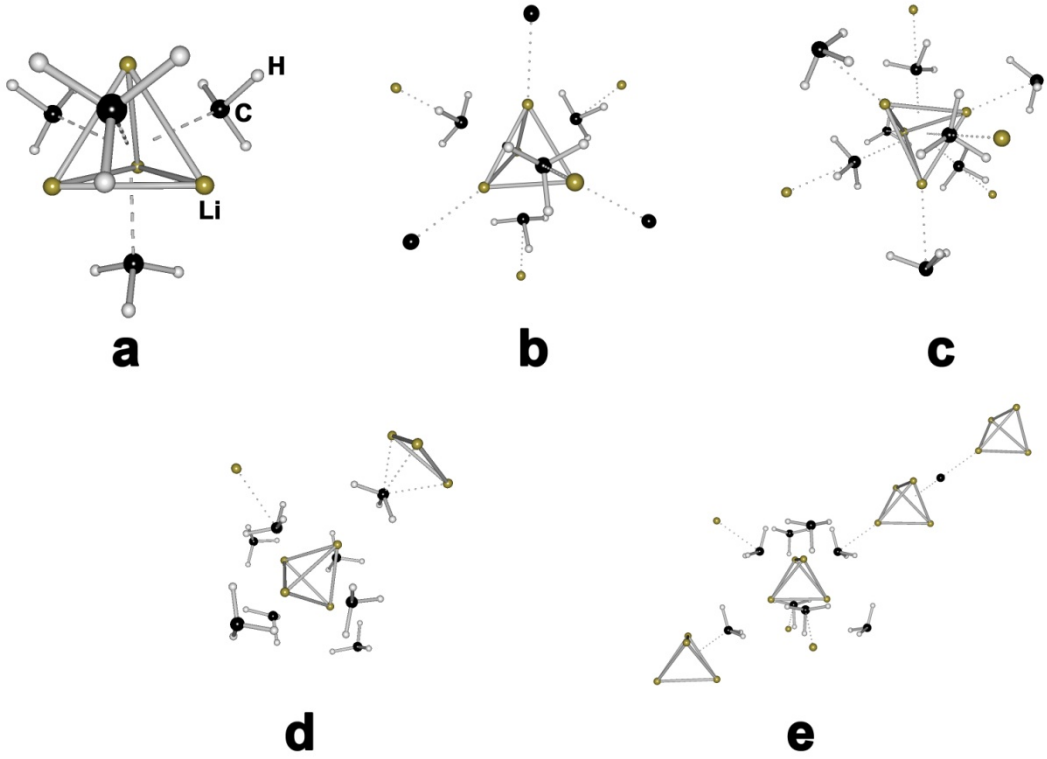

Figure 11.1. QM clusters: a) tetrameric unit, b) tetrameric unit with adjacent Li atoms being replaced by ECPs and C by point charges c) unit cell, d) unit cell with adjacent Li ECPs indicated (for clarity, only 4 of the 28 Li atoms of the ECP layer are shown), and e) schematically illustrated 2x2x2 supercell. Colors of the atoms: Li gold, C black, H white.

capping methyl groups, and four additional methyl groups pointing their hydrogen atoms towards the corners of the inner Li_4 tetrahedron, is contained quantum-mechanically in models **1c**, **2c** and **3c** (Figure 11.1c). Within the PEECM approach, this cluster has either been embedded directly into the point-charge field (model **3c**) or was surrounded first by a layer of 28 lithium cation ECPs (model **3d**, Figure 11.1c). The largest QM region is a full 2x2x2 supercell (schematically illustrated in Figure 1d; models **2e**, **3e**). For benchmarking purposes a full solid-state calculation was performed taking the periodicity of the crystal into account (**4**).

11.1.6 Location of BCPs and AIM Basin Integration

Within AIM2000 the threshold for bcp location was set at 10^{-9} a.u. for the distance of consecutive points and at 10^{-7} a.u. for the norm of the gradient. Standard adjustment was also employed for the basin integrations. If the Laplacian within the basin integrated to

less than 0.005 ebohr^{-5} and electro-neutrality for the tetramer was satisfied within less than 0.25 e, integration data was accepted; otherwise the procedure was repeated applying higher accuracy of the integration step. Identical criteria were employed for TOPOND08 integrations.

Table 11.1. Labeling of isolated and embedded cluster models and PBC benchmark system.

Model		Units	Classification
1	**isolated QM cluster**		
	1a	$(CH_3Li)_4$	tetrameric unit
	1c	$(CH_3Li)_8$	unit cell
2	**QM Cluster + PCM**		
	2a	$(CH_3Li)_4$	tetrameric unit
	2b	$(CH_3Li)_4$	tetrameric unit + ECP layer
	2b'	$(CH_3Li)_4$	tetrameric unit + ECP and point charge layer
	2c	$(CH_3Li)_8$	unit cell
	2e	$(CH_3Li)_{64}$	2x2x2 supercell
3	**QM Cluster + PEECM embedding**		
	3a	$(CH_3Li)_4$	tetrameric unit
	3b	$(CH_3Li)_4$	tetrameric unit + ECP layer
	3c	$(CH_3Li)_8$	unit cell
	3d	$(CH_3Li)_8$	unit cell + ECP layer (Figure 1c)
	3e	$(CH_3Li)_{64}$	2x2x2 supercell
4	**PBC**		
	4	$(CH_3Li)_\infty$	full crystal

11.2 Results and Discussion

We will first focus on the density, ρ, and the Laplacian, $\nabla^2\rho$, at the Li–C and C–H bond critical points (BCPs) as parameters to be evaluated. Table 11.2 shows the results for the various isolated and embedded clusters compared to the full PBC crystal calculation. Direct comparison between molecular and solid-state calculations has been possible at the BP86/mod-TZVP and B3LYP/TZVP vs. B3LYP/Li-TZVP-s levels, respectively.

We note first of all, that B3LYP/TZVP calculations for the isolated tetramer (**1a**) with TURBOMOLE+AIM2000 and with CRYSTAL06/TOPOND08 give virtually identical results, justifiying the subsequent comparison between embedded-cluster calculations using the former and PBC calculations using the latter combination of codes. Removal of the most diffuse s-function from the Li TZVP basis set affects the Li–C BCP properties negligibly and the C–H BCP properties slightly (B3LYP/TZVP entries). Changes in the ratio of the bond-path lengths (d_1/d_2) are more notable but should probably not be overrated in view of the overall small changes and the difficulties in locating the BCP very accurately (BCP shifts of the indicated magnitude affect the BCP properties negligibly).

At BP86/mod-TZVP(B3LYP/TZVP) levels, the differences between the isolated tetramer (**1a**) and the periodic crystal (**4**) are consistently notable but not dramatic. At the Li–C BCP, the crystal environment reduces ρ by 0.010(0.005) eÅ^{-3}, and the Laplacian by 0.059(0.046) eÅ^{-5}. At the C–H BCP, ρ is increased by 0.052(0.054) eÅ^{-3}, and the absolute value of the Laplacian by 0.939(0.919) eÅ^{-5}. The enhanced charge accumulation at the C–H BCP is the most notable change. However, in percentage, the electron density decrease at Li–C (–6,8%;–3,6%) and the electron density increase at C–H (+2,9%; +3%) BCPs are qualitatively similar in magnitude. It seems that, in spite of the large electrostatic interactions mentioned in the introduction, the direct polarization of the charge density within the tetrameric unit is relatively moderate. Nevertheless, it is these differences that are relevant and that we aim at in the embedded-cluster modeling (see also introduction). Note that all calculations provide qualitatively similar density distributions with predominantly ionic Li–C bonds (small ρ and positive $\nabla^2\rho$) and predominantly covalent C–H bonds (large ρ and negative $\nabla^2\rho$).

We start the evaluation of the various cluster models at the BP86/mod-TZVP level. Going from the isolated tetramer to a full unit cell (yet still without embedding) provides already a large change. In fact, for most parameters, this model overestimates the environmental effects somewhat, i.e. we observe some overshooting. The interactions with the nearest neighbors of the tetramer are thus very important but seem to be cancelled partly by more longer-range interactions (note that computation of the full unit cell may not always be possible for more complicated compounds and crystal structures). Extension to the 2x2x2 supercell without embedding failed due to SCF convergence problems (but the supercell could be converged after embedding, see below).

Starting our embedding validation with the polarizable continuum model, we see that the properties of the tetramer within a PCM environment are still close to those of the isolated tetramer. The inclusion of a Li ECP layer in model **2b** slightly moves the C–H BCP properties essentially to the full crystal values, whereas the Li–C BCP data are still relatively poor. Addition of explicit point charges at the outer carbon positions (model **2b'**) brings no further benefit (the Laplacian at the Li BCP remains too large whereas the density becomes too low). The BCP properties of the full unit cell, while already significantly better than those of the tetramer, are altered only little by the PCM (the density at the Li–C BCP is improved somewhat). That is, even with the infinite dielectric constant chosen, the environmental effects may be simulated only to a very limited amount by a PCM embedding. While we could not converge an isolated 2x2x2 supercell (**1e**), this was successful upon PCM embedding (**2e**). The result has obviously already converged to the full PBC target numbers. This indicates that the large supercell recovers almost all of the crystal environmental effects on the central tetramer and would likely need no further embedding (except for the convergence problems). However, use of such large supercells will typically not be feasible for more complex systems.

In principle, a more realistic and efficient description of the crystal environment is expected by the PEECM embedding. However, direct embedding of the tetramer in the point-charge field (**3a**) provides only a partial solution: The C–H BCP parameters are now already in excellent agreement with the periodic crystal results, and so is the density at the Li–C BCP (BP86/mod-TZVP results). Yet the Laplacian at the Li–C BCP is unaffected (compared to **1a**). Inclusion of a Li ECP intermediate layer (**3b**) helps only little in this context (the Laplacian at the C-H BCP is improved further by the ECP layer). It appears that overpolarization of the charge density within the tetramer by the PEECM embedding field is a problem. The embedded full unit cell (**3c**) reproduces the crystal results already almost perfectly. Interestingly, introduction of an ECP layer (**3d**) in this case does not improve the agreement but worsens it very slightly. It seems possible that the ECPs introduce some errors. In any case, for the $(CH_3Li)_8$ unit cell, ECP embedding is not needed, as neither overpolarization nor leaking out of charge seem to be an issue. No significant further improvement is thus possible or necessary in case of PEECM embedding by going to the 2x2x2 supercell (**3e**).

Table 11.2. BCP properties for the methyl lithium crystal using different computational models

Method/ basis set	Model	Li–C BCP			C–H BCP	
		ρ [eA^{-3}]	$\nabla^2\rho$ [eA^{-5}]	d_1/d_2[a]	ρ [eA^{-3}]	$\nabla^2\rho$ [eA^{-5}]
BP86/mod–TZVP						
Isolated	**1a**	0.147	2.303	0.535	1.798	–20.415
	1c	0.128	2.249	0.547	1.872	–22.208
PCM	**2a**	0.143	2.316	0.535	1.796	–20.295
	2b	0.140	2.319	0.535	1.847	–21.163
	2b'[b]	0.134	2.316	0.537	1.840	–21.000
	2c	0.134	2.251	0.548	1.849	–21.351
	2e	0.137	2.246	0.542	1.851	–21.393
PEECM	**3a**	0.139	2.328	0.535	1.843	–21.136
	3b	0.139	2.311	0.536	1.847	–21.136
	3c	0.137	2.252	0.542	1.851	–21.382
	3d	0.140	2.305	0.536	1.848	–21.176
PBC crystal	**4**[c]	0.137	2.244	0.547	1.850	–21.354
BP86/TZVP						
Isolated	**1a**	0.141	2.338	0.538	1.785	–19.560
PEECM	**3c**	0.135	2.300	0.549	1.840	–20.533
	3d	0.134	2.320	0.541	1.838	–20.358
B3LYP/TZVP						
isolated	**1a**	0.139	2.354	0.537	1.800	–20.135
	1a[d]	0.139	2.355	0.549	1.816	–20.456
	1a[c]	0.140	2.359	0.539	1.817	–20.457
	1c	0.125	2.288	0.543	1.858	–21.281
PCM	**2a**	0.134	2.360	0.541	1.799	–20.095
	2b	0.133	2.354	0.539	1.851	–20.913
	2b[b]	0.125	2.341	0.543	1.846	–20.852
	2c	0.131	2.315	0.543	1.853	–21.085
PEECM	**3a**	0.124	2.331	0.546	1.859	–21.482
	3b	0.131	2.353	0.540	1.853	–20.945
	3c	0.134	2.316	0.541	1.857	–21.140
	3d	0.133	2.338	0.537	1.854	–20.978
	3e	0.134	2.311	0.541	1.854	–21.062
PBC crystal	**4**[c,d]	0.134	2.308	0.539	1.854	–21.054

[a]Ratio between Li-BCP and BCP-C distances. [b]Explicit –1.0 point charges added at outer methyl carbon atoms within the unit cell. [c]CRYSTAL06/ TOPOND08 results. [d]Most diffuse Li s function omitted (Li-TZVP-s basis).

The effect of the initial truncation/modification of the basis set has been evaluated for a few cluster calculations by comparing BP86/mod-TZVP and the full BP68/TZVP results (Table 11.2). TZVP is usually considered a reasonable basis set for DFT-based

charge density analyses (still larger basis sets may be needed in post-HF calculations). For the isolated tetramer (**1a**), BP86/TZVP compared to BP86/mod-TZVP provides the following changes: ρ(Li–C) -0.006 eÅ^{-3}, $\nabla^2\rho$ (Li–C) +0.035 eÅ^{-5}, ρ(C–H) –0.013 eÅ^{-3}, $\nabla^2\rho$ (C–H) –0.855 eÅ^{-5}. These are significant differences, at the same order of magnitude as the overall crystal environmental effects, in particular for the crucial Laplacian at the C–H BCP. It is sometimes assumed that the basis-set incompleteness in full solid-state calculations is diminished by "borrowing" of basis functions from more remote neighbor positions. However, the TZVP *vs*. mod-TZVP differences for the PEECM-embedded unit cell (**3c**) are not much different from those of the isolated tetramer: ρ(Li–C) –0.002 eÅ^{-3}, $\nabla^2\rho$ (Li–C) +0.048 eÅ^{-5}, ρ(C–H) –0.011 eÅ^{-3}, $\nabla^2\rho$ (C–H) –0.859 eÅ^{-5}.

The B3LYP/TZVP results exhibit largely the same trends as those discussed above for the series of BP86/mod-TZVP results. Again, results for **2c** results are comparable in quality to those with **3c**: **2c** is slightly better for the C–H bond properties and **3c** marginally improves the Li–C descriptors. Small differences pertain to the density at the Li-C BCP: models **2b'** and **3a** give a more pronounced overshooting of the environmental effects (too low density), whereas this trend seemed to be less pronounced at BP86/mod-TZVP level (*vide supra*). The comparison BP86/TZVP vs. B3LYP/TZVP finally gives us an idea of the influence of the functional on the BCP properties, in particular due to exact-exchange admixture in the B3LYP hybrid functional. Focusing first on the isolated tetramer, **1a**, B3LYP/TZVP compared to BP86/TZVP provides the following changes: ρ(Li–C) –0.002 eÅ^{-3}, $\nabla^2\rho$ (Li–C) +0.016 eÅ^{-5}, ρ(C–H) –0.015 eÅ^{-3}, $\nabla^2\rho$ (C–H) –0.575 eÅ^{-5}. Similar differences are observed (Table 11.2) for the unit cell in PEECM embedding (**3c**). Again, these differences are only a little smaller than the overall environmental effects. That is, in the present example, the embedding is certainly not the only challenge, as basis sets and functional are of similar importance. Future comparisons with exemplary, very accurate experimentally obtained charge densities should provide further insights into an optimal quantum-chemical protocol for embedded-cluster simulations of solid-state charge densities in polar organometallics.

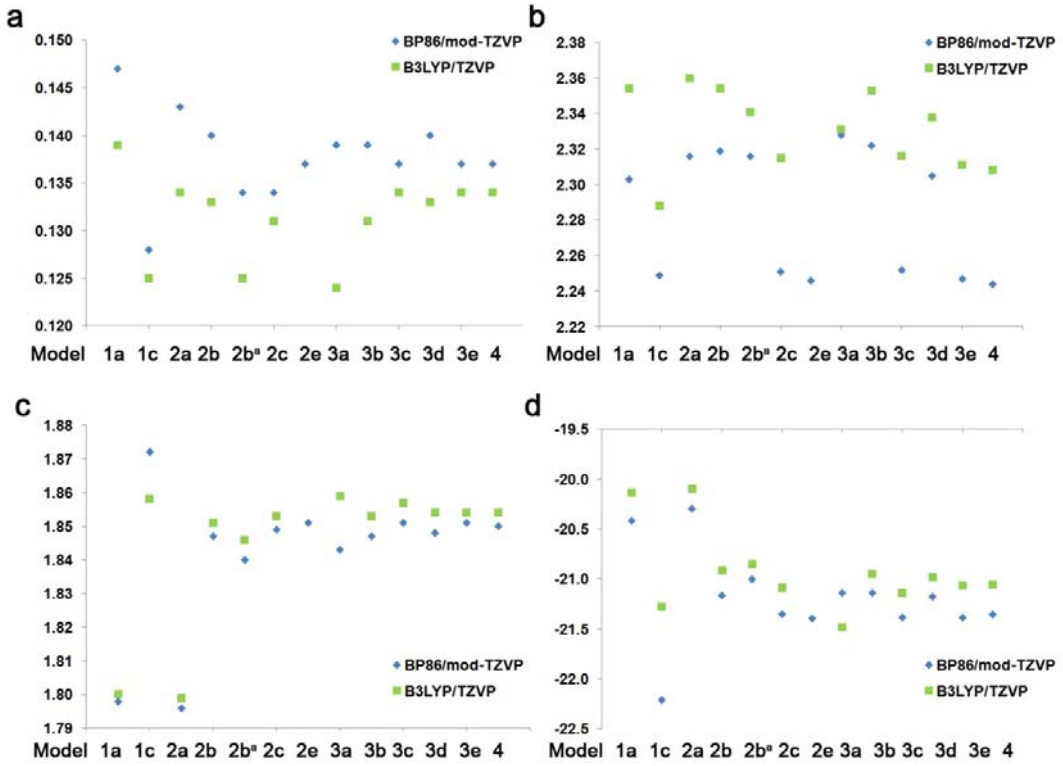

Figure 11.2. BCP properties as function of embedding model, compared to the full solid.-state results (BP86/mod-TZVP results as blue diamonds, B3LYP/TZVP results as green squares). a) ρ (in eÅ^{-3}) at Li–C BCP; b) $\nabla^2\rho$ (in eÅ^{-5}) at Li–C BCP; c) ρ (in eÅ^{-3}) at C–H BCP; d) $\nabla^2\rho$ (in eÅ^{-5}) at C–H BCP.

As additional, possibly even more challenging parameters, we have also looked at QTAIM charges obtained by integrating the electron density over the atomic basins. Atomic charges provide some additional insight into the influence of crystal environment and other computational parameters on bond polarity, but the small differences between the different models and the large sensitivity to the integration parameters and to charge leaking renders the results less informative. The data are provided in Table C1 in Appendix C. Here we mention only briefly that compared to the isolated tetramer (**1a**), the crystal environment (**4**) reduces somewhat the positive charge on Li and the negative charge on C and enhances slightly the negative charge on H. An isolated unit cell (**1c**) overestimates these environmental effects. PCM embedding of a tetramer (**2a**) captures largely the effects on the C and H charges but not on the Li charges. A PEECM embedded supercell (**3d**) provides good agreement with the full periodic solid data.

11.3 Conclusions

The present test case for our validation study, the CH_3Li crystal, is expected to be representative for organolithium compounds and other polar organometallics with comparably high ionic character in general. In spite of the obviously large electrostatic interactions between the $(LiCH_3)_4$ tetramers in the crystal, the overall environmental effects on the properties of the charge density at the Li–C and C–H BCPs within the tetrameric unit turned out to be rather moderate. Yet, the effects are sufficiently large to evaluate various embedded-cluster schemes. First of all, extension of the QM cluster from the tetramer to a full unit cell overestimates the environmental effects somewhat. A 2x2x2 supercell provided essentially quantitative agreement with the reference solid-state calculations. These types of cluster definitions may not always be computationally affordable for more complicated systems. Embedding of just the tetramer into either PCM or PEECM surroundings provided an insufficient description of the environmental effects. In case of PEECM, this may be a result of overpolarization. As soon as a full unit cell was embedded, results were almost converged to the periodic crystal data.

The choice of basis sets and general computational method (in the present case the exchange-correlation functional) have been shown to influence the charge density to a similar extent as the environmental effects. In this context, if crystal environmental effects are to be included, embedded-cluster schemes like PEECM have distinct advantages over explicit solid-state calculations using periodic boundary conditions: molecular calculations provide much larger freedom with respect to theoretical level and basis sets employed. In the future, embedded-cluster calculations at high computational levels should allow the elimination of most computational errors in charge-density studies of crystals containing polar metal-ligand bonds. Then the inherent errors of experimental charge-density distributions and of the underlying multipole refinement procedures may be evaluated in more detail than possible hitherto.

Chapter 12

Understanding the Structure-Reactivity Relationship of Methyllithium Base-Adducts

An important and ubiquitous structural motif in organolithium chemistry is the formation of aggregates and oligomers, as introduced in Chapter 9. Although other features may additionally influence the structure formation (Chapter 9.1), electrostatic interactions are the driving force in many cases and favor arrangements with a maximum of coordination partners. In general, all interactions enabling an optimal charge distribution result in an increased stability and decreased reactivity of the lithium compound. Therefore, Lewis bases are added to cleave the oligomeric structures to smaller and more reactive organolithium adducts. Accordingly, many examples of dimeric or even monomeric alkyllithium structures have been reported in recent years.[1-6] However, the changes in the electronic structure upon deaggregation and base complexation are still an open

question. Broadly it is assumed that the Li–C bond polarity is increased during the deaggregation procedure, explaining the increased reactivity observed for dimers or monomers compared to their higher aggregated equivalents (see e.g. ref. [7]). The elucidation of this feature will be one of the main issues of the subsequent chapter and has been carried on the basis of experimental as well as theoretical data in collaboration with *V. H. Gessner* and *C. Strohmann* (TU Dortmund). Based on crystal structures obtained for a series of alkyllithium compounds, the structural and electronic differences have been studied by means of X-ray diffraction and DFT methods. To gain insight into the fine details of polarity changes, QTAIM, NPA and NLMO analysis have been taken out on a sequence of isolated clusters as well as Lewis base adducts.

12.1 Computational Details

All single point calculations of isolated and embedded clusters were done with the TURBOMOLE 5.10 package[8-10] at the TZVP/BP86[11-14] level of theory. Coordinates were taken from the X-ray and neutron diffraction studies published by *Weiss et al.*[15] or obtained by *Strohmann et al*. For the PCM, Klamt's conductor-like screening model was employed, as implemented in the COSMO[16] module of TURBOMOLE, with an infinite dielectric constant ε. The PEECM (*Sauer et al.*) calculations used the implementation in TURBOMOLE 5.10.[17] Full point charges were employed throughout. Lower charges did not lead to significant changes (results not shown). Subsequent QTAIM analyses of all molecular or embedded-cluster calculations employed the AIM2000[18] program. NPA and NLMO analyses were taken out with the NBO3.1 tool in Gaussian03[19] at the TZVP/BP86[11-14] level of theory.

12.2 Structure Formation and Agostic Interactions

In the previous chapter several techniques were reported for the efficient and sufficiently accurate description of the solid-state charge distribution of methyllithium. Embedding techniques have been partly employed during the structure optimization procedure in contrast to the preceding study, which was solely based on coordinates taken from neutron and X-ray diffraction results and keeping them fixed during the wavefunction optimization. In the following, it will be investigated if the correct solid-state

configuration for isolated clusters as well as Lewis base adducts can be obtained from structure optimizations with respect to the experimentally derived coordinates. In extension to the previous study, methyllithium was chosen as it is the smallest organolithium compound with no interfering impacts of further substituents at the carbanionic centre.

12.2.1 Experimental Background and X-ray Structure Determination

Only a few adducts are known of tetrameric MeLi, namely $[MeLi \cdot THF]_4$[20] and $[(MeLi)_4 \cdot 4\ TMEDA]_\infty$[21]. The commercially available MeLi is mainly provided in Et_2O, but this most crucial adduct has not been structurally characterized until very recently. *Strohmann et al*. have succeeded in the isolation and X-ray characterization of $[MeLi \cdot Et_2O]_4$ (**17**, see Figure 12.1).[22] In the course of this chapter only the most important details of the crystallographic investigation are summarized, and further information can be found elsewhere (see ref. [23]).

The Li–Li distances within **17** are found to be 2.525(7) Å and 2.565(5) Å with interior angles between 58.72(17)° and 61.01(12)°. The Li_3 faces of the tetrahedron are μ_3-capped by the methyl groups, comparable to the isolated $[MeLi]_{4,\infty}$ structure, with Li–C distances being in the range of known oligomeric lithiumalkyls (2.249(5) Å to 2.267(5) Å).[7] Additionally, the lithium atoms are apically coordinated by diethyl ether molecules as is also observed for the THF adduct, thus completing the coordination sphere of the lithium atom. Regarding additional stabilizing and agostic effects, it is noteworthy that all hydrogens of the methyl units adopt an intermediate position between staggered and eclipsed arrangement in contrast to the pure methyllithium crystal.

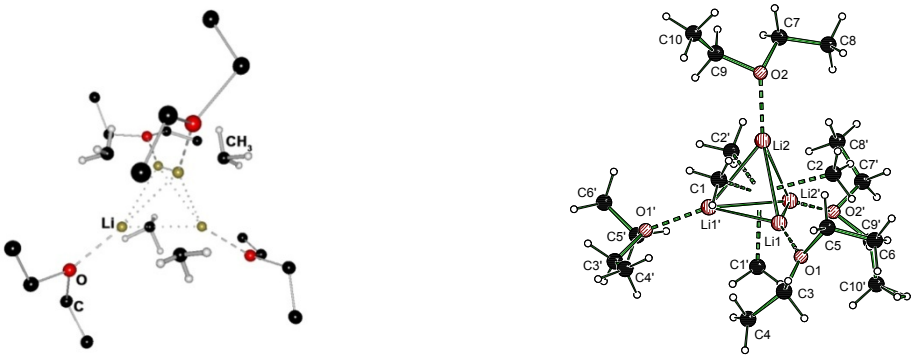

Figure 12.1. Molecular structure of $[MeLi \cdot Et_2O]_4$ (**17**) determined by *V. Gessner*; hydrogen atoms of diethyl ether molecule are omitted in the left picture.

Previous studies have shown that the cleavage of polymeric methyllithium to smaller adducts, in particular dimers, is restricted to strongly coordinating ligands. Thus far, only three dimeric methyllithium complexes have been isolated and characterized by *Strohmann et al.*, namely the adducts [MeLi·(*R*,*R*)-TMCDA]$_2$ (**18**) and its racemic mixture with (*S*,*S*)-TMCDA (**19**), and [MeLi·(–)-sparteine]$_2$ (**20**) and one of its (+)-surrogates (substitute of one enantiomer) (**21**).[23, 24]

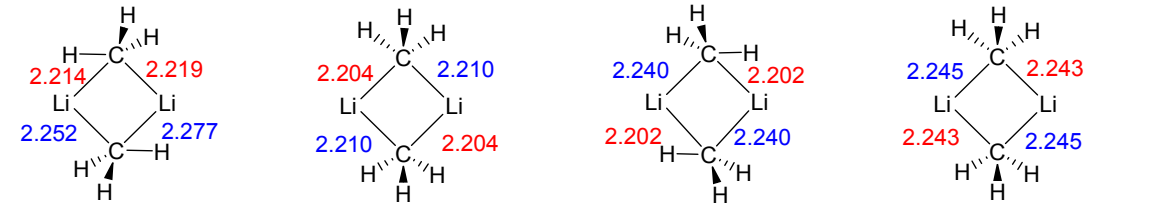

[MeLi·(*R*,*R*)-TMCDA]$_2$ **18** | [MeLi·*trans*-TMCDA]$_2$ **19** | [MeLi·(–)-sparteine]$_2$ **20** | [MeLi·(+)-sparteine-surrogate]$_2$ **21**

Figure 12.2. Li-C distances [Å] and arrangement of the methyl hydrogen atoms in dimeric methyllithium structures obtained from X-ray diffraction. Similar bond lengths are marked pairwise in red and blue.

An overview of detected Li–C bond lengths and the conformational arrangement of the methyl hydrogen atoms towards the lithium centers in dimeric adducts is given in Figure 4.2 (see also Figure 13.3). For [MeLi·(*R*,*R*)-TMCDA]$_2$ (**18**) the Li–C distances range pairwise between 2.219 Å and 2.277 Å, with one carbon center exhibiting slightly shorter bond lengths. Furthermore, one hydrogen atom of each methyl group is situated eclipsed towards the lithium atom suggesting Li···H interactions. In contradiction, the *trans*-TMCDA adduct **19** features only staggered hydrogen atoms and an opposed arrangement of slightly shorter (2.204 Å) and elongated (2.210 Å) Li–C distances. A comparable situation is observed in **20**, with Li–C bond lengths ranging from 2.202 Å to 2.240 Å. However, the conformation of the methyl group is found to be staggered with respect to the Li centers. Within the sparteine-surrogate **21**, the bond length differences are negligible and the methyl hydrogen atoms are arranged in staggered conformation.

12.2.2 Optimized Structures

As discussed in chapter 9.1, the intermolecular interactions in the pure [MeLi]$_{4,\infty}$ are known to be significant, to the extent that the preferred conformation of the methyl ligand differs between solid-state and gas-phase tetramer.[25, 26] While the μ_3-methyl hydrogen

Table 12.1. Selected bond lengths and angles of experimentally and theoretically derived structures.

Compound	Li–C [Å]	Li···H(D) [Å]	Li–C–Li [°]	H–C–Li–Li [°]
[MeLi]				
full optimization (gas-phase, tetramer)	2.207	2.228-2.239	66	0
PEECM optimization (embedded, unit cell + ECP layer)	2.264	2.457	68	60
neutron diffraction[15] (solid-state, deuterated)	2.256	2.454	70	60
[MeLi·Et_2O]$_4$ (**17**)				
full optimization (gas-phase)	2.251-2.292	2.27-2.42	68	20-35
X-ray diffraction (solid-state)	2.249-2.267	-[a]	68-69	-
[MeLi·(*R,R*)-TMCDA]$_2$ (**18**)				
full optimization (gas-phase, dimer)	2.218, 2.224[b] 2.222, 2.239	2.30-2.38 2.50-2.76	65	<18[c] >34
X-ray diffraction (solid-state)	2.214, 2.219 2.252, 2.277	-	65	-
[MeLi·(*trans*)-TMCDA]$_2$ (**19**)				
full optimization (gas-phase, dimer)	2.222, 2.223 2.227, 2.230	2.36-2.41 2.85	65	30-40 90
X-ray diffraction (solid-state)	2.204 2.210	-	65	-
[MeLi·(–)-sparteine]$_2$ (**20**)				
full optimization (gas-phase, dimer)	2.240 2.241	2.24 2.54-2.72	66	<15 50-70
X-ray diffraction (solid-state)	2.202 2.240	-	67	-
[MeLi·(+)-sparteine-surrogate]$_2$ (**21**)				
full optimization (gas-phase, dimer)	2.235 2.237	2.33 2.52-2.99	66	<16 50-70
X-ray diffraction (solid-state)	2.243 2.245	-	67	-

[a]No values obtained from X-ray diffraction. [b]Individual values for all four Li–C bonds, see also Figure 12.2. [c]Only limiting values given due to distortional methyl conformation.

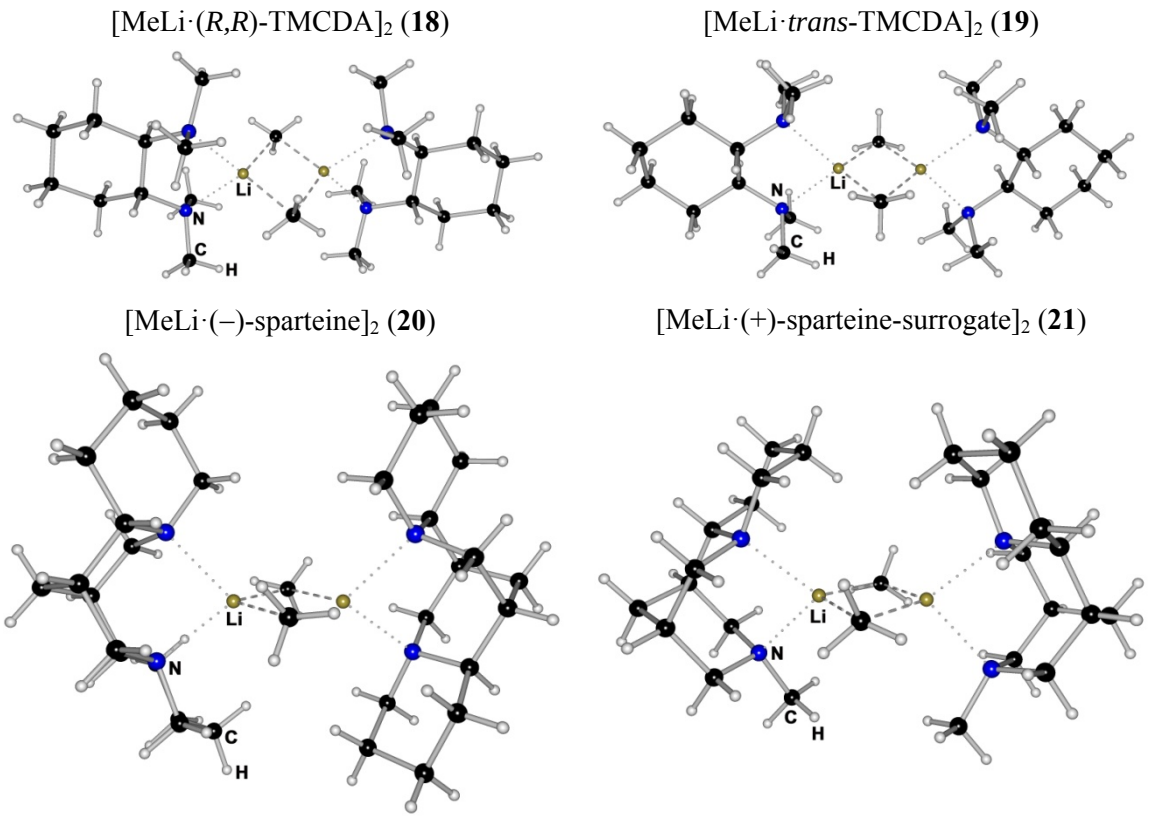

Figure 12.3. X-ray derived structures of **18**-**21**.

atoms are arranged staggered in the crystal, an ecliptic conformation is observed for the isolated gas-phase tetramer. To provide an efficient procedure for the derivation of the correct solid-state configuration, structure optimization routines within the PCM and PEECM embedding schemes were tested. It turns out that the QM simulation of the $[MeLi]_8$ unit cell embedded in the PCM environment is already sufficient to obtain the solid-state staggered conformation of the μ_3-CH_3 groups. Within the PEECM scheme, additional ECP substituted point charges for the adjacent lithium atoms have to be included (model 3c in Chapter 11) and kept fixed during the optimization procedure, otherwise convergence cannot be achieved. The resulting structure is in very good agreement with the neutron diffraction data (Table 12.1, e.g. Li–C distances; theory: 2.237 Å compared to experiment: 2.256 Å) and exhibits the correct conformation of the methyl hydrogen atoms.

For all investigated Lewis base adducts **17-21**, the correct solid-state structure was obtained without employing embedding techniques, and deviations from the X-ray data are within acceptable range (see Table 12.1) Thus, the coordinating Lewis bases shield the interior $[MeLi]_n$ (n=2, 4) clusters from influences of adjacent RLi fragments and

suppress any further intermolecular interactions. Furthermore, the arrangement of the methyl hydrogen atoms is interesting to note. As mentioned before, gas-phase and solid-state conformation of pure methyllithium differ by 60° in the H–C–Li–Li dihedral angle. For the Et_2O adduct **17**, we find, however, an intermediate methyl configuration with a dihedral angle between 20 and 35° in agreement with the X-ray structure[23]. For the dimeric adducts **18**, **20** and **21**, an acute H–C–Li–Li dihedral angle of <20° is observed for one hydrogen atom of each methyl group suggesting direct Li···H interactions. Only for the *trans*-TMCDA compound **19**, a staggered arrangement is detected. Due to the varying H–C–Li–Li dihedral angles, the Li···H distances also vary between 2.23 Å and 2.85 Å. Nevertheless, they are considerably shortened compared to the van-der-Waals radii (2.91 Å).

In comparison to the tetrameric units in the solid-state, the $[MeLi]_2$ entities exhibit slightly shorter Li–C distances (see Table 12.1). However, the differences are marginal. As expected, the Li–C–Li angle is enlarged for the tetrameric structures (66-70°) and more acute for the dimeric units (~65°). The alternation of bond lengths within the $[MeLi]_2$ units observed for the experimentally derived structures is not in all cases reproduced with the same distinction in the theoretical data (see e.g. Li–C bond lengths of **20**). However, the variations are within 0.02 Å and are thus in acceptable range.

Overall, the structural data of pure and coordinated dimeric and tetrameric methyllithium compounds has been modeled within sufficient accuracy by means of PCM and PEECM embedding techniques or as isolated Lewis base adducts. The conformation of the methyl hydrogen atoms was obtained correctly with respect to the changeover from eclipsed to staggered arrangements for gas-phase and solid-state structures, respectively.

12.2.3 Agostic Li···H Interactions

On the basis of the previously discussed structural data, Li···H agostic interactions have been assumed to explain the conformational changes for gas-phase/solid-state $[MeLi]_4$ or $[MeLi{\cdot}(R,R)\text{-TMCDA}]_2$ and $[MeLi{\cdot}trans\text{-TMCDA}]_2$. However, as discussed in chapter 9.2, the investigation of these fine structural details is challenging. In earlier work, the slight polarization of the C–H bond by agostic interactions has been suggested, causing a small charge transfer towards the hydrogen atom and making it a better donor.[27]

Comparing the herein derived NPA charges for different $[MeLi]_n$ (n=1-4) (Table 12.2), a similar tendency can be observed. While the staggered isolated $[MeLi]_4$ tetramer features a hydrogen charge of 0.220 e, its eclipsed analogue provides a decreased positive charge of 0.204 e. A similar trend is found for **18** and **19**, however, the differences are smaller than 0.03 e (**18**, eclipsed hydrogen: 0.177 e; **19**: 0.180 e).

Table 12.2. Averaged NPA charges of isolated and Lewis base coordinated $[MeLi]_n$ clusters.

		Li	C	H	Σ_{CH3}	Σ_{Ligand}
Monomers	[MeLi]	0.830	–1.425	0.198	–0.830	-
	[MeLi·TMCDA] (**22**)	0.790	–1.364	0.182	–0.816	0.026
Dimers	$[MeLi]_2$ (eclipsed)	0.869	–1.489	0.207	–0.869	-
	$[MeLi\cdot(R,R)\text{-TMCDA}]_2$ (**18**)	0.829	–1.402	0.182	–0.856	0.029
	$[MeLi\cdot trans\text{-TMCDA}]_2$ (**19**)	0.829	–1.399	0.181	–0.855	0.028
	[MeLi·(–)-sparteine]$_2$ (**20**)	0.844	–1.426	0.181	–0.885	0.044
	[MeLi·(+)-spart.-sur.]$_2$ (**21**)	0.836	–1.422	0.181	–0.879	0.047
Trimers	$[MeLi]_3$ (eclipsed C_{3v})	0.828	–1.457	0.210	–0.827	-
	$[MeLi\cdot(R,R)\text{-TMCDA}]_3$ (**23**)	0.842	–1.399	0.181	–0.857	0.015
Tetramers	$[MeLi]_4$ (stag.)[a] (**25-A**)	0.850	–1.510	0.220	–0.850	-
	$[MeLi]_4$ (eclipsed)[a] (**25-B**)	0.836	–1.448	0.204	–0.836	-
	$[MeLi]_{8,emb.}$ (stag.)[b] (**25-C**)	0.856	–1.560	0.217	–0.921	-
	$[MeLi\cdot Et_2O]_4$ (**17**)	0.824	–1.446	0.198	–0.853	0.030
	$[MeLi\cdot NEt_3]_4$ (**24**)	0.817	–1.412	0.190	–0.841	0.024

[a]Optimized gas-phase tetramer. [b]Optimized $[MeLi]_8$ unit within PEECM embedding.

In addition, a second order perturbation theory analysis of the Fock matrix in the NBO basis has been performed, to evaluate the interaction energies between lithium centers and eclipsed hydrogen atoms. In analogy to previous studies,[27] we find the maximum interaction energy for the isolated eclipsed tetramer (E=16.622 kJ/mol in comparison to 7.113 kJ/mol for the staggered equivalent). The energies for all other investigated compounds **17-21** range between 6.950 kJ/mol and 12.058 kJ/mol for the strongest Li···H interaction. However, the differences between **18** and **19** are marginal (0.042 kJ/mol) despite the changeover from eclipsed to staggered conformation. Hence, agostic interactions definitely play a role in stabilizing the individual methyllithium conformations, but are only one amongst several features which influence the overall structure formation.

12.3 Electronic Structure Analysis

For a better understanding of the electronic structure of MeLi clusters and their corresponding base adducts, a detailed QTAIM analysis has been performed for a series of isolated and Lewis base coordinated $[MeLi]_n$ (n=1-4) units (see Table 12.3). In addition to the dimeric and tetrameric Lewis-base coordinated structures **17**-**21**, a possible monomeric TMCDA adduct (**22**) as well as the trimeric structure [MeLi·(*R,R*)-TMCDA]$_3$ (**23**) have been evolved by means of structure optimization. Furthermore, the ether molecules in **17** have been replaced by an amino base (NEt_3) to yield **24**, and thus create a complementary series of $[MeLi]_n$ (n=1-4) clusters coordinated by N-ligands. The isolated cluster $[MeLi]_n$ (n=1-3) as well as the staggered (**25-A**), eclipsed (**25-B**) and embedded (**25-C**) $[MeLi]_{8,\infty}$ tetramers have also been included in this study.

Table 12.3. Bond path lengths d(Li–C) [Å], bond path ratios [d_1(Li–BCP)/d_2(C–BCP)], and BCP properties $\rho(\mathbf{r}_{BCP})$ [eÅ^{-3}], $\nabla^2\rho(\mathbf{r}_{BCP})$ [eÅ^{-5}].

		d	d_1/d_2	$\rho(r_{BCP})$	$\nabla^2\rho(r_{BCP})$
Monomers	[MeLi]	1.993	0.555	0.274	4.586
	[MeLi·TMCDA] (**22**)	2.046	0.555	0.206	3.283
Dimers	$[MeLi]_2$ (eclipsed)	2.136	0.547	0.198	3.217
	[MeLi·(*R,R*)-TMCDA]$_2$ (**18**)	2.241	0.541	0.156	2.469
	[MeLi·*trans*-TMCDA]$_2$ (**19**)	2.239	0.542	0.156	2.478
	[MeLi·(–)-sparteine]$_2$ (**20**)	2.254	0.541	0.151	2.388
	[MeLi·(+)-sparteine-sur.]$_2$ (**21**)	2.250	0.541	0.152	2.418
Trimers	$[MeLi]_3$ (eclipsed C_{3v})	2.102	0.560	0.208	3.238
	[MeLi·(*R,R*)-TMCDA]$_3$ (**23**)	2.203	0.552	0.161	2.636
Tetramers	$[MeLi]_4$ (staggered)[a] (**25-A**)	2.245	0.539	0.154	2.585
	$[MeLi]_4$ (eclipsed)[a] (**25-B**)	2.223	0.543	0.160	2.692
	$[MeLi]_{8,\infty}$ (staggered)[b] (**25-C**)	2.264	0.541	0.141	2.446
	[MeLi·Et_2O]$_4$ (**17**)	2.289	0.538	0.137	2.266
	[MeLi·NEt_3]$_4$ (**24**)	2.248	0.542	0.152	2.512

[a]Optimized gas-phase tetramer. [b]Optimized $[MeLi]_8$ unit within PEECM embedding.

12.3.1 General Aspects of Li–C Bonding in MeLi Clusters and Adducts

Within the topological analysis, all expected bond, ring and cage critical points were detected. The BCP properties of all Li–C bonds feature low $\rho(\mathbf{r}_{BCP})$ and positive $\nabla^2\rho(\mathbf{r}_{BCP})$ values, typical for very polar metal–element interactions (see Table 12.3). From the obtained data, it is, however, dubious to judge the precise degree of covalency

of the individual Li–C bonds. The features observed for the studied series of organolithium compounds correspond to a strongly polarized bond nature, involving a minor part of covalent attraction mirrored in the small amount of density found at the particular BCPs.

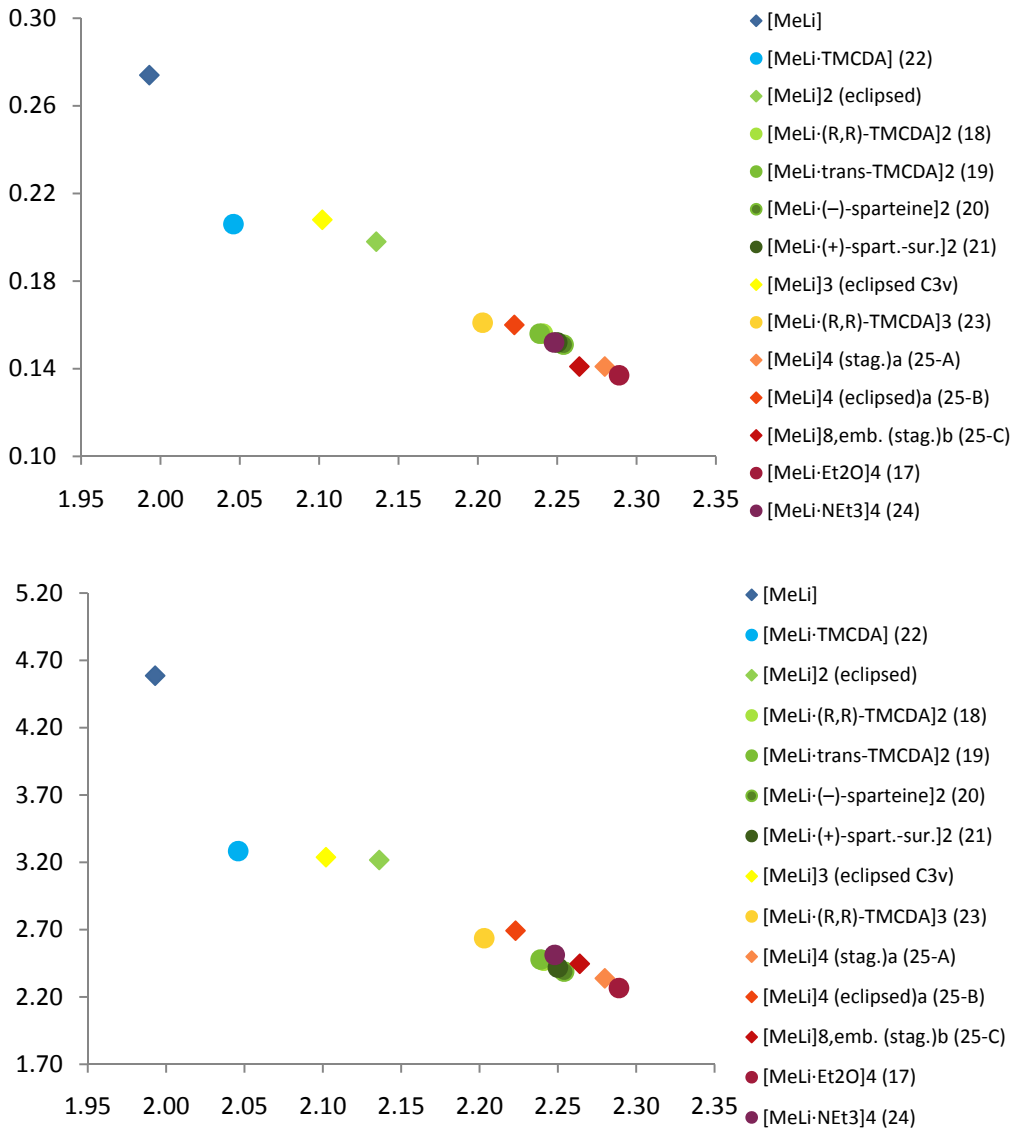

Figure 12.4. Correlation between BCP properties $\rho(\mathbf{r}_{BCP})$ [eÅ^{-3}], $\nabla^2\rho(\mathbf{r}_{BCP})$ [eÅ^{-5}] and bond path length *d* [Å]; ♦ denotes isolated clusters, • refers to Lewis base adducts; blue symbols refer to monomers, green to dimers, yellow/orange icons mark trimers and red signs denote tetramers.

Within the series of isolated and base coordinated MeLi clusters, the lowest BCP density values are observed for the tetrameric entities (**17**: 0.137 eÅ^{-3}), while the highest amount of density is detected at the BCP of the isolated monomer (0.274 eÅ^{-3}).

Interestingly, the Laplacian behavior runs parallel, with the most positive value exhibited by the isolated monomer (4.586 eÅ^{-5}) and the lowest one found for the ether-coordinated tetramer (2.266 eÅ^{-5}). In Figure 13.4 the BCP density and Laplacian values of all studied organolithium compounds are plotted *versus* the bond path lengths *d*, respectively. From the distribution of points an almost linear dependency of $\rho(\mathbf{r}_{BCP})$ and $\nabla^2\rho(\mathbf{r}_{BCP})$ values on *d* may be suggested, with high density and Laplacian values corresponding to the shortest bond path lengths. Thus, in agreement with chemical intuition, the shortest bonds (*d*) correspond to the strongest interactions in terms of comparably high $\rho(\mathbf{r}_{BCP})$ and $\nabla^2\rho(\mathbf{r}_{BCP})$ values, the latter indicating a pronounced electrostatic attraction.

12.3.2 Polarity Changes upon Deaggregation and Lewis Base Coordination

For the evaluation of polarity changes within QTAIM, the bond path lengths and ratios offer first insight, since they are directly related to an increase or decrease of charge density within the corresponding atomic basins. Regarding the total bond path lengths (see Table 12.3, also Figure 12.4), *d* is considerably shortened going from tetrameric to monomeric entities (e.g. $[MeLi]_{4,st.}$: 2.280 Å to [MeLi]: 1.993 Å; $[MeLi{\cdot}NEt_3]_4$: 2.248 Å to [MeLi·TMCDA]: 2.046 Å). However, the contraction affects both bonding partners, and thus the ratio d_1(Li–BCP)/d_2(C–BCP) of the individual bond path lengths does not indicate any polarity increase upon deaggregation. The lowest d_1/d_2 ratio corresponds to the most polarized situation and is detected for the isolated staggered tetramer (0.537), while the monomeric entity features a more even charge distribution along the bond path (0.555). Hence, with exception of the trimeric structures, the d_1/d_2 ratio actually increases upon deaggregation, thus indicating a polarity decrease. Furthermore, comparing the isolated clusters to their Lewis base adducts, the Li–C bond polarity is in most cases increased upon base coordination with exception of the isolated staggered tetramer and the monomeric structures of equal d_1/d_2 values.

A more detailed view of polarity changes can be gained from the investigation of the individual BCP properties. Since $\nabla^2\rho$ is directly related to the kinetic and potential energy values at a given point *via* the Virial Theorem (Chapter 3.1), positive Laplacian values refer to an excess of potential energy. In view of bond polarity changes, increasingly positive $\nabla^2\rho$ values may thus be interpreted as enhancement of electrostatic attraction. As discussed in the preceding chapter (12.3.1), the most positive Laplacian

values are observed for the monomeric structures. However, no constant decrease is detected upon aggregation (see also Figure 12.3). For instance dimeric and tetrameric structures feature Laplacian values, which are fairly comparable in magnitude (e.g. **24**: 2.512 eÅ^{-5} to **19**: 2.478 eÅ^{-5}). In contradiction to the d_1/d_2 values, a decrease of the electrostatic influence is observed upon base coordination, with the more positive $\nabla^2\rho$ observed for the isolated clusters compared to the base adducts (see Table 12.3).

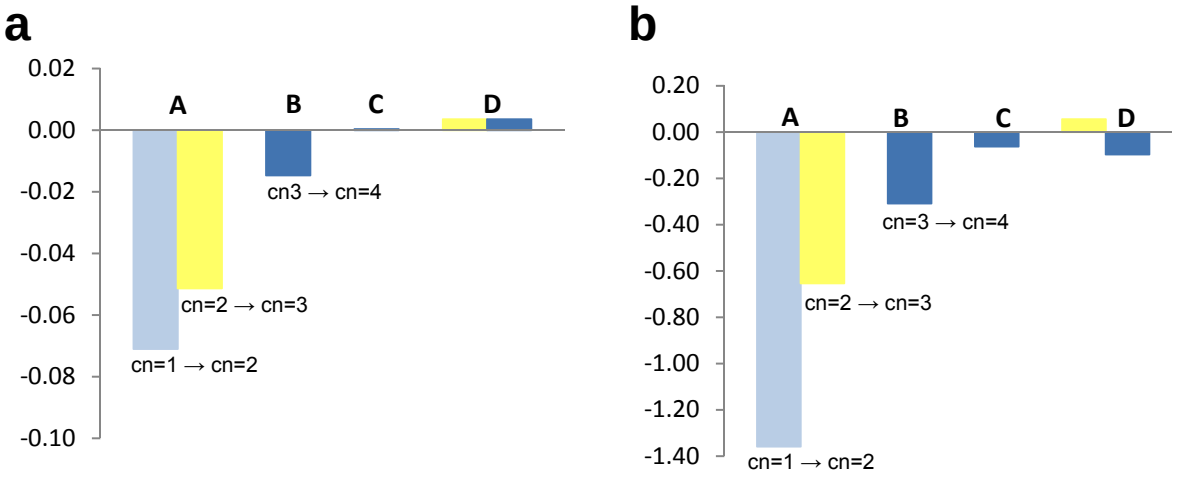

Figure 12.5. Representation of the incremental changes in a) ρ [eÅ^{-3}] and b) $\nabla^2\rho$ [eÅ^{-5}] upon increased Li coordination numbers (cn). Light blue denotes an increase from cn=1 to cn=2, yellow from cn=2 to cn=3 and dark blue represents an increase from cn=3 to cn=4. On the x-axes the accrued type of interaction is denoted: **A**) corresponds to an additional Li–C interaction, **B**) depicts one further dative oxygen coordination, **C**) stands for a nitrogen coordination equivalent to **B** and **D**) summarizes the replacements of one strong Li–C interaction by two dative Li–N coordination sites in chelate ligand system.

Since no dependency of the BCP properties on the aggregation state was observed, the influence of the overall Li coordination number on the QTAIM properties was investigated. Regarding the presented series of complexes, the Li coordination number can be increased *via* i) an additional electrostatic interaction in a higher aggregated MeLi cluster, ii) the coordination of a monodentate nitrogen or oxygen base (**24** or **17**, respectively) or iii) the replacement of one strong Li–C interaction by two dative Li–N coordination sites in chelate ligand systems (**18**-**23**). In Figure 12.5 the incremental changes in ρ and $\nabla^2\rho$ are summarized and graphically depicted. First of all, the observed changes are more pronounced for a coordination number increase from 1→2 than for the higher equivalents (see e.g. section **A** in Figure 12.5). Since organolithium

compounds favor high coordination numbers (cn) with a minimum of three neighbors for the Li atom, the more distinct changes observed for cn=1 to cn=2 are in line with chemical expectations.

Furthermore, the magnitude of divergences in ρ and $\nabla^2\rho$ are decreased from **A** to **C**. In this context, **A** denotes an additional coordination site that bonds via a strong and electrostatic interaction. In contrast to **A**, **B** and **C** correspond to a dative coordination, with **B** being the more polar one due to the higher electronegativity of oxygen compared to nitrogen. Hence, the magnitude of changes within the BCP properties also depends on the strength of the augmented coordination site.

Concomitantly to the QTAIM studies, NPA charges have been calculated (see Table 12.2). The divergence from electroneutrality for some compounds can be ascribed to the employed averaging procedure. In addition, the ECPs incooperated in the PEECM optimization are most probably responsible for the residual charge obtained for **25-B**. From the distribution of yielded values, no dependency of Li and C charges on the aggregation degree can be observed. However, in contradiction to common belief,[7] the lowest charges are actually exhibited by the monomeric structures ([MeLi]: (Li) 0.830 e and (C) –1.425 e), while dimers and tetramers feature equally high charges (e.g. $[MeLi]_2$: (Li) 0.867 e and (C) –1.489 e; **25-A**: (Li) 0.850 e and (C) –1.510 e). Furthermore, with exception of the C charges found for the trimeric structures, isolated clusters exhibit in general the higher charges compared to their Lewis base adducts. Hence, within the NPA scheme polarity is decreased upon base complexation. Comparing the tetrameric N- and O-ligand systems, the more electronegative oxygen base in **17** favors a more ionic charge distribution in the inner MeLi unit (Li: 0.824 e; C: –1.446 e) compared to the NEt_3-complexed **24** (Li: 0.817 e; C: –1.412 e). This may be interpreted in terms of an increasingly polarized or ionic surrounding in the O-coordinated system **17**, which enhances in return the polarity within the inner MeLi moiety. This can also be observed comparing models **25-A** to **C**, of which the point charge embedded cluster **25-C** exhibits the most ionic charge distribution.

In summary, neither from QTAIM nor NPA studies was an increase of bond polarity upon deaggregation observed. The tendencies in polarity and charge variances were erratic and no distinct dependency on the aggregation state could be observed. Similar results have already been discussed for the isolated systems $[MeLi]_n$ (n=1-4) in

earlier studies,[27] however, the influence of base coordination was omitted therein. From the results presented *vide supra*, a significant impact of the surrounding Lewis base upon the electronic structure of the inner MeLi entity becomes obvious, especially in view of the connatural systems **17** and **24**. This is particularly important in view of the compounds which are actually employed within synthesis, since they are exclusively base-coordinated. In any case, regarding the series of N-complexed systems **18**-**21** and **24**, no coherence between aggregation degree and charge distribution is detected. Thus an increase of bond polarity upon deaggregation may no longer be adduced to account for the predominantly enhanced reactivity of MeLi units with lower aggregation degree. Presumably, this perception can be extended to other RLi systems and other motives have to be investigated to explain the structure-reactivity relationship of MeLi and congener systems. *Collum et al*. have already discussed in extensive thermodynamic and kinetic studies,[28-30] that the factors influencing structure and reactivity of lithiumorganic compounds may be by far more complicated than commonly assumed. Furthermore, they have demonstrated that a lowering of the aggregation degree may not always be the explanation for the observed reactivity and that higher aggregates may additionally be able to perform without an initial decomposition to monomers.

12.4 Conclusions

In the preceding chapter, a detailed computational study on methyllithium in various aggregation degrees and its corresponding Lewis base adducts has been presented, in an attempt to investigate the changes in the electronic structure upon deaggregation and base coordination. Based on the experimental data obtained for the tetrameric and dimeric structures **17**-**21**, a complementary series of $[MeLi]_n$ (n=1-4) isolated clusters and corresponding base adducts (TMCDA, sparteine, Et_2O and NEt_3) have been evolved. To scrutinize the fine details of electronic structure alternation, QTAIM, NPA and NLMO analyses have been accomplished.

In a first step, efficient and sufficiently accurate modeling techniques have been tested to yield the correct solid-state configuration of the individual MeLi clusters. Through application of PCM and PEECM embedding techniques, the structural data of pure and coordinated MeLi compounds has been modeled within sufficient accuracy,

especially with respect to the conformational changeover from eclipsed to staggered arrangements for gas-phase and solid-state $[MeLi]_4$, respectively. All Lewis base-coordinated compounds were obtained in good agreement with the experimental data.

Due to the close Li···H contacts observed for all studied compounds, agostic interactions have been investigated employing NPA charges and NLMO analysis. Although an energetic difference of 9.546 kJ/mol has been observed for the isolated eclipsed and staggered tetramers (**25-A** and **25-B**), the results were less conclusive for the couples of corresponding dimers with staggered and eclipsed configuration. Hence, agostic interactions definitely play a role in stabilizing the individual conformations, but are only one of a number of features influencing the overall structure formation.

Within the electronic structure analysis, all examined Li–C bonds were characterized as strongly polarized, featuring low $\rho(\mathbf{r}_{BCP})$ and positive $\nabla^2\rho(\mathbf{r}_{BCP})$ values typical for metal–element interactions. A quasi-linear dependency was suggested between $\rho(\mathbf{r}_{BCP})$ and $\nabla^2\rho(\mathbf{r}_{BCP})$ and the bond path length *d*. For the evaluation of polarity changes upon deaggregation, bond path ratios d_1/d_2, $\nabla^2\rho(\mathbf{r}_{BCP})$ values and NPA charges have been taken into account. However, no increase of Li–C bond polarity during deaggregation of isolated and base coordinated clusters was observed, either from QTAIM or NPA results. Hence, an enhancement of bond polarity may no longer be offered as explanation for the significantly enhanced reactivity of MeLi entities of lower aggregation degree. However, a dependency of the incremental changes within the BCP properties on the Li coordination number and the type of additional coordination site was presented. With respect to the interaction strength of the additional coordination site, the divergence within $\rho(\mathbf{r}_{BCP})$ and $\nabla^2\rho(\mathbf{r}_{BCP})$ became more pronounced in magnitude.

Furthermore, the influence of base coordination upon the electronic structure has been discussed. Particularly the NPA charges suggest a decrease of the overall polarity due to base complexation. Comparing O- and N-bases, the more electronegative ligand system in **17** favors a more ionic charge distribution compared to **24**. Electronic (and presumably also steric) properties of the solvent molecule or coordinating base modify the strength and nature of the encapsulated Li–C entity.

In summary, a broad overview of structural and electronic features within isolated MeLi clusters and their Lewis base-coordinated adducts has been presented in this chapter, taking agostic interactions and electronic structure alternations upon cluster size

modification into account. However, no straightforward guideline for the structure-reactivity relationship of organolithiums in general, and specifically MeLi, could be derived. This suggests a complex connection between fine structural details (also taking steric influences into account), charge distribution and thus bonding and the reactivity and activity of the actual organothlium reactand.

PART IV

Summary

Deutsche Zusammenfassung

Summary

Within this thesis, the analysis and hence the better comprehension of the chemical bond within metal–element compounds is the central topic. By use of various DFT methods a selection of M–E interactions have been modeled and analyzed *via* Bader's QTAIM, the ELF and NBO techniques. Special focus was set on a series of transition metal borylene and carbene complexes, and the Li–C bonds as representatives for main group organometallics. Therefore, this thesis is split into three parts:

(I) An introduction reviewing the quantum chemical machinery as well as the analysis tools applied for the evaluation of chemical bonds.

(II) Within the second part the chemical interactions taking place in transition metal complexes are studied focusing on borylenes and cognate carbenes.

(III) In Part III, a broad overview of the appropriate modeling and nature of the Li–C bond as well as intermolecular interactions in methyllithium is provided.

Part I: Introduction and Theoretical Background

Within the introductory part of this thesis the basic formalism, applicability and shortcomings of the herein applied quantum chemical methods are presented. Density functional theory is introduced, since it is the underlying technique to obtain the molecular charge density that can be evaluated by bond analysis tools afterwards. Bader's QTAIM and the electron localization functions and the electron localizability indicator are presented as they have been broadly applied within this thesis for bonding analysis.

Part II: Chemical Bonding in Transition Metal Compounds

In the second part a detailed study of *d*-block metal–metal and metal–ligand interactions by means of ELF and QTAIM analysis was presented. In particular, bridged borylene and carbene transition metal complexes were investigated with emphasis on the specific binding state of the bridging ligand and the absence/occurrence of a direct metal–metal interaction. Already from the overview about M–M interactions given in Chapter 5, the divergence between chemical intuition and the actual detection of a direct metal–metal interaction became apparent. Although the formal electron counting preserves the image of a direct metal–metal bond in many dinuclear complexes, the direct interaction can be suppressed by a through-bond mechanism depending on conformation and nature of the bridging ligand. With reference to a series of diiron complexes, the boundary conditions for the occurrence or absence of a metal–metal bond path or ELF attractor were studied. Additionally, molecular orbitals were discussed and the interplay between ligand donation and metal back-donation was investigated by means of NPA charges. In summary, the features indicating a direct M–M bond are suppressed, if the structural arrangement and the total binding strength (σ-acceptor and π-donor capabilities) of the bridging ligand ensure the effective M···M interaction *via* the bridge.

In the subsequent chapter (Chapter 6), the singlet and triplet states of carbenes and borylenes were investigated to explain the varying topological features observed for both kinds of ligands depending on the particular bonding partners. In analogy to the

Fischer/Schrock concept, the bonding patterns observed for carbenes were transcribed to borylenes and first results on terminal complexes have been presented. Based on these findings, the possible characteristics of "Schrock"-type borylene complexes were illustrated. However, the limits of QTAIM and ELF analysis were unveiled in the discrepancies between both methods and requirements for refined techniques in bonding analysis became perceivable.

The shortcomings of density functionals with respect to bonding analysis are investigated in Chapter 7. For a series of borylene, vinylidene and carbene bridged dimanganese complexes a striking qualitative dependency of QTAIM and ELF results on the amount of exact exchange in the employed density functional was observed. Only for the methylene supported complex a univocal bonding situation at the bridging atom was detected. All other complexes featured a dependency of VSCC synapticity and ELF attractors on the amount of Hatree-Fock exchange incorporated in the density functional. Comparing boron and carbon bridgeheads, the main differences are found in the net charge transfer *from* the bridge towards the metal centers in the two borylene complexes in contradiction to the charge transfer *to* the bridge in the carbon bridged complexes. Furthermore, for all supported complexes the absence of a direct metal–metal bond could be confirmed, which was especially remarkable for the prototype "dimetalla-cyclopropane" in the methylene complex. Thus, all bridging ligands were classified as good-to-excellent π-acceptors towards the metal fragments, enabling a through-bond mechanism *via* the bridge and preventing a direct Mn–Mn interaction.

In Chapter 8, a survey of bonding patterns in borylene-bridged cobalt, nickel and the previously discussed manganese complexes was given and the individual QTAIM properties were compared. The topological features around the supporting boron atom in the dinickel complex were interpreted as those of a delocalized borylene bridge, whereas the cobalt and manganese species were more consistent with a dimetalla-substituted borane. Presumably, the varying topologies of borylenes can be linked to the spin – and hence binding – state of the bridging boron atom, which may be influenced by the nature and oxidation state of the bonding partners. This seems to be closely related to the extension of the Fischer/Schrock concept from carbenes to borylenes that has been targeted in Chapter 6. However, additional experimental data is necessary for the further evaluation of "Schrock"-type borylenes. It should be noted that promising attempts have already been undertaken, however, no crystal structure has been obtained.

Part III: Main Group Metals: Li–C Bonding and Intermolecular Interactions in Methyllithium

In Part III an extensive study on metal–element interactions in methyllithium and their appropriate modeling has been presented. Within the scope of this investigation, the understanding of the electronic constitution and the relationship between structure and reactivity was of particular interest with special focus on:

- The efficient and sufficiently accurate modeling of environmental effects *via* embedding approaches in comparison to full solid state calculations.

- The correct structure evolvement by means of embedding techniques, especially in view of the conformational changeover observed for eclipsed and staggered methyllithium in the gas-phase and solid state, respectively.

- The alterations within the electronic structure upon base coordination and deaggregation.

In the introductory Chapter (9) an overview of structure forming principles and prevalent bonding concepts in organolithium compounds was presented. In particular the formation of aggregates and oligomeric structures with often complex three-dimensional distention was discussed. Based on the introduced structure characteristics of lithiumorganics, the demand for modeling techniques, which explicitly or approximately take the surroundings into account, was illustrated.

Thus, in the subsequent Chapter (10) the basic principles of solid state modeling as well as embedding techniques were described. Of the many possibilities to bridge the gap between pure gas-phase and full solid state calculations the polarizable continuum models (PCM) and the recently proposed periodic electrostatic embedded cluster model (PEECM) have been selected and reviewed.

Based on the techniques introduced beforehand, Chapter 11 focuses on the evaluation of embedding approaches for modeling environmental effects on charge density parameters in comparison with full solid state and isolated gas-phase calculations. In detail, the charge density and its Laplacian at the Li–C and C–H bond critical points as

well as other features of the electron density distribution (such as AIM charges and bond path ratios) of the methyl lithium crystal have been compared by density functional methods for i) the isolated $(LiCH_3)_4$ tetramer or larger clusters, ii) for quantum-mechanically treated clusters in polarizable continuum model (PCM) surroundings, iii) for clusters augmented by the periodic electrostatic embedded cluster model (PEECM), and for iv) the full periodic crystal. Comparisons with identical functional and basis sets indicated that the simple PCM approach alone did not provide a good representation of the crystal environmental effects on the charge density parameters. Instead PEECM gave a more faithful picture. Effects of basis set and exchange-correlation functional were of a comparable order of magnitude as the crystal environmental effects. In this context, embedded-cluster computations provided distinct advantages over explicit solid-state calculations with respect to their freedom of the choice of computational and theoretical level.

In Chapter 12, a detailed computational study on methyllithium $[MeLi]_n$ in various aggregation degrees n = 1-4 and a selection of corresponding Lewis base adducts has been presented to investigate the changes in the electronic structure upon deaggregation and base coordination. Arising from the experimental data obtained for tetrameric and dimeric Lewis base adducts, a complementary series of $[MeLi]_n$ (n = 1-4) isolated clusters and corresponding coordination compounds (with TMCDA, sparteine, Et_2O and NEt_3) have been evolved and studied by means of QTAIM, NBO and NLMO analysis. Through application of embedding techniques (evaluated in Chapter 11) the correct solid state configuration of the individual MeLi clusters was obtained *via* structure optimization. In addition, weak interactions such as agostic Li···H contacts have been investigated based on NBO charges and NLMO analysis. Differences between the interaction energies of eclipsed and staggered methyl hydrogens in the isolated tetramers were observed. However, they have been too small for a clear assignment of agostic interactions being responsible for the conformational discrepancies. Within the electronic structure analysis, all examined Li–C bonds were characterized as strongly polarized, featuring typical $\rho(\mathbf{r}_{BCP})$ and $\nabla^2\rho(\mathbf{r}_{BCP})$ values for metal–element interactions. A quasi-linear dependency was suggested between $\rho(\mathbf{r}_{BCP})$ and $\nabla^2\rho(\mathbf{r}_{BCP})$, and the bond path length *d*. For the evaluation of polarity changes upon deaggregation, bond path ratios d_1/d_2, $\nabla^2\rho(\mathbf{r}_{BCP})$ values and NBO charges have been taken into account. However, no increase of Li–C bond polarity during deaggregation of isolated and base-coordinated

clusters was observed, neither from QTAIM nor NBO results. Nevertheless, a dependency of the incremental changes within the BCP properties on the Li coordination number and the type of additional coordination site was presented. Furthermore, the influence of base coordination upon the electronic structure has been discussed. In particular the NBO charges suggested a decrease of the overall polarity due to base complexation. Comparing O- and N-donor bases, the more electronegative oxygen atom in Et_2O favored a more ionic charge distribution compared to the NEt_3 complexed analogue. In summary, electronic (and presumably also steric) properties of the solvent molecule or coordinating base modify the strength and nature of the encapsulated Li–C bond.

The scope of the thesis was the better understanding of the chemical bond as an elementary concept within chemistry. Special focus has been set on metal–(main-group)element interactions since they determine the chemical behavior of a complete section of chemistry: organometallics. A very broad survey and detailed insight into the technical modeling and chemical nature of a selection of M–E bonds could be gained, offering guidance for the classification and chemical applicability of the investigated compounds.

Zusammenfassung

Im Zentrum dieser Arbeit stand die Analyse von Metall–Element Wechselwirkungen, um ein tieferes Verständnis der chemischen Bindung zu erlangen. Unter Verwendung verschiedener DFT Methoden wurde eine Serie von M–E Bindungen modelliert und anschließend mittels Baders QTAIM, der ELF und dem NBO Ansatz analysiert. Im Fokus standen hierbei besonders Borylen und Carben Komplexe, sowie die Li–C Bindung stellvertretend für Organometallverbindungen der Hauptgruppen. Folglich gliederte sich die vorliegende Arbeit sich in drei Teile:

(I) In einem einführenden Kapitel wurden die quantenchemischen Methoden sowie die verwendeten Techniken zur Bindungsanalyse vorgestellt.

(II) Innerhalb des zweiten Teils wurden chemische Wechselwirkungen in Übergangsmetallkomplexen untersucht, im Besonderen in Borylen und gleichartigen Carben Verbindungen.

(III) Teil III bot einen weitgefächerten Überblick über Modellierung und Natur der Li–C Bindung sowie der intermolekularen Wechselwirkungen in Methyllithium als Beispielverbindung.

Part I: Einführung und Theoretischer Hintergrund

Innerhalb des einleitenden Kapitels dieser Arbeit wurden die Grundlagen, Anwendbarkeit und Mängel der verwendeten theoretischen Methoden zusammengefasst. Die Dichtefunktionaltheorie wurde als elementares Werkzeug eingeführt, die zur Modellierung der anschließend zu analysierenden Ladungsdichteverteilung verwendet wurde. Baders QTAIM, sowie die Elektronenlokalisierungsfunktion und der Elektronenlokalisierbarkeitsindikator wurden vorgestellt, da diese vielfach zur Bindungsanalyse innerhalb dieser Arbeit angewendet wurden.

Part II: Die Chemische Bindung in Übergansmetallverbindungen

Im zweiten Teil der Arbeit wurde eine detaillierte Studie von Metall–Metall sowie Metall–Ligand Wechselwirkungen der Übergangsmetalle präsentiert. Im Besonderen Borylene und Carbene wurden hierbei untersucht mit Betonung auf dem jeweiligen Spinzustand des verbrückenden Liganden und der Anwesenheit/Abwesenheit einer direkten Metall–Metall Wechselwirkung. Bereits anhand des Überblicks in Kapitel 5 ließ sich die Divergenz zwischen chemischer Intuition und dem tatsächlichen Nachweisen einer direkten Metall–Metall Bindung erkennen. Obwohl die 18-Elektronen-Regel die Existenz einer direkten M–M Bindung in vielen zweikernigen Übergansmetallkomplexen vorhersagt, kann diese durch einen Brückentransfer-Mechanismus („through-bond mechanism“) unterdrückt werden in Abhängigkeit von Konformation und Natur des Brückenliganden. Anhand einer Auswahl von zweikernigen Eisenkomplexen wurden die Randbedingungen für die Detektion eines Metall–Metall Bindungspfades oder entsprechender ELF Attraktoren untersucht. Zudem wurden Molekülorbitale heran-gezogen und das Wechselspiel zwischen Ligandenbindung und Metallrückbindung mittels NPA Ladungen untersucht. Zusammenfassend werden die Indikatoren einer direkten Metall–Metall Bindung stets dann unterdrückt, wenn die strukturelle Anordnung sowie die gesamte Bindungsstärke (im Sinne von σ-Akzeptoren und π-Donoren) des

Brückenliganden eine ausreichende Wechselwirkungen der Metall-Atome über das Brückenatom erlauben.

Im anschließenden Kapitel 6 wurden die Singlett und Triplett Zustände freier und gebundener Carbene und Borylene untersucht, um die unterschiedlichen topologischen Charakteristika beider Ligandensysteme in Abhängigkeit von ihren Bindungspartner zu erklären. In Analogie zum Fischer/Schrock Konzept, wurden die Besonderheiten innerhalb der chemischen Bindungen der Carbene auf Borylene übertragen und erste Ergebnisse des erweiterten Konzepts präsentiert. Hierauf basierend, wurden die möglichen Eigenschaften der „Schrock"-artigen Borylene diskutiert. Die Mängel innerhalb der QTAIM und ELF Theorien wurden jedoch im weiteren Verlauf erkenntlich, da sich für einen Teil der untersuchten Verbindungen kein eindeutiges Ergebnis bezüglich der ELF und QTAIM Analyse erhalten ließ. Die Notwendigkeit einer Verfeinerung der Analysewerkzeuge wurde hieraus deutlich ersichtbar.

Kapitel 7 befasste sich ausführlich mit den Unzulänglichkeiten der Dichtefunktionaltheorie im Hinblick auf die Analyse chemischer Bindungen. Innerhalb einer Reihe von Borylene, Vinyliden und Carben Komplexen wurde eine unvermutete Abhängigkeit der QTAIM und ELF Ergebnisse vom Anteil an exaktem Austausch im verwendeten Funktional beobachtet. Lediglich für das Methylen-verbrückte System wurde ein einheitliches Ergebnis bezüglich der M–E Bindungsklassifizierung gefunden. Alle übrigen Komplexe zeigten eine Korrelation der Anzahl an beobachteten VSCCs und ELF Attraktoren vom Anteil an Hartree-Fock Austausch innerhalb des Dichtefunktionals. Verglich man Bor und Kohlenstoff in ihren Eigenschaften als Brückenatome, so fanden sich die Hauptunterschiede im Transfer an Netzladung. Während die Borylene Ladung von der Brücke weg zu den Metallzentren transferierten, fand in den Carben-verbrückten Spezies der umgekehrte Vorgang statt. Darüber hinaus wurde für keine der verbrückten Komplexe eine direkte Metall–Metall Bindung beobachtet. Dies ist besonders im Hinblick auf den Methylenkomplex bemerkenswert, da dieser als Prototyp des Dimetallazyklopropans galt. Somit wurden alle verbrückenden Liganden als gute oder exzellent π-Akzeptoren klassifiziert, die eine Wechselwirkung der Metallatome via Brückenatom begünstigen und eine direkte M–M Bindung unterdrücken.

In Kapitel 8 wurde eine Übersicht über Borylene-verbrückte Kobalt- und Nickelkomplexe gegeben unter Einbeziehung der zuvor diskutierten analogen

Manganspezies. Die topologischen Eigenschaften des Brückenboratoms im zweikernigen Nickelkomplex wiesen auf eine delokalisierte Wechselwirkung hin. Im Gegensatz hierzu zeigte die zweikernige Kobaltspezies Charakteristika, die eher einem dimetalla-substituierten Boran entsprachen. Diese Unterschiede lassen sich vermutlich auf einen andersartigen Spinzustand des Boratoms zurückführen, welcher durch Natur und Oxidationsstufe des Bindungspartners beeinflusst wird. Dies steht in engem Zusammenhang mit der in Kapitel 6 diskutierten Übertragung des Fischer/Schrock Konzepts von Carbenen zu Borylenen. Es werden jedoch zusätzliche experimentelle Struktur- und Reaktivitätsdaten benötigt, um eine grundlegendere Evaluierung dieses erweiterten Konzeptes zu ermöglichen. An dieser Stelle soll jedoch angemerkt werden, dass bereits vielversprechende Versuche unternommen wurden, die bislang jedoch nicht durch den Erhalt einer Kristallstruktur verifiziert werden konnten.

Part III: Hauptgruppenmetalle: die Li–C Bindung sowie intermolekulare Wechselwirkungen in Methyllithium

Der dritte Teil dieser Arbeit enthielt eine ausführliche Studie über Metall–Elementbindungen in Methyllithium und ihre angemessene quantenchemische Modellierung. Ziel dieser Untersuchungen war es, den elektronischen Aufbau sowie den Zusammenhang zwischen Struktur und Reaktivität zu klären mit besonderem Fokus auf:

- Die effiziente und ausreichend akkurate Modellierung der Umgebungseffekte mittels Einbettungstechniken und ihre Evaluierung anhand expliziten Festphasenrechnungen.

- Der Erhalt der korrekten Struktur, besonders im Hinblick auf den Konformationswechsel des Methyllithium in Fest- und Gasphase von ekliptisch nach gestaffelt.

- Die Abweichungen, die sich innerhalb der elektronischen Struktur durch Basen- Koordination oder Deaggregation ergeben.

Im einleitenden Kapitel 9 wurde eine Übersicht der strukturbildenden Prinzipen und gängige Bindungskonzepte gegeben. Im Besonderen die Ausbildung von Aggregaten

und oligomeren Strukturen mit häufig weitläufiger dreidimensionaler Ausdehnung wurde hierbei diskutiert. Anhand der aufgeführten Strukturcharakteristika der Lithiumorganyle wurde die Notwendigkeit für besondere, Umgebungseffekte berücksichtigende Modellierungstechniken dargelegt.

Im anschließenden Kapitel 10 wurden deshalb die Grundlagen der Festphasenrechnung sowie verschiedene Einbettungstechniken diskutiert. Aus den vielen Möglichkeiten zur Überbrückung der Lücke zwischen reiner Gasphasenrechnung und expliziter Festphasenmodellierung wurden der PCM (polarizable continuum models) und das kürzlich vorgestellte PEECM Ansatz (periodic electrostatic embedded cluster model) herausgegriffen und eingeführt.

Basierend auf diesen Modellierungstechniken, stand die Evaluierung der Einbettungsverfahrung bezüglich ihrer Genauigkeit bei der Modellierung von Umgebungseffekten auf Ladungsdichteparameter im Zentrum von Kapitel 11. Im Detail wurden hierbei die Werte der Ladungsdichte selbst sowie des Laplace an den bindungskritschen Punkten der Li–C und C–H Bindungen sowie weitere Parameter (AIM Ladungen, Verhältnisse der Bindungspfadlängen) des Methyllithiumkristalles verglichen für i) das isolierter $(LiCH_3)_4$ Tetramer oder größere Cluster, ii) für Cluster modelliert innerhalb des PCM Ansatzes, iii) PEECM erweiterte Cluster und iv) die explizite Festphasenspezies. Der Vergleich bei identischem theoretischem Niveau ergab, dass die Modellierung innerhalb des PCM nicht ausreicht, um den Einfluss der Kristalleffekte auf die Ladungsdichteparameter wiederzugeben. Vielmehr konnte gezeigt werden, dass sich durch Verwendung des PEECM eine weitaus bessere Beschreibung der elektronischen Struktur erzielen lässt. Der Einfluss des Basisatzes sowie des Austausch-Korrelations-Funktionals waren jedoch in vergleichbarer Größenordnung wie die untersuchten Umgebungseffekte. In diesem Zusammenhang weisen die Einbettungsverfahrung jedoch große Vorteile gegenüber der Festphasenmodellierung auf, da sie eine größere Auswahl an theoretischen Verfahren unterstützen.

Kapitel 12 befasste sich mit der Untersuchung von Methyllithium $[MeLi]_n$ in verschiedenen Aggregatszuständen n = 1-4 und einer Auswahl von entsprechenden Lewisbasen-Addukten. Der Schwerpunkt lag hierbei auf der Analyse des Einflusses von Aggregationszustand und Koordination auf die elektronische Struktur der MeLi Einheit. Basierend auf experimentellen Daten, die für dimere und tetramere Lewisbasen Addukte

erhalten wurden, konnte eine vollständige Serie von $[MeLi]_n$ (n = 1-4) Clustern erstellt, die korrespondierenden Koordinationsverbindungen mit TMCDA, Spartein, Diethylether und Triethylamin erhalten und anhand von QTAIM, NBO und NLMO untersucht werden. Mittels der in Kapitel 11 evaluierten Einbettungstechniken wurde darüber hinaus die korrekte Festphasenkonformation der Methyleinheiten in der Strukturoptimierung erhalten. Zusätzlich wurden schwache Wechselwirkungen wie agostische Li···H Kontakte anhand von NBO Ladungen und des NLMO Ansatzes analysiert. Hierbei konnten Unterschiede in den Wechselwirkungsenergien für ekliptische und gestaffelte Wasserstoffatome festgestellt werden. Die Energiedifferenzen erwiesen sich jedoch als zu gering, um eine eindeutige Rückführung der jeweiligen Konformation auf bestimmte agostische Wechselwirkungen zu erlauben. Innerhalb der elektronischen Strukturanalyse, wurden alle untersuchten Li–C Bindungen als stark polarisiert klassifiziert und wiesen für Metall–Element Bindungen typischen $\rho(\mathbf{r}_{BCP})$ und $\nabla^2\rho(\mathbf{r}_{BCP})$ Werte auf. Eine quasi-lineare Abhängigkeit zwischen $\rho(\mathbf{r}_{BCP})$ bzw. $\nabla^2\rho(\mathbf{r}_{BCP})$ und der Länge *d* des Bindungspfades wurde aufgestellt. Zur Evaluierung der Polaritätsänderung, die mit einer Deaggregation einhergehen, wurden die Verhältnisse der Bindungspfade d_1/d_2, Elektronendichte und Laplace am bindungskritischen Punkt, sowie NBO Ladungen herangezogen. Es konnte jedoch keine Zunahme der Li–C Bindungspolarität aufgrund von Deaggregation festgestellt werden, weder innerhalb der QTAIM noch der NBO Ergebnisse. Allerdings wurde eine Abhängigkeit der Änderungen innerhalb der BCP Eigenschaften von der Koordinationszahl des Li Atoms sowie der Art der zusätzlichen Koordinationsstelle gefunden. Darüber hinaus wurde der Einfluss der Basenkoordination auf die elektronische Struktur diskutiert. Besonders die NBO Analyse wies auf eine Abnahme der Bindungspolarität durch Koordination hin. Verglich man O- und N-Donorbasen, so bevorzugte der elektronegativere Sauerstoffligand eine polarere Ladungsverteilung innerhalb des MeLi Einheit wie das NEt_3 komplexierte Equivalent. Zusammenfassend lässt sich folglich feststellen, dass die elektronische (und vermutlich auch sterische) Beschaffenheit des Solvent Moleküls bzw. der Lewisbase Stärke und Art der eingeschlossenen Li–C Bindung beeinflusst.

Wie einleitend erwähnt, lag der Schwerpunkt dieser Arbeit auf der Erlangung eines tieferen Verständnisses der chemischen Bindung als einem der elementarsten Konzepte der Chemie. Besonders wurden hierbei Metall–(Hauptgruppen)Element Wechselwirkungen untersucht, da sie das chemische Verhalten einer ganzen

Verbindungsklasse bestimmen: der Organometallchemie. Eine weit gefächerte Übersicht sowie Detailstudien zur technischen Modellierung und chemischen Natur einer Auswahl an M–E Bindungen konnte präsentiert werden, die eine Anleitung zur Klassifizierung und dem chemischen Anwendungspotential der untersuchten Verbindungen ermöglichte.

References

Chapter 1

[1] S. Shaik, *J. Comput. Chem.* **2007**, *28*, 51.
[2] R. Siegfried, *A History of Chemical Composition*, American Philosophical Society, Philadelphia, **2002**.
[3] G. N. Lewis, *J. Am. Chem. Soc.* **1916**, *38*, 762.
[4] I. Langmuir, *J. Am. Chem. Soc.* **1919**, *41*, 868.
[5] W. B. Jensen, *J. Chem. Ed.* **1984**, *61*, 191.
[6] L. Pauling, *The Nature of the Chemical Bond and the Structure of Molecules and Crystals – An Introduction to Modern Structural Chemistry*, Cornell University Press: Ithaca, New York, **1939, 1960**.
[7] W. Heitler and F. London, *Zeits. für Physik* **1927**, *44*, 455.
[8] F. London, *Zeits. für Physik* **1928**, *46*, 455.
[9] G. N. Lewis, *Trans. Faraday Soc.* **1923**, *19*, 450.
[10] G. Frenking and A. Krapp, *J. Comput. Chem.* **2007**, *28*, 15.
[11] C. Elschenbroich, *Organometallchemie*, B.G. Teubner, Wiesbaden, **2005**, p. 32-58.
[12] *Special Issue: 90 Years of Chemical Bonding; J. Comput. Chem. 28*, **2007**.
[13] M. P. Mitoraj, A. Michalak, T. Ziegler, *J. Chem. Theory and Comput.* **2009**, *5*, 962.
[14] J. P. Foster and F. Weinhold, *J. Am. Chem. Soc.* **1980**, *102*, 7211.
[15] A. E. Reed and P. v. R. Schleyer, *J. Am. Chem. Soc.* **1990**, *112*, 1434.
[16] A. E. Reed, R. B. Weinstock and F. Weinhold, *J. Chem. Phys.* **1985**, *83*, 735.
[17] A. E. Reed, L. A. Curtiss and F. Weinhold, *Chem. Rev.* **1998**, *88*, 899.
[18] R. W. F. Bader, *Atoms in Molecules: A Quantum Theory*, Oxford University Press, Oxford, **1990**.
[19] A. D. Becke and K. E. Edgecombe, *J. Chem. Phys.* **1990**, *92*, 5397.
[20] A. Savin, R. Nesper, S. Wengert and T. F. Fässler, *Angew. Chem. Int. Ed.* **1997**, *36*, 1808.
[21] A. Savin, *THEOCHEM* **2005**, *727*, 127.
[22] P.-O. Löwdin, *J. Chem. Phys.* **1950**, *18*, 365.
[23] R. S. Mulliken, *J. Chem. Phys.* **1955**, *23*, 1833.
[24] K. Kitaura and K. Morokuma, *Int. J. Quant. Chem.* **1976**, *10*, 325.
[25] T. Ziegler and A. Rauk, *Theor. Chim. Acta* **1977**, *46*, 1.
[26] T. Ziegler and A. Rauk, *Inorg. Chem.* **1979**, *18*, 1755.
[27] T. Ziegler and A. Rauk, *Inorg. Chem.* **1979**, *18*, 1558.
[28] K. Wiberg, *Tetrahedron* **1968**, *24*, 1093.
[29] M. S. Gopinathan and K. Jug, *Theoret. Chim. Acta* **1983**, *63*, 497.
[30] I. Mayer, *Chem. Phys. Lett.* **1984**, *97*, 270.
[31] J. Cioslowksi and S. T. Mixon, *J. Am. Chem. Soc.* **1991**, *113*, 4142.

Chapter 2

[1] E. Fermi, *Rend. Accad. Lincei* **1927**, *6*, 602.
[2] L. H. Thomas, *Proc. Camb. Phil. Soc.* **1927**, *23*, 542.
[3] J. C. Slater, *Phys. Rev.* **1951**, *81*, 385.
[4] P. Hohenberg, W. Kohn, *Phys. Rev. B* **1964**, *136*, 864.
[5] W. Kohn, L. J. Sham, *Phys. Rev. A* **1965**, *140*, 1133.
[6] A. Szabo, N. S. Ostlund, *Modern Quantum Chemistry*, Dover Publications Inc., Mineola, New York, **1996**.
[7] W. Koch, M. C. Holthausen, *A Chemist's Guide to Density Functional Theory, Second Edition*, Wiley-VCH, Weinheim, **2001**.
[8] R. G. Parr, W. Yang, *Density Functional Theory of Atoms and Molecules, Vol. 16*, Oxford Science Publications, New York, **1998**.
[9] P.-O. Löwdin, *Phys. Rev.* **1955**, *97*, 1474.
[10] P.-O. Löwdin, *Phys. Rev.* **1955**, *97*, 1490.
[11] P.-O. Löwdin, *Phys. Rev.* **1955**, *97*, 1509.
[12] E. J. Baerends, O. V. Gritsenko, *J. Phys. Chem. A* **1997**, *101*, 5383.
[13] R. McWeeny, *Faraday Discuss.* **2007**, *135*, 13.
[14] J. Harris, *Phys. Rev. A.* **1984**, *29*, 1648.
[15] O. V. Gritsenko, P. R. T. Schipper, E. J. Baerends, *J. Chem. Phys.* **1997**, *107*, 5007.
[16] S. J. Vosko, L. Wilk, M. Nusair, *Can. J. Phys.* **1980**, *58*, 1200.
[17] A. D. Becke, *Phys. Rev. A* **1988**, *38*, 3089.
[18] J. P. Perdew, J. A. Chevary, S. J. Vosko, *Phys. Rev. B* **1992**, *46*, 6671.
[19] J. P. Perdew, W. Yue, *Phys. Rev. B* **1986**, *33*, 8800.
[20] J. P. Perdew, K. Burke, M. Ernzerhof, *Phys. Rev. Lett.* **1996**, *77*, 3865.
[21] J. P. Perdew, *Phys. Rev. B* **1986**, *33*, 8822.
[22] C. Lee, W. Yang, R. G. Parr, *Phys. Rev. B: Condens. Matter* **1988**, *37*, 785.
[23] B. Miehlich, A. Savin, H. Stoll, H. Preuss, *Chem. Phys. Lett.* **1989**, *157*, 200.
[24] A. D. Becke, *J. Chem. Phys.* **1993**, *98*, 5648.
[25] F. G. Cruz, K.-C. Lam, K. Burke, *J. Phys. Chem. A* **1998**, *102*, 4911.
[26] H. Bahmann, A. Rodenberg, A. V. Arbuznikov, M. Kaupp, *J. Chem. Phys.* **2007**, *126*, 011103.
[27] M. Kaupp, H. Bahmann, A. V. Arbuznikov, *J. Chem. Phys.* **2007**, *127*, 194102.
[28] A. Görling, *J. Chem. Phys.* **2005**, *123*, 062203.
[29] K. Burke, J. Werschnick, E. K. U. Gross, *J. Chem. Phys.* **2005**, *123*, 062206.
[30] A. Dreuw, M. Head-Gordon, *Chem. Rev.* **2005**, *105*, 4009.
[31] E. H. Lieb, S. Oxford, *Int. J. Quantum. Chem.* **1981**, *19*, 427.
[32] A. J. Cohen, P. Mori-Sanchéz, W. Yang, *Science* **2008**, *321*, 792.
[33] A. D. Becke, *J. Chem. Phys.* **2003**, *119*, 2972.
[34] F. Neese, *Coord. Chem. Rev.* **2008**, *In Press,* doi:10.1016/j.ccr.2008.10.014.
[35] A. D. Becke, *J. Chem. Phys.* **2005**, *122*, 064101.
[36] P. Mori-Sanchéz, A. J. Cohen, W. Yang, *J. Chem. Phys.* **2006**, *124*, 091102.
[37] P. Mori-Sanchéz, A. J. Cohen, W. Yang, *J. Chem. Phys.* **2006**, *125*, 201102.

Chapter 3

[1] R. W. F. Bader, *Atoms in Molecules: A Quantum Theory*, Oxford University Press, Oxford, **1990**.
[2] R. W. F. Bader, *Chem. Rev.* **1991**, *91*, 893.
[3] C. F. Matta, R. W. F. Bader, *J. Phys. Chem. A* **2006**, *110*, 6365.
[4] R. W. F. Bader, *J. Phys. Chem. A* **2007**, *111*, 7966.
[5] A. Martín Pendás, E. Francisco, M. A. Blanco, C. Gatti, *Chem. Eur. J.* **2007**, *13*, 9362.
[6] C. Gatti, *Z. Kristallogr.* **2005**, *220*, 399.
[7] P. Macchi, A. Sironi, *Coord. Chem. Rev.* **2003**, *238-239*, 383.
[8] P. Coppens, A. Volkov, *Acta Crystallogr. A* **2004**, *60*, 357.
[9] D. Leusser, J. Henn, N. Kocher, B. Engels, D. Stalke, *J. Am. Chem. Soc.* **2004**, *126*, 1781.
[10] J. Overgaard, H. F. Clausen, J. A. Platts, B. B. Iversen, *J. Am. Chem. Soc.* **2008**, *130*, 3834.
[11] W. Scherer, G. Eickerling, D. Shorokhov, E. Gullo, S. G. McGrady, P. Sirsch, *New J. Chem.* **2006**, *30*, 309.
[12] A. Martín Pendás, A. Costales, V. Luaña, *Phys. Rev. B* **1997**, *55*, 4275.
[13] E. Cerpa, A. Krapp, A. Vela, G. Merino, *Chem. Eur. J.* **2008**, *14*, 10232.
[14] S. Grimme, C. Mück-Lichtenfeld, G. Erker, G. Kehr, H. Wang, H. Beckers, H. Willner, *Angew. Chem. Int. Ed.* **2009**, *48*, 1.
[15] A. Haaland, D. J. Shorokhov, N. V. Tverdova, *Chem. Eur. J.* **2004**, *10*, 4416.
[16] A. Haaland, D. J. Shorokhov, N. V. Tverdova, *Chem. Eur. J.* **2004**, *10*, 6210.
[17] J. Cioslowski, S. T. Mixon, *Can. J. Chem.* **1992**, *70*, 443.
[18] M. A. Blanco, A. Martín Pendás, E. Francisco, *J. Chem. Theory Comput.* **2005**, *1*, 1096.
[19] A. Martín Pendás, M. A. Blanco, E. Francisco, *J. Comput. Chem.* **2009**, *30*, 98.
[20] E. Francisco, A. Martín Pendás, M. A. Blanco, *J. Chem. Phys.* **2007**, *126*, 094102.
[21] A. Martín Pendás, E. Francisco, M. A. Blanco, *Phys. Chem. Chem. Phys.* **2007**, *9*, 1087.
[22] R. W. F. Bader, C. Gatti, *Chem. Phys. Lett.* **1998**, *287*, 233.
[23] C. Gatti, F. Cargnoni, L. Bertini, *J. Comput. Chem.* **2003**, *24*, 422.
[24] C. Gatti, D. Lasi, *Faraday Discuss.* **2007**, *135*, 55.
[25] C. Gatti, D. Lasi, *Faraday Discussion* **2007**, *135*, 55.
[26] P. Cassam-Chenaï, D. Jayatilaka, *Theor. Chem. Acc.* **2001**, *105*, 213.
[27] P. Cassam-Chenaï, D. Jayatilaka, *Theor. Chem. Acc.* **2002**, *107*, 383.
[28] L. Delle Site, *Theor. Chem. Acc.* **2002**, *107*, 378.
[29] R. W. F. Bader, *Theor. Chem. Acc.* **2002**, *107*, 381.
[30] E. S. Kryachko, *Theor. Chem. Acc.* **2002**, *107*, 375.
[31] J. R. Mohallem, *Theor. Chem. Acc.* **2002**, *107*, 372.
[32] J. Schwinger, *Phys. Rev.* **1951**, *82*, 914.
[33] G. K. H. Madsen, P. Blaha, K. Schwarz, *J. Chem. Phys.* **2002**, *117*, 8030.
[34] V. Luaña, P. Mori-Sanchéz, A. Costales, M. A. Blanco, *J. Chem. Phys.* **2003**, *119*, 6341.
[35] A. D. Becke, K. E. Edgecombe, *J. Chem. Phys.* **1990**, *92*, 5397.
[36] R. W. F. Bader, M. E. Stephens, *J. Am. Chem. Soc.* **1975**, *97*, 7391.
[37] A. Savin, *THEOCHEM* **2005**, *727*, 127.
[38] R. W. F. Bader, S. Johnson, T.-H. Tang, P. L. A. Popelier, *J. Phys. Chem.* **1996**, *100*, 15398.
[39] R. W. F. Bader, G. L. Head, *J. Chem. Phys.* **1999**, *111*, 8789.
[40] J. K. Burdett, T. A. McCormick, *J. Phys. Chem. A* **1998**, *102*, 6366.
[41] M. Kohout, A. Savin, *Int. J. Quant. Chem.* **1996**, *60*, 875.
[42] A. Savin, R. Nesper, S. Wengert, T. F. Fässler, *Angew. Chem. Int. Ed.* **1997**, *36*, 1808.

[43] J. Poater, M. Duran, M. Solà, B. Silvi, *Chem. Rev.* **2005**, *105*, 3911.
[44] E. Matito, B. Silvi, M. Duran, M. Solà, *J. Chem. Phys.* **2006**, *125*, 024301.
[45] M. Kohout, *Int. J. Quantum. Chem.* **2004**, *97*, 651.
[46] M. Kohout, K. Pernal, F. R. Wagner, Y. Grin, *Theor. Chem. Acc.* **2004**, *112*, 453.
[47] M. Kohout, K. Pernal, F. R. Wagner, Y. Grin, *Theor. Chem. Acc.* **2005**, *113*, 287.
[48] M. Kohout, F. R. Wagner, Y. Grin, *Theor. Chem. Acc.* **2008**, *119*, 413.
[49] M. Kohout, *Faraday Discuss.* **2007**, *135*, 43.
[50] F. R. Wagner, V. Bezugly, M. Kohout, Y. Grin, *Chem. Eur. J.* **2007**, *13*, 5724.
[51] F. R. Wagner, M. Kohout, Y. Grin, *J. Phys. Chem. A* **2008**, *112*, 9814.
[52] H. L. Schmider, A. D. Becke, *J. Chem. Phys.* **2002**, *116*, 3184.
[53] H. L. Schmider, A. D. Becke, *THEOCHEM* **2005**, *527*, 51.
[54] R. Ponec, D. L. Cooper, A. Savin, *Chem. Eur. J.* **2008**, *14*, 3338.
[55] J. J. McKinnon, A. S. Mitchell, M. A. Spackman, *Chem. Eur. J.* **1998**, *4*, 2136.
[56] J. J. McKinnon, D. Jayatilaka, M. A. Spackman, *Chem. Commun.* **2007**, 3814.
[57] M. A. Spackman, J. J. McKinnon, D. Jayatilaka, *Cryst. Eng. Comm.* **2008**, *10*, 377.
[58] F. Weinhold, *J. Chem. Edu.* **1999**, *76*, 1144.
[59] F. Weinhold, C. R. Landis, *J. Chem. Edu.* **2001**, *2*, 91.

Chapter 4

[1] F. Furche and J. P. Perdew, *J. Chem. Phys.* **2006**, *124*, 044103.
[2] M. Reiher, *Chimia* **2009**, *63*, 140.
[3] E. R. Davidson, *Chem. Rev.* **2000**, *100*, 351.
[4] R. J. Deeth, A. Anastasi, C. Diedrich and K. Randell, *Coord. Chem. Rev.* **2009**, *253*, 795.
[5] F. Neese, *Coord. Chem. Rev.* **2008**, *in Press,* doi:10.1016/j.ccr.2008.10.014.
[6] R. G. Parr and W. Yang, *Density Functional Theory of Atoms and Molecules*, Oxford Science Publications, New York, **1998**.
[7] T. Ziegler, *Chem. Rev.* **1991**, *91*, 651.
[8] T. R. Cundari, M. T. Benson, M. L. Lutz and M. O. Sommerer, *Rev. Comput. Chem.* **1996**, *8*, 63.
[9] L. Szasz, *Pseudopotential Theory of Atoms and Molecules*, J. Wiley & Sons, New York, **1986**.
[10] D. Figgen, A. Wedig, H. Stoll, M. Dolg, E. Eliav and U. Kaldor, *J. Chem. Phys.* **2008**, *128*, 024106.
[11] D. Figgen, K. A. Peterson and H. Stoll, *J. Chem. Phys.* **2008**, *128*, 034110.
[12] S. Faas, J. G. Snijders, J. H. van Lenthe, E. van Lenthe and E. J. Baerends, *Chem. Phys. Lett.* **1995**, *246*, 632.
[13] M. Reiher and J. Hinze in *Four-component ab initio Methods for Electronic Structure Calculations of Atoms, Molecules and Solids*, (Ed. B. A. Hess), Wiley, New York, **2003**, p. 61.
[14] G. Eickerling and M. Reiher, *J. Chem. Theory and Comput.* **2008**, *4*, 286.
[15] A. Savin, R. Nesper, S. Wengert and T. F. Fässler, *Angew. Chem. Int. Ed.* **1997**, *36*, 1808.
[16] M. Kohout *Die Elektronen-Lokalisierungs-Funktion und ionische Bindung*, Doktorarbeit, Universität Stuttgart, **1999**.
[17] M. Kohout and A. Savin, *Int. J. Quant. Chem.* **1996**, *60*, 875.
[18] M. Kohout and A. Savin, *Int. J. Quant. Chem.* **1997**, *18*, 1431.
[19] M. Kaupp, *J. Comput. Chem.* **2006**, *28*, 320.
[20] W. A. Herrmann, B. Reiter and H. Biersack, *J. Organomet. Chem.* **1975**, *97*, 245.

Chapter 5

[1] F. A. Cotton and G. Wilkinson, *Advanced Inorganic Chemistry*, Viley VCH, New York, **1988**.
[2] J. P. Collman, L. S. Hegedus, J. R. Norton and R. G. Finke, *Principles and Applications of Organotransition Metal Chemistry*, University Science Books, Mill Valley, **1987**.
[3] E. Hunstock, C. Mealli, M. J. Calhorda and J. Reinhold, *Inorg. Chem.* **1999**, *38*, 5053.
[4] A. Sironi, *Metal Clusters in Chemistry*, Wiley-VCH, New York, **1999**, p. 937-959.
[5] G. Frenking and N. Fröhlich, *Chem. Rev.* **2000**, *100*, 717.
[6] L. H. Gade, *Angew. Chem. Int. Ed.* **2000**, *39*, 2659.
[7] M. H. Powell and R. V. G. Ewens, *J. Chem. Soc.* **1939**, 286.
[8] L. F. Dahl and R. E. Rundle, *Acta Crystallogr.* **1963**, *16*, 419.
[9] M. Martin, B. Rees and A. Mitschler, *Acta Crystallogr.* **1982**, *B38*, 6.
[10] M. B. Hall, *Electron Distribution and Chemical Bonding*, Plenum Press, New York, **1982**, p. 205.
[11] D. A. Brown, W. J. Chambers, N. J. Fitzpatrick and R. M. Rawilson, *J. Chem. Soc. A* **1971**, 720.
[12] J. W. Lauher, M. Elian, R. H. Summerville and R. Hoffmann, *J. Am. Chem. Soc.* **1976**, *98*, 3219.
[13] R. Hoffmann and R. H. Summerville, *J. Am. Chem. Soc.* **1979**, *101*, 3821.
[14] P. Macchi, D. M. Prosperpio and A. Sironi, *J. Am. Chem. Soc.* **1998**, *120*, 13429.
[15] R. Bianchi, G. Gervasio and D. Marabello, *Chem. Commun.* **1998**, 1535.
[16] A. A. Low, K. L. Kunze, P. J. MacDougall and M. B. Hall, *Inorg. Chem.* **1991**, *30*, 1079.
[17] C. Bo, J.-P. Sarasa and J. M. Poblet, *J. Phys. Chem.* **1993**, *97*, 6362.
[18] M. Kaupp, *Chem. Ber.* **1996**, *129*, 527.
[19] F. A. Cotton and J. M. Troup, *J. Chem. Soc. Dalton Trans.* **1974**, *8*, 800.
[20] C. W. Bauschlicher Jr., *J. Chem. Phys.* **1986**, *84*, 872.
[21] C. Mealli and D. M. Prosperpio, *J. Organomet. Chem.* **1990**, *118*, 4631.
[22] J. Reinhold, E. Hunstock and C. Mealli, *New J. Chem.* **1994**, *18*, 465.
[23] J. Li and K. Jug, *Inorg. Chim. Acta* **1992**, *196*, 89.
[24] J. Reinhold, A. Barthel and C. Mealli, *Coord. Chem. Rev.* **2003**, *238-239*, 333.
[25] P. Macchi, L. Garlaschelli and A. Sironi, *J. Am. Chem. Soc.* **2002**, *124*, 14173.
[26] J. Windhager, M. Rudolph, S. Bräutigam, H. Görls and W. Weigand, *Eur. J. Inorg. Chem.* **2007**, 2748.
[27] H. Braunschweig and D. Rais, *Heteroatom Chem.* **2005**, *16*, 566.
[28] H. Braunschweig and M. Colling, *J. Organomet. Chem.* **2000**, *614-615*, 18.
[29] H. Braunschweig, K. Radacki, D. Rais, F. Seeler and K. Uttinger, *J. Am. Chem. Soc.* **2005**, *127*, 1386.
[30] H. Braunschweig, C. Burschka, M. Burzler, S. Metz and K. Radacki, *Angew. Chem. Int. Ed.* **2006**, *45*, 4352.
[31] H. Braunschweig, D. Rais and K. Uttinger, *Angew. Chem. Int. Ed.* **2005**, *44*, 3763.
[32] A. W. Ehlers, E. J. Baerends, F. M. Bickelhaupt and U. Radius, *Chem. Eur. J.* **1998**, *4*, 210.
[33] C. Lee, W. Yang and R. G. Parr, *Phys. Rev. B: Condens. Matter* **1988**, *37*, 785.
[34] B. Miehlich, A. Savin, H. Stoll and H. Preuss, *Chem. Phys. Lett.* **1989**, *157*, 200.
[35] A. D. Becke, *J. Chem. Phys.* **1993**, *98*, 5648.
[36] P. J. Stephens, F. J. Devlin, C. F. Chabalowski and M. J. Frisch, *J. Phys. Chem.* **1994**, *98*, 11623.
[37] A. Schäfer, C. Huber and R. Ahlrichs, *J. Chem. Phys.* **1994**, *100*, 5829.

[38] R. Ahlrichs, M. Bär, M. Häser, H. Horn and C. Kölmel, *Chem. Phys. Lett.* **1989**, *162*, 165.
[39] O. Treutler and R. Ahlrichs, *J. Chem. Phys.* **1995**, *102*, 346.
[40] M. v. Arnim and R. Ahlrichs, *J. Comput. Chem.* **1998**, *19*, 1746.
[41] A. D. Becke, *Phys. Rev. A* **1988**, *38*, 3098.
[42] J. P. Perdew, *Phys. Rev. B* **1986**, *33*, 8822.
[43] A. D. Becke, *J. Chem. Phys.* **1993**, *98*, 1372.
[44] F. Biegler-König and J. Schönbohm, *AIM2000, v2.0*, Bielefeld, Germany, **2002**.
[45] S. Noury, X. Krokidis, F. Fuster and B. Silvi, *ToPMoD Package*, Paris, **1997**.
[46] S. Noury, X. Krokidis, F. Fuster and B. Silvi, *Comput. Chem.* **1999**, *23*, 597.
[47] P. Macchi and A. Sironi, *Coord. Chem. Rev.* **2003**, *238*, 383.
[48] P. Macchi, D. M. Prosperpio and A. Sironi, *J. Am. Chem. Soc.* **1998**, *120*, 13429.
[49] G. Eickerling and M. Reiher, *J. Chem. Theory and Comput.* **2008**, *4*, 286.
[50] G. Eickerling, R. Mastalerz, V. Herz, W. Scherer, H.-J. Himmel and M. Reiher, *J. Chem. Theory and Comput.* **2007**, *3*, 2182.
[51] C. Gatti, *Z. Kristallogr.* **2005**, *220*, 399.
[52] D. Leusser, J. Henn, N. Kocher, B. Engels and D. Stalke, *J. Am. Chem. Soc.* **2004**, *126*, 1781.
[53] H. Braunschweig, C. Kollann and K. W. Klinkhammer, *Eur. J. Inorg. Chem.* **1999**, 1523.

Chapter 6

[1] H. Braunschweig, C. Kollann, D. Rais, *Angew. Chem. Int. Ed.* **2006**, *45*, 5254.
[2] C. E. Anderson, H. Braunschweig, R. D. Dewhurst, *Organometallics* **2008**, *27*, 6381.
[3] H. Braunschweig, C. Kollann, F. Seeler, *Struct. Bond.* **2008**, *130*, 1.
[4] A. W. Ehlers, E. J. Baerends, F. M. Bickelhaupt, U. Radius, *Chem. Eur. J.* **1998**, *4*, 210.
[5] F. M. Bickelhaupt, U. Radius, A. W. Ehlers, R. Hoffmann, *New J. Chem.* **1998**, *1*, 1.
[6] C. L. B. Macdonald, A. H. Cowley, *J. Am. Chem. Soc.* **1999**, *121*, 12113.
[7] J. Uddin, G. Frenking, *Organometallics* **2000**, *19*, 571.
[8] J. Uddin, G. Frenking, *J. Am. Chem. Soc.* **2001**, *123*, 1683.
[9] Y. Chen, G. Frenking, *J. Chem. Soc. Dalton Trans.* **2000**, 434.
[10] A. D. Becke, *J. Chem. Phys.* **1993**, *98*, 5648.
[11] C. Lee, W. Yang, R. G. Parr, *Phys. Rev. B: Condens. Matter* **1988**, *37*, 785.
[12] B. Miehlich, A. Savin, H. Stoll, H. Preuss, *Chem. Phys. Lett.* **1989**, *157*, 200.
[13] P. J. Stephens, F. J. Devlin, C. F. Chabalowski, M. J. Frisch, *J. Phys. Chem.* **1994**, *98*, 11623.
[14] A. Schäfer, C. Huber, R. Ahlrichs, *J. Chem. Phys.* **1994**, *100*, 5829.
[15] R. Ahlrichs, M. Bär, M. Häser, H. Horn, C. Kölmel, *Chem. Phys. Lett.* **1989**, *162*, 165.
[16] O. Treutler, R. Ahlrichs, *J. Chem. Phys.* **1995**, *102*, 346.
[17] M. v. Arnim, R. Ahlrichs, *J. Comput. Chem.* **1998**, *19*, 1746.
[18] A. D. Becke, *Phys. Rev. A* **1988**, *38*, 3089.
[19] J. P. Perdew, W. Yue, *Phys. Rev. B* **1986**, *33*, 8800.
[20] J. P. Perdew, *Phys. Rev. B* **1986**, *33*, 8822.
[21] A. D. Becke, *J. Chem. Phys.* **1993**, *98*, 1372.
[22] F. Biegler-König, J. Schönbohm, *AIM2000, v2.0*, Bielefeld, Germany, **2002**.
[23] A. Savin, R. Nesper, S. Wengert, T. F. Fässler, *Angew. Chem. Int. Ed.* **1997**, *36*, 1808.
[24] S. Noury, X. Krokidis, F. Fuster, B. Silvi, *ToPMoD Package*, Paris, **1997**.
[25] S. Noury, X. Krokidis, F. Fuster, B. Silvi, *Comput. Chem.* **1999**, *23*, 597.
[26] T. E. Taylor, M. B. Hall, *J. Am. Chem. Soc.* **1984**, *106*, 1576.

[27] C. Elschenbroich, *Organometallchemie, Vol. 5*, B.G. Teubner, Wiesbaden, **2005**.
[28] T. R. Cundari, M. S. Gordon, *J. Am. Chem. Soc.* **1991**, *113*, 5231.
[29] T. R. Cundari, M. S. Gordon, *J. Am. Chem. Soc.* **1992**, *114*, 539.
[30] T. R. Cundari, M. S. Gordon, *Organometallics* **1992**, *11*, 55.
[31] J. W. Herndon, *Coord. Chem. Rev.* **2009**, *253*, 1517.
[32] A. F. Hill, W. R. Roper, J. M. Waters, A. H. Wright, *J. Am. Chem. Soc.* **1983**, *105*, 5939.
[33] S. F. Vyboishchikov, G. Frenking, *Chem. Eur. J.* **1998**, *4*, 1428.
[34] G. Frenking, N. Fröhlich, *Chem. Rev.* **2000**, *100*, 717.
[35] M. Lein, A. Szabó, A. Kovács, G. Frenking, *Faraday Discuss.* **2003**, *124*, 365.
[36] H. Braunschweig, R. D. Dewhurst, *Angew. Chem. Int. Ed.* **2009**, *48*, 1893.
[37] G. Alcaraz, E. Clot, U. Helmstedt, L. Vendier, S. Sabo-Etienne, *J. Am. Chem. Soc.* **2008**, *129*, 8704.
[38] H. Braunschweig, *personal correspondence*.
[39] L. Andrews, X. Wang, *Matrix Infrared Spectra and Density Functional Calculations of Simple Terminal Borylene Complexes* **2009**.
[40] B. Blank, M. Colling, C. Kollann, K. Radacki, D. Rais, K. Uttinger, G. R. Whittell, H. Braunschweig, *Chem. Eur. J.* **2007**, *13*, 4770.
[41] H. Braunschweig, M. Colling, C. Kollann, K. Merz, K. Radacki, *Angew. Chem. Int. Ed.* **2001**, *40*, 4198.
[42] H. Braunschweig, M. Burzler, K. Radacki, F. Seeler, *Angew. Chem. Int. Ed.* **2007**, *46*, 8071.

Chapter 7

[1] H. Braunschweig, *Angew. Chem. Int. Ed. Engl.* **1998**, *37*, 1786.
[2] H. Braunschweig, C. Kollann and D. Rais, *Angew. Chem. Int. Ed. Engl.* **2006**, *45*, 5254.
[3] H. Braunschweig and M. Colling, *Coord. Chem. Rev.* **2001**, *223*, 1.
[4] S. Aldridge and D. L. Coombs, *Coord. Chem. Rev.* **2004**, *248*, 535.
[5] G. J. Irvine, M. J. G. Lesley, T. B. Marder, N. C. Norman, C. R. Rice, E. G. Robins, W. R. Roper, G. R. Whittell and L. J. Wright, *Chem. Rev.* **1998**, *98*, 2685.
[6] H. Braunschweig and T. Wagner, *Angew. Chem.* **1995**, *107*, 904.
[7] H. Braunschweig and B. Ganter, *J. Organomet. Chem.* **1997**, *545*, 163.
[8] R. F. W. Bader and H. Essen, *J. Chem. Phys.* **1984**, *80*, 1943.
[9] U. Flierler, M. Burzler, D. Leusser, J. Henn, H. Ott, H. Braunschweig and D. Stalke, *Angew. Chem. Int. Ed.* **2008**, *47*, 4321.
[10] R. W. F. Bader, *Atoms in Molecules: A Quantum Theory*, Oxford University Press, Oxford, **1990**.
[11] P. Macchi and A. Sironi, *Coord. Chem. Rev.* **2003**, *238*, 383.
[12] H. Braunschweig and M. Müller, *Chem. Ber./Recueil* **1997**, *130*, 1295.
[13] H. Braunschweig, C. Burschka, M. Burzler, S. Metz and K. Radacki, *Angew. Chem.* **2006**, *118*, 4458.
[14] K. Folting, J. C. Huffman, L. N. Lewis and K. Caulton, G, *Inorg. Chem.* **1979**, *18*, 3483.
[15] W. A. Herrmann, B. Reiter and H. Biersack, *J. Organomet. Chem.* **1975**, *97*, 245.
[16] D. A. Clemente, B. Rees, G. Bandoli, M. C. Biagini, B. Rieter and W. A. Herrmann, *Angew. Chem.* **1981**, *93*, 920.
[17] D. C. Calabro, D. L. Lichtenberger and W. A. Herrmann, *J. Am. Chem. Soc.* **1981**, *103*, 6852.
[18] A. D. Becke and K. E. Edgecombe, *J. Chem. Phys.* **1990**, *92*, 5397.

[19] A. Savin, R. Nesper, S. Wengert and T. F. Fässler, *Angew. Chem. Int. Ed.* **1997**, *36*, 1809.
[20] A. E. Reed, R. B. Weinstock and F. Weinhold, *J. Chem. Phys.* **1985**, *83*, 735.
[21] J. W. Lauher, M. Elian, R. H. Summerville and R. Hoffmann, *J. Am. Chem. Soc.* **1976**, *98*, 3219.
[22] D. L. Thorne and R. Hoffmann, *Inorg. Chem.* **1978**, *17*, 126.
[23] R. Hoffmann and R. H. Summerville, *J. Am. Chem. Soc.* **1979**, *101*, 3821.
[24] S. Shaik, R. Hoffmann, C. R. Fisel and R. H. Summerville, *J. Am. Chem. Soc.* **1980**, *102*, 4556.
[25] H. Willem, E. J. Baerends and P. Ros, *Faraday Symp.* **1980**, *14*, 211.
[26] J. Overgaard, H. F. Clausen, J. A. Platts and B. B. Iversen, *J. Am. Chem. Soc.* **2008**, *130*, 3834.
[27] J. A. Platts, G. J. S. Evans, M. P. Coogan and J. Overgaard, *Inorg. Chem.* **2007**, *46*, 6291.
[28] P. Macchi, D. M. Prosperpio and A. Sironi, *J. Am. Chem. Soc.* **1998**, *120*, 13429.
[29] A. A. Low, K. L. Kunze, P. J. MacDougall and M. B. Hall, *Inorg. Chem.* **1991**, *30*, 1079.
[30] P. Macchi, L. Garlaschelli and A. Sironi, *J. Am. Chem. Soc.* **2002**, *124*, 14173.
[31] P. Macchi, L. Garlaschelli, S. Martinengo and A. Sironi, *J. Am. Chem. Soc.* **1999**, *121*, 10428.
[32] R. Bianchi, G. Gervasio and D. Marabello, *Inorg. Chem.* **2000**, *39*, 2360.
[33] G. Gervasio, R. Bianchi and D. Marabello, *Chem. Phys. Lett.* **2004**, *387*, 481.
[34] M. Kaupp, *Chem. Ber.* **1996**, *129*, 527.
[35] M. Finger and J. Reinhold, *Inorg. Chem.* **2003**, *42*, 8128-8130.
[36] E. Hunstock, C. Mealli, M. J. Calhorda and J. Reinhold, *Inorg. Chem.* **1999**, *38*, 5053.
[37] A. W. Ehlers, E. J. Baerends, F. M. Bickelhaupt and U. Radius, *Chem. Eur. J.* **1998**, *4*, 210.
[38] A. D. Becke, *J. Chem. Phys.* **1993**, *98*, 5648.
[39] P. J. Stephens, F. J. Devlin, C. F. Chabalowski and M. J. Frisch, *J. Phys. Chem.* **1994**, *98*, 11623.
[40] C. Lee, W. Yang and R. G. Parr, *Phys. Rev. B: Condens. Matter* **1988**, *37*, 785.
[41] B. Miehlich, A. Savin, H. Stoll and H. Preuss, *Chem. Phys. Lett.* **1989**, *157*, 200.
[42] A. Schäfer, C. Huber and R. Ahlrichs, *J. Chem. Phys.* **1994**, *100*, 5829.
[43] R. Ahlrichs, M. Bär, M. Häser, H. Horn and C. Kölmel, *Chem. Phys. Lett.* **1989**, *162*, 165.
[44] O. Treutler and R. Ahlrichs, *J. Chem. Phys.* **1995**, *102*, 346.
[45] M. v. Arnim and R. Ahlrichs, *J. Comput. Chem.* **1998**, *19*, 1746.
[46] A. D. Becke, *Phys. Rev. A* **1998**, *38*, 3098.
[47] J. P. Perdew, *Phys. Rev. B* **1986**, *33*, 8822.
[48] A. D. Becke, *J. Chem. Phys.* **1993**, *98*, 1372.
[49] F. Biegler-König and J. Schönbohm, *AIM2000, v2.0*, Bielefeld, Germany, **2002**.
[50] S. Noury, X. Krokidis, F. Fuster and B. Silvi, *ToPMoD Package*, Paris, **1997**.
[51] S. Noury, X. Krokidis, F. Fuster and B. Silvi, *Comput. Chem.* **1999**, *23*, 597.
[52] P. Flükiger, H. P. Lüthi, S. Portmann and J. Weber, *MOLEKEL 4.0*, Swiss National Supercomputing Centre CSCS, Manno, Switzerland, **2000**.
[53] R. Bianchi, G. Gervasio and D. Marabello, *Chem. Commun.* **1998**, 1535.
[54] L. J. Farrugia, P. R. Mallinson and B. Stewart, *Acta Crystallogr. B* **2003**, *59*, 234.
[55] S. Schinzel and M. Kaupp, *unpublished results*.
[56] C. Bo, J.-P. Sarasa and J. M. Poblet, *J. Phys. Chem.* **1993**, *97*, 6362.
[57] C. Gatti and D. Lasi, *Faraday Discussion* **2007**, *135*, 55.
[58] J. Henn, D. Leusser and D. Stalke, *J. Comput. Chem.* **2007**, *28*, 2317.
[59] P. Macchi, D. M. Prosperpio and A. Sironi, *J. Am. Chem. Soc.* **1998**, *120*, 1447.
[60] W. Scherer, G. Eickerling, D. Shorokhov, E. Gullo, S. G. McGrady and P. Sirsch, *New J. Chem.* **2006**, *30*, 309.
[61] S. Patchkovskii and T. Ziegler, *J. Chem. Phys.* **1999**, *111*, 5730.
[62] W. Koch and M. C. Holthausen, *A Chemist's Guide to Density Functional Theory: An Introduction*, Wiley-VCH, Weinheim, **2000**, p. 308-310.
[63] M. Kaupp, R. Reviakine, O. L. Malkina, A. Arbuznikov, B. Schimmelpfennig and V. G. Malkin, *J. Comput. Chem.* **2002**, *23*, 794.
[64] M. Munzarova and M. Kaupp, *J. Phys. Chem. A* **1999**, *103*, 9966.

[65] J. P. Perdew, M. Ernzerhof and K. Burke, *J. Chem. Phys.* **1996**, *105*, 9982.
[66] J. Fritscher, P. Hrobarik and M. Kaupp, *J. Phys. Chem. B* **2007**, *111*, 4616.
[67] M. Kaupp, R. Reviakine, O. L. Malkina, A. V. Arbouznikov, B. Schimmelpfennig and V. G. Malkin, *J. Comput. Chem.* **2002**, *23*, 794.
[68] C. Remenyi, R. Reviakine and M. Kaupp, *J. Phys. Chem. B* **2007**, *111*, 8290.
[69] F. Furche and J. P. Perdew, *J. Chem. Phys.***2006**, *124*, 044103.
[70] W. Koch and M. C. Holthausen, *A Chemist's Guide to Density Functional Theory, 2nd Edition*, Wiley-VCH, Weinheim, **2001**, p. 528.
[71] S. Riedel and M. Kaupp, *Inorg. Chem.* **2006**, *45*, 1228.
[72] S. Riedel, M. Straka and M. Kaupp, *Phys. Chem. Chem. Phys.* **2004**, *6*, 1122.
[73] R. F. W. Bader, T. T. Nguyen-Dang and Y. Tal, *Reports on Progress in Physics* **1981**, *44*, 893.
[74] P. Hofmann, *Angew. Chem.* **1979**, *91*, 591.
[75] K. H. Döth, H. Fischer, P. Hofmann, F. R. Kreissl, U. Schubert and K. Weiss, *Transition Metal Carbene Complexes*, Verlag Chemie, Weinheim, **1983**.
[76] H. Braunschweig and M. Colling, *J. Organomet. Chem.* **2000**, *614-615*, 18.
[77] H. Braunschweig, M. Colling and C. Hu, *Inorg. Chem.* **2003**, *42*, 941.
[78] H. Braunschweig, M. Colling, C. Hu and K. Radacki, *Inorg. Chim. Acta* **2004**, *357*, 1822.
[79] R. F. W. Bader, S. Johnson, T. H. Tang and P. L. A. Popelier, *J. Phys. Chem.* **1996**, *100*, 15398.
[80] R. W. F. Bader and G. L. Heard, *J. Chem. Phys.* **1999**, *111*, 8789.
[81] B. Silvi, J. Pilme, F. Fuster and M. E. Alikhani, *NATO Science Series, II: Mathematics, Physics and Chemistry* **2003**, *116*, 241.
[82] K. Besancon, G. Laurenczy, T. Lumini, R. Roulet, R. Bruyndonckx and C. Daul, *Inorg. Chem.* **1998**, *37*, 5634.
[83] H. Chevreau, C. Martinsky, A. Sevin, C. Minot and B. Silvi, *New J. Chem.* **2003**, *27*, 1049.
[84] U. Effertz, U. Englert, F. Podewils, A. Salzer, T. Wagner and M. Kaupp, *Organometallics* **2003**, *22*, 264.
[85] G. Jansen, M. Schubart, B. Findeis, L. H. Gade, I. J. Scowen and M. McPartlin, *J. Am. Chem. Soc.* **1998**, *120*, 7239.
[86] P. J. Low, R. Rousseau, P. Lam, K. A. Udachin, G. D. Enright, J. S. Tse, D. D. M. Wayner and A. J. Carty, *Organometallics* **1999**, *18*, 3885-3897.
[87] J. Andres, S. Berski, M. Feliz, R. Llusar, F. Sensato and B. Silvi, *Comptes Rend. Chimie* **2005**, *8*, 1400.
[88] A. Savin, B. Silvi and F. Colonna, *Canad. J. Chem.* **1996**, *74*, 1088.
[89] B. Silvi and A. Savin, *Nature* **1994**, *371*, 683.

Chapter 8

[1] R. W. F. Bader, *Atoms in Molecules: A Quantum Theory*, Oxford University Press, Oxford, **1990**.
[2] A. D. Becke and K. E. Edgecombe, *J. Chem. Phys.* **1990**, *92*, 5397.
[3] A. Savin, R. Nesper, S. Wengert and T. F. Fässler, *Angew. Chem. Int. Ed.* **1997**, *36*, 1808.
[4] A. E. Reed, R. B. Weinstock and F. Weinhold, *J. Chem. Phys.* **1985**, *83*, 735.
[5] A. D. Becke, *J. Chem. Phys.* **1993**, *98*, 5648.
[6] P. J. Stephens, F. J. Devlin, C. F. Chabalowski and M. J. Frisch, *J. Phys. Chem.* **1994**, *98*, 11623.
[7] C. Lee, W. Yang and R. G. Parr, *Phys. Rev. B: Condens. Matter* **1988**, *37*, 785.

[8] B. Miehlich, A. Savin, H. Stoll and H. Preuss, *Chem. Phys. Lett.* **1989**, *157*, 200.
[9] A. Schäfer, C. Huber and R. Ahlrichs, *J. Chem. Phys.* **1994**, *100*, 5829.
[10] R. Ahlrichs, M. Bär, M. Häser, H. Horn and C. Kölmel, *Chem. Phys. Lett.* **1989**, *162*, 165.
[11] O. Treutler and R. Ahlrichs, *J. Chem. Phys.* **1995**, *102*, 346.
[12] M. v. Arnim and R. Ahlrichs, *J. Comput. Chem.* **1998**, *19*, 1746.
[13] A. D. Becke, *Phys. Rev. A* **1998**, *38*, 3098.
[14] J. P. Perdew, *Phys. Rev. B* **1986**, *33*, 8822.
[15] A. D. Becke, *J. Chem. Phys.* **1993**, *98*, 1372.
[16] F. Biegler-König and J. Schönbohm, *AIM2000, v2.0*, Bielefeld, Germany, **2002**.
[17] S. Noury, X. Krokidis, F. Fuster and B. Silvi, *ToPMoD Package*, Paris, **1997**.
[18] S. Noury, X. Krokidis, F. Fuster and B. Silvi, *Comput. Chem.* **1999**, *23*, 597.
[19] M. Forster, *Photochemisch und thermisch induzierter Borylentransfer auf späte Übergangsmetallsysteme*, Doktorarbeit, Universität Würzburg, **2009**.
[20] H. Braunschweig, B. Christ, M. Colling, M. Forster, K. Götz, M. Kaupp, K. Radacki and F. Seeler, *Chem. Eur. J.* **2009**, *15*, 7150.
[21] H. Braunschweig, M. Forster, K. Radacki, F. Seeler and G. R. Whittell, *Angew. Chem. Int. Ed.* **2007**, *46*, 5212.
[22] *determined by K. Radacki.*
[23] W. R. J. Bailey, D. M. Collins, F. A. Cotton, J. C. Baldwin and W. C. Kaska, *Organomet. Chem.* **1979**, *165*, 373.
[24] D. Adhikari, J. Huffmann and D. J. Mindiola, *Chem. Commun.* **2007**, 4489.
[25] U. Flierler, M. Burzler, D. Leusser, J. Henn, H. Ott, H. Braunschweig and D. Stalke, *Angew. Chem. Int. Ed.* **2008**, *47*, 4321.
[26] K. Götz, M. Kaupp, H. Braunschweig and D. Stalke, *Chem. Eur. J.* **2009**, *15*, 623.

Chapter 9

[1] W. Schlenk, J. Holtz, *Ber. Dtsch. Chem. Ges.* **1917**, *50*, 262.
[2] V. H. Gessner, C. Däschlein, C. Strohmann, *Chem. Eur. J.* **2009**, *15*, 320.
[3] A. Streitwieser Jr., *J. Organomet. Chem.* **1978**, *156*, 1.
[4] R. J. Bushby, H. L. Steel, *J. Organomet. Chem.* **1987**, *336*, C25.
[5] R. J. Bushby, H. L. Steel, *J. Chem. Soc. Perkin Trans.* **1990**, *2*, 1143.
[6] D. Stalke, T. Stey, *Lead Structures in Lithium Organic Chemistry in The Chemistry of Organolithium Compounds*, John Wiley & Sons, Ltd, **2004**.
[7] C. Elschenbroich, *Organometallchemie, Vol. 5*, B.G. Teubner, Wiesbaden, **2005**.
[8] R. E. Dinnebier, U. Behrend, F. Olbrich, *Organometallics* **1997**, *16*, 3855.
[9] R. E. Dinnebier, U. Behrends, F. Olbrich, *J. Am. Chem. Soc.* **1998**, *120*, 1430.
[10] E. Weiss, T. Lambertsena, B. Schubert, J. K. Cockcroft, A. Wiedenmann, *Chem. Ber.* **1990**, *123*, 79.
[11] Y. Ohta, A. Denmura, T. Okamoto, H. Hitomi, M. Nagaoka, *J. Phys. Chem. B* **2006**, *110*, 12640.
[12] O. Kwon, F. Sevin, M. L. McKee, *J. Phys. Chem. A* **2001**, *105*, 913.
[13] T. Kottke, D. Stalke, *Angew. Chem. Int. Ed.* **1993**, *32*, 580.
[14] H. J. Dietrich, *J. Organomet. Chem.* **1981**, *205*, 291.
[15] U. Siemeling, T. Redecker, B. Neumann, H.-G. Stammler, *J. Am. Chem. Soc.* **1994**, *116*, 5507.
[16] E. Kaufmann, K. Raghavachari, A. E. Reed, P. v. R. Schleyer, *Organometallics* **1988**, *7*, 1597.

[17] J. R. van Eikema Hommes, P. v. R. Schleyer, *Tetrahedron* **1994**, *50*, 5903.
[18] J. L. Wardell, in *Comprehensive Organometallic Chemistry* (Eds.: J. Wilkinson, F. G. A. Stone, E. W. Abel), Pergamon, New York, **1982**, Chapter 2.
[19] M. P. Bernstein, D. B. Collum, *J. Am. Chem. Soc.* **1993**, *115*, 789.
[20] M. P. Bernstein, D. B. Collum, *J. Am. Chem. Soc.* **1993**, *115*, 8008.
[21] F. Hoeffner, T. Brinck, *Organometallics* **2001**, *20*, 5134.
[22] S. Liao, D. B. Collum, *J. Am. Chem. Soc.* **2003**, *125*, 15114.
[23] C. Strohmann, V. H. Gessner, *J. Am. Chem. Soc.* **2008**, *130*, 11719.
[24] P. Verstraete, A. Deffieux, A. Fritsch, J. C. Rayez, M. T. Rayez, *THEOCHEM* **2003**, *631*, 53.
[25] E. Matito, J. Poater, F. M. Bickelhaupt, M. Solà, *J. Phys. Chem. B* **2006**, *110*, 7189.
[26] P. Fuentealba, A. Savin, *J. Phys. Chem. A* **2001**, *105*, 11531.
[27] W. Bauer, A. M. Sapse, P. v. R. Schleyer, in *Lithium Chemistry*, Wiley Interscience, New York, **1995**.
[28] F. M. Bickelhaupt, J. R. van Eikema Hommes, C. F. Guerra, E. J. Baerends, *Organometallics* **1996**, *15*, 2923.
[29] F. M. Bickelhaupt, M. Solà, C. F. Guerra, *J. Chem. Theory Comput.* **2006**, *2*, 965.
[30] R. Ponec, J. Roithová, X. Gironés, L. Lain, A. Torre, R. Bochicchio, *J. Phys. Chem. A* **2002**, *106*, 1019.
[31] M. Brookhart, M. L. H. Green, *J. Organometall. Chem.* **1983**, *250*, 395.
[32] R. H. Crabtree, *Angew. Chem. Int. Ed.* **1993**, *32*, 789.
[33] J. J. Schneider, *Angew. Chem. Int. Ed.* **1996**, *35*, 1068.
[34] D. Braga, F. Grepioni, K. Biradha, G. R. Desiraju, *J. Chem. Soc. Dalton Trans.* **1996**, 3925.
[35] A. de la Lande, C. Fressigné, H. Gérard, J. Maddaluno, O. Parisel, *Chem. Eur. J.* **2007**, *13*, 3459.
[36] P. v. R. Schleyer, A. J. Kos, *Tetrahedron* **1983**, *39*, 1141.
[37] A. E. Reed, P. v. R. Schleyer, *J. Am. Chem. Soc.* **1990**, *112*, 1434.
[38] P. Petillo, L. Lerner, *ACS Symp. Ser.* **1993**, *539*, 156.
[39] F. Weinhold, *Nature* **2001**, *411*, 539.
[40] V. Pophristic, L. Gooman, *Nature* **2001**, *411*, 565.
[41] H. Ott, C. Däschlein, D. Leusser, D. Schildbach, T. Seibel, D. Stalke, C. Strohmann, *J. Am. Chem. Soc.* **2008**, *130*, 11901.
[42] W. Scherer, P. Sirsch, D. J. Shorokhov, S. G. McGrady, S. A. Mason, M. G. Gardiner, *Chem. Eur. J.* **2002**, *8*, 2324.

Chapter 10

[1] K. Schwarz, P. Blaha, *Comput. Mater. Sci.* **2003**, *28*, 259.
[2] J. Hafner, *Comput. Phys. Commun.* **2007**, *117*, 6.
[3] R. Dovesi, V. R. Saunders, C. Roetti, R. Orlando, C. M. Zicovich-Wilson, F. Pascale, B. Civalleri, K. Doll, N. M. Harrison, I. J. Bush, P. D'Arco, M. Llunell, *CRYSTAL06*, *v.1.0.2*. **2007**.
[4] R. Dovesi, B. Civalleri, R. Orlando, C. Roetti, V. R. Saunders, *Rev. Comput. Chem.* **2005**, *21*, 1.
[5] M. Ferrero, M. Rérat, R. Orlando, R. Dovesi, *J. Chem. Phys.* **2008**, *128*, 14110.
[6] B. Paulus, P. Fulde, H. Stoll, *Phys. Rev. B* **1995**, *51*, 10572.
[7] K. Kopitzki, *Einführung in die Festkörperphysik, Vol. 3*, B.G. Teubner, Stuttgart, **1993**.
[8] F. Bloch, *Z. Phys.* **1928**, *52*, 555.

[9] C. Peter, W. F. van Gunsteren, P. H. Hünenberger, *J. Chem. Phys.* **2003**, *119*, 12205.
[10] P. Ewald, *Ann. Phys.* **1921**, *369*, 253.
[11] M. D. Towler, *An introductory guide to Gaussian basis sets in solid-state electronic structure calculations*, Notes for Summer School "Ab initio modelling in solid-state chemistry" (Torino), **2000**.
[12] E. Miertus, E. Scrocco, J. Tomasi, *Chem. Phys. Lett.* **1981**, *55*, 117.
[13] A. Klamt, Schüürmann, *J. Chem. Soc. Perkin Trans.* **1993**, *2*, 799.
[14] J. Tomasi, M. Persico, *Chem. Rev.* **1994**, *94*, 2027.
[15] R. Cammi, J. Tomasi, *J. Comput. Chem.* **1995**, *16*, 1449.
[16] A. Burow, M. Sierka, J. Döbler, J. Sauer, *J. Chem. Phys.* **2009**, *130*, 174710.
[17] A. Schäfer, A. Klamt, D. Sattel, J. C. W. Lohrenz, F. Eckert, *Phys. Chem. Chem. Phys.* **2000**, *2*, 2187.
[18] A. Laio, J. VandeVondele, L. Visscher, *J. Chem. Phys.* **2002**, *116*, 6941.
[19] C. G. Lambert, T. A. Darden, J. A. Board Jr., *J. Comput. Chem.* **1996**, *126*, 274.
[20] K. N. Kudin, G. E. Scuseria, *Chem. Phys. Lett.* **1998**, *283*, 61.
[21] K. N. Kudin, G. E. Scuseria, *J. Chem. Phys.* **2004**, *121*, 2886.
[22] V. Rokhlin, *J. Comput. Chem.* **1985**, *60*, 187.
[23] L. Greengard, "The Rapid Evaluation of Potential Fields in Particle Systems" PhD Thesis, MIT (Cambridge), **1987**.
[24] C. A. White, M. Head-Gordon, *J. Chem. Phys.* **1994**, *101*, 6593.
[25] J. Sauer, M. Sierka, *J. Comput. Chem.* **2000**, *21*, 1470.
[26] H. M. Senn, W. Thiel, *Angew. Chem.* **2009**, *121*, 1220.

Chapter 11

[1] R. W. F. Bader, *Atoms in Molecules: A Quantum Theory*, Oxford University Press, Oxford, **1990**.
[2] P. Luger, *Org. Biomol. Chem.* **2007**, *5*, 2529.
[3] C. Gatti, *Z. Kristallogr.* **2005**, *220*, 399.
[4] A. Volkov, Y. Abramov, P. Coppens and C. Gatti, *Acta Crystallogr. A* **2000**, *56*, 332.
[5] C. Gatti, R. Bianchi, R. Destro and F. Merati, *THEOCHEM* **1992**, *255*, 409.
[6] T. Koritsanszky, R. Flaig, D. Zobel, H.-G. Krane, W. Morgenroth and P. Luger, *Science* **1998**, *279*, 356.
[7] S. T. Howard, M. B. Hursthouse, C. W. Lehmann and E. A. Poyner, *Acta Crystallogr. B* **1995**, *51*, 328.
[8] R. Flaig, T. Koritsanszky, D. Zobel and P. Luger, *J. Am. Chem. Soc.* **1998**, *120*, 2227.
[9] P. Coppens, Y. Abramov, M. Carducci, B. Korjov, I. Novozhilova, C. Alhambra and M. R. Pressprich, *J. Am. Chem. Soc.* **1999**, *121*, 2585.
[10] P. Coppens and A. Volkov, *Acta Crystallogr. A* **2004**, *60*, 357.
[11] M. Kappkhan, V. G. Tsirelson and R. P. Ozerov, *Dokl. Akad. SSSr* **1988**, *303*, 404.
[12] M. A. Spackman, P. G. Byrom, M. Alfredsson and K. Hermansson, *Acta Crystallogr. A* **1999**, *55*, 30.
[13] R. Destro, R. Bianchi, C. Gatti and F. Merati, *Chem. Phys. Lett.* **1991**, *186*, 47.
[14] E. May, R. Destro and C. Gatti, *J. Am. Chem. Soc.* **2001**, *123*, 12248.
[15] J. Henn, D. Leusser, D. Ilge, B. Engels and D. Stalke, *J. Phys. Chem. A* **2004**, *2004*, 9442.
[16] L. Bertini, F. Cargnoni and C. Gatti, *Theor. Chem. Acc.* **2007**, *117*, 847.

[17] R. Dovesi, V. R. Saunders, C. Roetti, R. Orlando, C. M. Zicovich-Wilson, F. Pascale, B. Civalleri, K. Doll, N. M. Harrison, I. J. Bush, P. D'Arco and M. Llunell, *CRYSTAL06*, **2007**.
[18] V. Luana, A. Costales and A. M. Pendas, *Phys. Rev. B* **1997**, *55*, 4285.
[19] A. M. Pendas, A. Costales and V. Luana, *Phys. Rev. B* **1997**, *55*, 4275.
[20] E. A. Zhurova, J. M. Zuo and V. G. Tsirelson, *J. Phys. Chem. of Solids* **2001**, *62*, 2143.
[21] E. A. Zhurova, Y. Ivanov, V. Zavodnik and V. Tsirelson, *Acta. Crystallogr. B* **2000**, *56*, 594.
[22] E. Miertus, E. Scrocco and J. Tomasi, *Chem. Phys. Lett.* **1981**, *55*, 117.
[23] A. Klamt and G. Schüürmann, *J. Chem. Soc. Perkin Trans.* **1993**, *2*, 799.
[24] J. Tomasi and M. Persico, *Chem. Rev.* **1994**, *94*, 2027.
[25] R. Cammi and J. Tomasi, *J. Comput. Chem.* **1995**, *16*, 1449.
[26] A. Burow, M. Sierka, J. Döbler and J. Sauer, *J. Chem. Phys.* **2009**, *130*, 174710.
[27] K. Kiewisch, G. Eickerling, M. Reiher and J. Neugebauer, *J. Chem. Phys.* **2008**, *128*, 044114.
[28] S. Fux, K. Kiewisch, C. R. Jacob, J. Neugebauer and M. Reiher, *Chem. Phys. Lett.* **2008**, *461*, 353.
[29] T. A. Wesolowski and A. Warshel, *J. Phys. Chem.* **1993**, *97*, 8050.
[30] Y. Ohta, A. Demura, T. Okamoto, H. Hitomi and M. Nagaoka, *J. Phys. Chem. B* **2006**, *110*, 12640.
[31] O. Kwon, F. Sevin and M. L. McKee, *J. Phys. Chem. A* **2001**, *105*, 913.
[32] M. v. Arnim and R. Ahlrichs, *J. Comput. Chem.* **1998**, *19*, 1746.
[33] O. Treutler and R. Ahlrichs, *J. Chem. Phys.* **1995**, *102*, 346.
[34] R. Ahlrichs, M. Bär, M. Häser, H. Horn and C. Kölmel, *Chem. Phys. Lett.* **1989**, *162*, 165.
[35] E. Weiss, T. Lambertsena, B. Schubert, J. K. Cockcroft and A. Wiedenmann, *Chem. Ber.* **1990**, *123*, 79.
[36] A. Klamt and Schüürmann, *J. Chem. Soc. Perkin Trans.* **1993**, *2*, 799.
[37] P. Fuentealba, H. Preuss, H. Stoll and L. Von Szentply, *Chem. Phys. Lett.* **1982**, *89*, 418.
[38] F. Biegler-König and J. Schönbohm, *AIM2000, v2.0*, Bielefeld, Germany, **2002**.
[39] C. Gatti, *TOPOND08*, Milano, **2008**.
[40] J. P. Perdew, *Phys. Rev. B* **1986**, *33*, 8822.
[41] A. D. Becke, *Phys. Rev. A* **1998**, *38*, 3098.
[42] C. Lee, W. Yang and R. G. Parr, *Phys. Rev. B: Condens. Matter* **1988**, *37*, 785.
[43] B. Miehlich, A. Savin, H. Stoll and H. Preuss, *Chem. Phys. Lett.* **1989**, *157*, 200.
[44] P. J. Stephens, F. J. Devlin, C. F. Chabalowski and M. J. Frisch, *J. Phys. Chem.* **1994**, *98*, 11623.
[45] A. D. Becke, *J. Chem. Phys.* **1993**, *98*, 5648.
[46] R. Dovesi, B. Civalleri, R. Orlando, C. Roetti and V. R. Saunders, *Rev. Comput. Chem.* **2005**, *21*, 1.
[47] M. D. Towler, *An introductory guide to Gaussian basis sets in solid-state electronic structure calculations,* Notes for Summer School "Ab initio modelling in solid-state chemistry", Torino, **2000**.
[48] A. Schäfer, C. Huber and R. Ahlrichs, *J. Chem. Phys.* **1994**, *100*, 5829.
[49] F. Weigend, F. Furche and R. Ahlrichs, *J. Chem. Phys.* **2003**, *119*, 12753.
[50] A. Schäfer, H. Horn and R. Ahlrichs, *J. Chem. Phys.* **1992**, *97*, 2571.
[51] N. Godbout, R. Salahub, J. Andzelm and E. Wimmer, *Can. J. Chem.* **1992**, *70*, 560.

Chapter 12

[1] C. Strohmann and V. H. Gessner, *J. Am. Chem. Soc.* **2007**, *129*, 5982.
[2] C. Strohmann and V. H. Gessner, *Angew. Chem. Int. Ed.* **2007**, *46*, 8281.
[3] M. A. Nichols and P. G. Willard, *J. Am. Chem. Soc.* **1993**, *115*, 1568.
[4] N. D. R. Barnett and R. E. Mulvey, *J. Am. Chem. Soc.* **1993**, *115*, 1573.
[5] C. Strohmann, K. Strohfeld and D. Schildbach, *J. Am. Chem. Soc.* **2003**, *125*, 13672.
[6] C. Strohmann and V. H. Gessner, *J. Am. Chem. Soc.* **2008**, *130*, 11719.
[7] D. Stalke and T. Stey, *Lead Structures in Lithium Organic Chemistry in The Chemistry of Organolithium Compounds*, John Wiley & Sons, Ltd, **2004**.
[8] R. Ahlrichs, M. Bär, M. Häser, H. Horn and C. Kölmel, *Chem. Phys. Lett.* **1989**, *162*, 165.
[9] O. Treutler and R. Ahlrichs, *J. Chem. Phys.* **1995**, *102*, 346.
[10] M. v. Arnim and R. Ahlrichs, *J. Comput. Chem.* **1998**, *19*, 1746.
[11] A. Schäfer, C. Huber and R. Ahlrichs, *J. Chem. Phys.* **1994**, *100*, 5829.
[12] A. D. Becke, *Phys. Rev. A* **1988**, *38*, 3089.
[13] J. P. Perdew, *Phys. Rev. B* **1986**, *33*, 8822.
[14] J. P. Perdew and W. Yue, *Phys. Rev. B* **1986**, *33*, 8800.
[15] E. Weiss, T. Lambertsena, B. Schubert, J. K. Cockcroft and A. Wiedenmann, *Chem. Ber.* **1990**, *123*, 79.
[16] A. Klamt and Schüürmann, *J. Chem. Soc. Perkin Trans.* **1993**, *2*, 799.
[17] A. Burow, M. Sierka, J. Döbler and J. Sauer, *J. Chem. Phys.* **2009**, *130*, 174710.
[18] F. Biegler-König and J. SchöNPAhm, *AIM2000, v2.0*, Bielefeld, Germany, **2002**.
[19] M. J. Frisch, G. W. Trucks, H. B. Schlegel, G. E. Scuseria, M. A. Robb, J. R. Cheeseman, J. Montgomery, J. A.; , T. Vreven, K. N. Kudin, J. C. Burant, J. M. Millam, S. S. Iyengar, J. Tomasi, V. Barone, B. Mennucci, M. Cossi, G. Scalmani, N. Rega, G. A. Petersson, H. Nakatsuji, M. Hada, M. Ehara, K. Toyota, R. Fukuda, J. Hasegawa, M. Ishida, T. Nakajima, Y. Honda, O. Kitao, H. Nakai, M. Klene, X. Li, J. E. Knox, H. P. Hratchian, J. B. Cross, V. Bakken, C. Adamo, J. Jaramillo, R. Gomperts, R. E. Stratmann, O. Yazyev, A. J. Austin, R. Cammi, C. Pomelli, J. W. Ochterski, P. Y. Ayala, K. Morokuma, G. A. Voth, P. Salvador, J. J. Dannenberg, V. G. Zakrzewski, S. Dapprich, A. D. Daniels, M. C. Strain, O. Farkas, D. K. Malick, A. D. Rabuck, K. Raghavachari, J. B. Foresman, J. V. Ortiz, Q. Cui, A. G. Baboul, S. Clifford, J. Cioslowski, B. B. Stefanov, G. Liu, A. Liashenko, P. Piskorz, I. Komaromi, R. L. Martin, D. J. Fox, T. Keith, M. A. Al-Laham, C. Y. Peng, A. Nanayakkara, M. Challacombe, P. M. W. Gill, B. Johnson, W. Chen, M. W. Wong, C. Gonzalez and J. A. Pople, *Gaussian03 Revision B04* **2003**, Gaussian, Inc., Wallingford CT.
[20] C. A. Ogle, B. K. Huckabee, H. C. Johnson IV, P. F. Sims, A. Winslow and A. Pinkerton, *Organometallics* **1960**, *12*, 1193.
[21] H. Köster, D. Thoennes and E. Weiss, *J. Organomet. Chem.* **1978**, *160*, 1.
[22] K. Götz, V. H. Gessner, M. Kaupp and C. Strohmann, *manuscript in preparation,* **2009**.
[23] V. H. Gessner, *Lithiumorganische Verbindungen - Von der Struktur-Reaktivitätsbeziehung zu vielseitigen Synthesebausteinen und ihrer Anwendung*, Doktroarbeit, TU Dortmund, **2009**.
[24] C. Strohmann and V. H. Gessner, *J. Am. Chem. Soc.* **2007**, *129*, 8952.
[25] Y. Ohta, A. Denmura, T. Okamoto, H. Hitomi and M. Nagaoka, *J. Phys. Chem. B* **2006**, *110*, 12640.
[26] O. Kwon, F. Sevin and M. L. McKee, *J. Phys. Chem. A* **2001**, *105*, 913.
[27] E. Kaufmann, K. Raghavachari, A. E. Reed and P. v. R. Schleyer, *Organometallics* **1988**, *7*, 1597.
[28] D. B. Collum, *Acc. Chem. Res.* **1992**, *25*, 448.
[29] J. L. Rutherford, D. Hoffmann and D. B. Collum, *J. Am. Chem. Soc.* **2002**, *124*, 264.
[30] J. C. Riggs, K. J. Singh, M. Yun and D. B. Collum, *J. Am. Chem. Soc.* **2008**, *130*, 13709.

Appendix A

Modell	Molecular Graph	Laplace Map	ELF Isosurface
1	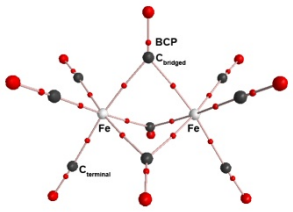	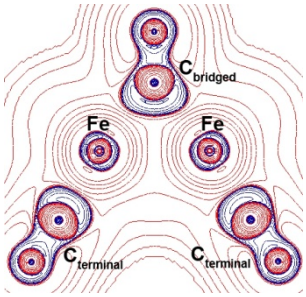	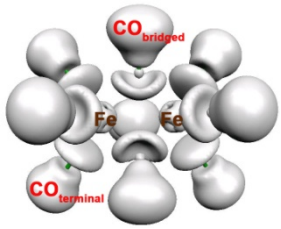
2	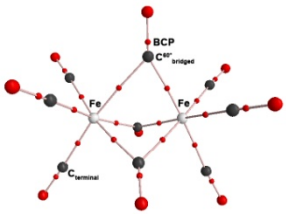	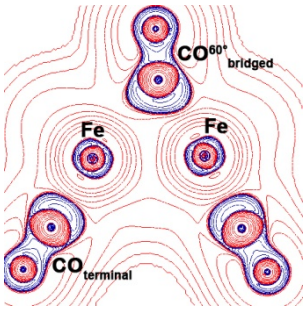	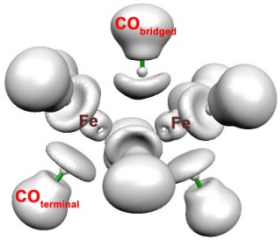
3	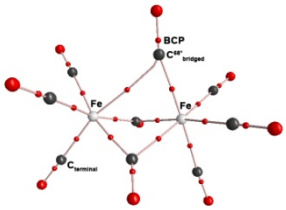	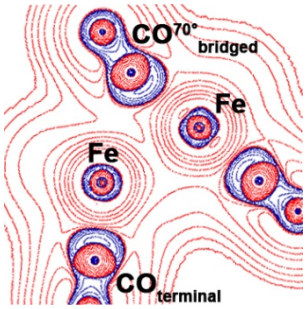	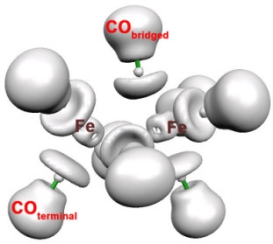
4	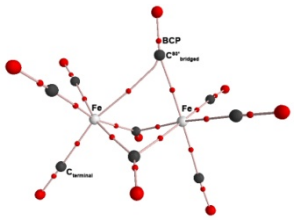	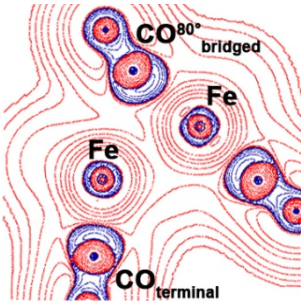	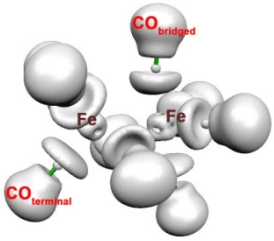

5

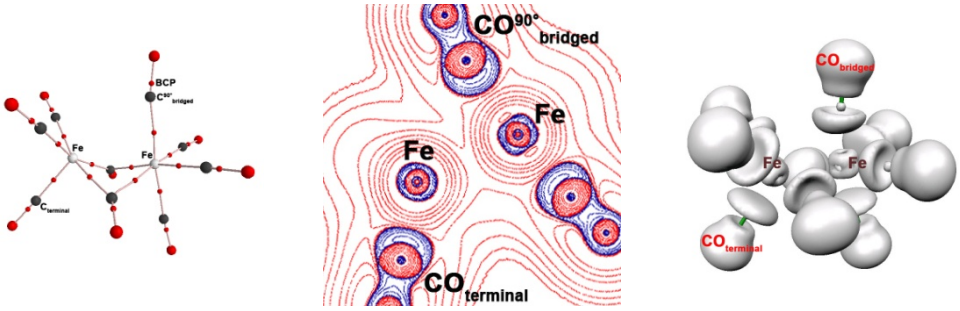

Figure A1. Molecular graphs, Laplacian Maps (charge concentrations are denoted in blue, charge depletions in red) and ELF isosurfaces η=0.7.

Appendix B

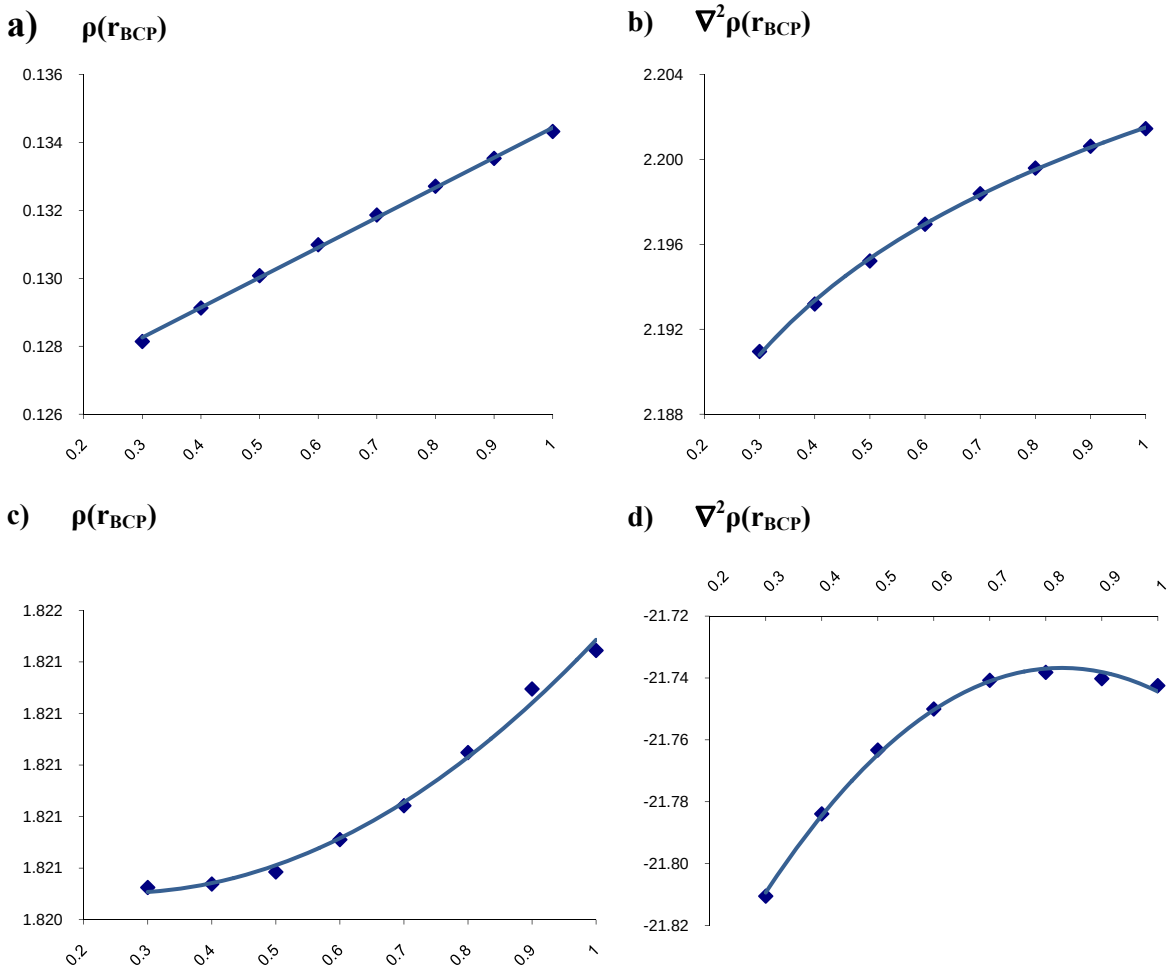

Figure B1. Electron density [eÅ^{-3}] and Laplacian values [eÅ^{-5}] at **a**, **b**) Li–C and **c**, **d**) C–H bond critical points, respectively, for increasing charges (0.3-1.0 e) employed within PEECM. Trend line included.

Appendix C

Table C1. QTAIM charges[a]

Model		QTAIM charge			
		Li	**C**	**H**	$\Sigma_{(MeLi)4}$[b]
Isolated	**1a**	0.892	-0.670	-0.071	0.036
	1c	0.866	-0.598	-0.108	-0.219
PCM	**2a**	0.904	-0.628	-0.088	0.042
	2c	0.875	-0.607	-0.092	-0.028
PEECM	**3c**	0.888	-0.665	-0.067	0.089
	3d	0.882	-0.647	-0.087	-0.108
PBC crystal	**4**	0.876	-0.625	-0.084	0.001

[a]B3LYP/TZVP results (Li-TZVP-s for the crystal calculations). [b]Sum of computed charges within the tetrameric central unit.

List of Compounds

1 $Fe_2(CO)_9$

2 $[Fe_2(SCH_2SCH_2S)(CO)_6]$

3 $[Fe_2\{BN(SiMe_3)_2\}(\eta^5\text{-}C_5H_4Me)_2(CO)_3]$

4 $[Fe_2(CO)_6(PH_2)_2]$

5 $[Fe_2(CO)_6(PF_3)_2]$

6 F_2TiBF

7 Cp_2TiBF

8 $(CO)_5MoBCl$

9 $[\{(\eta^5\text{-}C_5H_5)(OC)_2Mn\}_2\{\mu\text{-}B\text{–}t\text{Bu}\}]$

10 $[\{(\eta^5\text{-}C_5H_5)(OC)_2Mn\}_2\{\mu\text{-}BN(CH_3)_2\}]$

11 $[\{(\eta^5\text{-}C_5H_5)(OC)_2Mn\}_2\{\mu\text{-}CCH_2\}]$

12 $[\{(\eta^5\text{-}C_5H_5)(OC)_2Mn\}_2\{\mu\text{-}CH_2\}]$

13 $Mn_2(CO)_{10}$

14 $[\{(\eta^5\text{-}C_5H_4Me)Co\}_2\{\mu\text{-}(CO)\}_2\{\mu\text{-}BN(SiMe_3)_2\}]$

15 $[\{(\eta^5\text{-}C_5H_5)Ni\}_2\{\mu\text{-}(CO)\}\{\mu\text{-}BN(SiMe_3)_2\}]$

16 $[\{(\eta^5\text{-}C_5H_5)Co(CO)\}_2\{\mu\text{-}BN(SiMe_3)_2\}]$

17 $[CH_3Li{\cdot}Et_2O]_4$

18 $[CH_3Li{\cdot}(R,R)\text{-}\{C_6H_8N(CH_3)_2\}]_2$

19 $[MeLi{\cdot}trans\text{-}\{C_6H_8N(CH_3)_2\}]_2$

20 $[MeLi{\cdot}(–)\text{-sparteine}]_2$

21 $[MeLi{\cdot}(+)\text{-sparteine-surrogate}]_2$

22 $[CH_3Li{\cdot}(R,R)\text{-}\{C_6H_8N(CH_3)_2\}]$

23 $[CH_3Li{\cdot}(R,R)\text{-}\{C_6H_8N(CH_3)_2\}]_3$

24 $[CH_3Li{\cdot}NEt_3]_4$

25 $[CH_3Li]_4$

List of Publications

Publications

1 Oliver Seiler, Christian Burschka, Kathrin Götz, Martin Kaupp, Stefan Metz, Reinhold Tacke "The New λ_6 Si-Silicate Dianion $[Si(NCO)_6]_2^-$: Synthesis and Structural Charaterization of $[K(18\text{-crown-}6)]_2[Si(NCO)_6]$" *Z. Anorg. Allg. Chem*. **2007**, *633*, 2667-2670.

2 Kathrin Götz, Martin Kaupp, Holger Braunschweig, Dietmar Stalke "Comparative Analysis of Electron-Density and Electron-Localization Function for Dinuclear Manganese Complexes with Bridging Boron- and Carbon-Centered Ligands" *Chem. Eur. J*. **2009**, *15*, 623-632.

3 Holger Braunschweig, Bastian Christ, Miriam Colling, Melanie Forster, Kathrin Götz, Martin Kaupp, Krzysztof Radacki, Fabian Seeler "Synthesis, Structure and Bonding of Novel Homodinuclear Cobalt and Nickel Borylene Complexes" *Chem. Eur. J.* **2009**, *15*, 7150.

4 Peter W. Lippert, Christian Burschka, Kathrin Götz, Martin Kaupp, Diana Ivanova, Claudine Gaudon, Yoshiteru Sato, Pierre Antony, Natacha Rochel, Dino Moras, Hinrich Gronemeyer, Reinhold Tacke "Silicon Analogues of the RXR-Selective Retinoid Agonist SR11237 (BMS649): Chemistry and Biology" *Chem. Med. Chem*. **2009**, *4*, 1143-1152.

5 Stefan Metz, Jennifer B. Nätscher, Christian Burschka, Kathrin Götz, Martin Kaupp, Philip Kraft, Reinhold Tacke "Disila-Phantolide and Derivatives: Synthesis and Olfactory Characterization of Silicon-Containing derivatives of the Musk Odorant Phantolide" *Organometallics* **2009**, 28, 4700-4712.

6 Sebastian Burck, Kathrin Götz, Martin Kaupp, Martin Nieger, Jörn Schmedt auf der Günne, Dietrich Gudat "Diphosphines with strongly polarized PP-bonds: Hybrids between covalent molecules and donor-acceptor adducts with flexible molecular structure" *J. Am. Chem. Soc*. **2009**, *131*, 10763-10774.

7 Kathrin Götz, Florian Meier, Carlo Gatti, Asbjörn Burow, Marek Sierka, Joachim Sauer, Martin Kaupp "Modeling Environmental Effects on Charge Density Distributions in Polar Organometallics. Validation of Embedded Cluster Models for the Methyl Lithium Crystal" *submitted*.

Poster Presentations

1 „Experimental Charge Density and Theoretical Studies on $Me_2Al(\mu\text{-}Py)_2P$ – Evidence for P–C Single Bonding"; Kathrin Götz, Julian Henn, Dirk Leuser, Andreas Oechsner, Gerald Schwab, Dietmar Stalke, *4th European Charge Density Conference* , Potsdam (D), **2006**.

2 "Charge density distribution in a metallaphosphane – the bonding situation in $Me_2Al(\mu\text{-}Py)_2P$"; Kathrin Götz, Julian Henn, Dirk Leuser, Dietmar Stalke *Sagamore Conference*, Birmingham (GB), **2006**.

3 "Calculation of Nuclear Spin-Spin Coupling Tensors by Density Functional Methods"; Kathrin Götz, Martin Kaupp, Dietrich Gudat, *Ampere NMR Summer School*, Zagopane (PL), **2007**.

4 "Presence or absence of metal-metal bonding in B- and C-bridged transition metal complexes from ELF and AIM studies"; Kathrin Götz, Martin Kaupp, *43rd Symposium of Theoretical Chemistry*, Saarbrücken (D), **2007**.

5 "Bonding Patterns in Dimeric Transition Metal Complexes – ELF and AIM analyses in a nutshell"; Kathrin Götz, Martin Kaupp, *Chemie-Symposium der Studierenden Mainfrankens*, Wuerzburg (D), Posterprize, **2007**.

6 “Unexpected Dependence of AIM and ELF results on exchange correlation functional”; Kathrin Götz, Martin Kaupp, *Workhop on Electron Localizability*, Dresden (D), **2008**.

7 “Bonding in Transition Metal Complexes”; *Workshop on Modern Methods in Quantum Chemistry*, Kathrin Götz, Martin Kaupp, Mariapfarr (AU), **2008**.

8 “On the role of Pauli repulsion in metal-metal bonding of dinuclear transition metal complexes”; Kathrin Götz, Tilman Hain, Dorothee Krämer, Martin Kaupp, *5th European Charge Density Meeting*, Gravedona (IT), **2008**.

9 “QTAIM Analysis of Lithiumorganics – Fundamentals and Application”; Kathrin Götz, Martin Kaupp, *DFG meeting* SPP 1178, Banz (D), **2009**.

Unser größter Ruhm ist nicht, niemals zu fallen,
sondern jedes Mal wieder aufzustehen.
Ralph Waldo Emerson

Danksagung

Für jene Menschen, die mich durch Inspiration und Diskussionsbereitschaft, mit Zuspruch und Anteilnahme und durch ihre Lebensfreude und eine Prise Humor, die alles erträglicher macht, die letzten Jahre begleitet haben.

Besonderer Dank gilt meinem Doktorvater ***Prof. Martin Kaupp****, der mir in seiner Arbeitsgruppe nicht nur einen Neuanfang auf dem weiten und spannenden Feld der theoretischen Chemie ermöglichte sondern ein nie versiegender Quell an Wissen, Ratschlägen und Anekdoten aller Art war. Bedanken möchte ich mich vor allem für den großen wissenschaftlichen Freiraum, der mir die Entwicklung eigener Ideen gewährte, und das Vertrauen, das in mich und meine Arbeit gesetzt wurde.*

Darüber hinaus danke ich meinen zahlreichen Kooperationspartnern für eine wissenschaftlich sehr fruchtbare, interessante und bereichernde Zusammenarbeit. Besonders zu erwähnen sind hier:

Prof. Holger Braunschweig und seine Arbeitsgruppe *(insbesondere Rian Dewhurst, Michael Burzler, Melanie Forster, Krzysztof Radacki), mit deren Chemie sich ein Großteil dieser Arbeit befasst. Vielen Dank für zahlreiche Diskussionen und die große, ansteckende Begeisterung für Borylen Komplexe (von wegen bor-ing).*

Prof. Carsten Strohmann und Viktoria Gessner *für die fruchtbare und spannende Arbeite an „Methyllithium und seine Freunde“ sowie die gesamte Strohmann’sche Gruppe für die gemeinsame Zeit im 4. Stock.*

Dr. Carlo Gatti *(CNR-ISTM,* Milano*), dessen geduldigen Bemühungen es mit zu verdanken ist, dass das Methyllithium Projekt einen so guten Abschluss gefunden hat.*

Zudem gilt mein großer Dank dem gesamten ***AK Kaupp*** *sowie seinen ehemaligen Mitgliedern James Asher, Sebastian H.-Riedel, Christian Remenyi; explizit auch dem Computer-Team bestehend aus Manuel Renz und Robert Müller sowie der* ***Bratislava-***

Gang *mit ihren Mitgliedern Vladimir und Olga Malkin, Elena, Stano, Michal und Peter, die mich durch die letzten Jahre mit vielen wissenschaftlichen und sonstigen Diskussionen begleitet haben; und den vielen Studenten, die als F-, Schnupper- und Theorie-Praktikanten stets eine Bereicherung waren.*

Aufs herzlichste möchte ich mich bei den „Mädels“ ***Hilke Bahmann*** *und* ***Sandra Schinzel*** *bedanken, denn mit euch hatte ich eine großartige Zeit, nicht nur in den zahlreichen Mensa-Boykott-Mittagspausen sondern in fast jeder Lebenslage.*

Hilke Bahmann *danke ich für ihre Ehrlichkeit, die ein so rares Gut ist, und die freundschaftliche Kritik, die es mir erlaubt hat mich sowohl fachlich, vor allem aber auch menschlich weiterzuentwickeln. Ich danke dir für deine „Unbequemlichkeit“, denn du bist der Extra-Schub in meinem Leben.*

Sandra Schinzel *danke ich für ihr sonniges Gemüt und die Lebensfreude, die mal durch herzhaftes Lachen mal durch „unerwartete“ musikalische Auswüchse aus dem Nachbarbüro zu mir drang. Deine fröhliche Anwesenheit hat viele Dinge in den letzten Jahren einfacher und schlichtweg „arch schön“ gemacht.*

Bedanken möchte ich mich auch bei meinem geduldigen, liebenswert stoischen Bürokollegen ***Robert Müller*** *für 2 schöne gemeinsame Jahre in 416 mit geteiltem Musikgeschmack, gemeinsamen Pausen vor der Tür und vielen Theorie Diskussionen sowie bei* ***Johannes Schraut****, der ein bisschen frischen Wind in diesen AK gebracht hat. Die zahlreichen Diskussionen der letzten Wochen waren stets unterhaltsam auch, wenn wir nie eine Antwort auf die großen Fragen des Lebens und der Liebe fanden.*

Nicht zuletzt gilt mein persönlicher Dank all jenen Menschen meines privaten Umfeldes, die mir über die „Tiefs“ hinweghalfen und die „Hochs“ mit mir gefeiert haben, als da besonders zu nennen wären ***Rian Dewhurst*** *(besides the English „boost“, I enjoyed a lot of wine drinking and awesome evenings with you),* ***JC Tremblay*** *(nicht nur für die großzügige Aufnahme während meiner Berliner Zeit, sondern für unglaublich bereichernde Diskussionen über das Leben, die Liebe und fast alles andere),* ***Nele Welter*** *(für ihre so angenehm bodenständige Art),* ***Steffi Sparka*** *(die in einer für sie so schwierigen Zeit zur Freundin wurde),* ***Peter Fischer*** *(für ein kleines-großes Wunder in meinem Leben) und viele Freunde mehr, die mich durch die letzten Jahre begleitet, ermutigt und unterstützt haben.*

*Mein besonderer Dank gilt meiner **Familie** – meinen Eltern Erwin und Yvonne Götz sowie meiner Schwester Nina Götz – für euren Zuspruch und eure Unterstützung sowie auch für manches kritisches Wort, das mir eine klarere Sicht auf die Dinge ermöglicht hat. Ihr habt stets an mich und meine Fähigkeiten geglaubt und mir den Mut gegeben für meine Ziele zu kämpfen.*

Den größten Dank werde ich jedoch persönlich übergeben.